STUDIES ON HYBRID ORGANIC-INORGANIC PHOTODIODES

A thesis

submitted in partial fulfillment for the

degree of

MASTER OF SCIENCE

(Material Science)

By

PRASHANT KUMAR

CHEMISTRY AND PHYSICS OF MATERIALS UNIT

JAWAHARLAL NEHRU CENTRE FOR ADVANCED SCIENTIFIC RESEARCH

(A DEEMED UNIVERSITY)

Bangalore – 560 064

To My Parents

DECLARATION

I hereby declare that the matter embodied in the thesis entitled "**STUDIES ON HYBRID INORGANIC-ORGANIC PHOTODIODES**" is the result carried out by me at the Molecular Electronics Laboratory, Jawaharlal Nehru Centre for Advanced Scientific Research, Bangalore, India under the supervision of Prof. K. S. Narayan and has not been submitted elsewhere for the award of any degree or diploma.

In keeping with the general practice in reporting scientific observations, due acknowledgement has been made whenever the work described is based on the findings of other investigators.

Prashant Kumar

JAWAHARLAL NEHRU CENTRE FOR ADVANCED SCIENTIFIC RESEARCH

Jakkur, Bangalore 560064, India

K. S. NARAYAN
Professor
PHONE: 91 80 22082822
FAX: 91 80 22082766
e-mail: narayan@jncasr.ac.in

April 3rd, 2012

CERTIFICATE

I hereby certify that the matter embodied in this thesis entitled "**STUDIES ON HYBRID INORGANIC-ORGANIC PHOTODIODES**" has been carried out by Mr. Prashant Kumar at the Molecular Electronics Laboratory, Chemistry and Physics of Materials Unit, Jawaharlal Nehru Centre for Advanced Scientific Research, Bangalore, India under my supervision and it has not been submitted elsewhere for the award of any degree or diploma.

Prof. K. S. Narayan

Acknowledgement

I express my sincere thanks to my research supervisor Prof. K. S. Narayan, for introducing me to an interesting and challenging research problem. His invaluable guidance, constant support and encouragement throughout my masters research work. I am also thankful to his family members for their hospitality and support.

I would like to thank Dr. Suchismita Guha, University of Missouri, Columbia MO, for her valuable discussions on the project and providing with the n-Gallium Nitride substrates.

I take privilege to thank my Integrated PhD course instructors for their teachings and discussions.

I am thankful to all academic, administrative and technical staff for financial and technical support.

I acknowledge my lab members Dr. Monojit Bag, Sabayasachi Mukhopadhyay, Dr. Srinidhi Ramchandran, Anshuman Jyoti Das, Vini Gautam, Satyaprasad Premswaroop Senanayak, Ravichandran S., Nishit Srivastava, Vijay Venugopalan, Madhushankar B. N., Kishor V. C. and Ashar A. Z. for valuable scientific discussions and help on understanding the experimental techniques.

I would like to thank all my friends in JNCASR and the Integrated PhD family for their help and support.

I express my heartiest gratitude towards my brothers and sisters for their love, affection, support and encouragement.

Table of contents

DECLARATION 6

CERTIFICATE 8

Acknowledgement 10

Table of contents 12

PREFACE 16

List of Figures 20

List of Tables 26

Notations/Abbreviations 28

CHAPTER 1 30

GENERAL INTRODUCTION 30

1.1 Introduction 30

1.2 Polymer Semiconductor 34

1.2.1 Electronic Structure 37

1.2.2 Charge Transport in Disordered Polymer Semiconductor 40

1.2.3 Photophysics of polymer semiconductors 43

1.2.4 Charge Carrier loss mechanism 47

1.3 Nitride Semiconductors 49

1.3.1 Crystal structure and Band diagram 50

1.3.2 Photo – excitation and charge transport 52

1.4 Organic – Inorganic Hybrid Systems 56

1.4.1 p-n junction versus OI junction 57

1.4.2 I-V models 60

1.4.3 Interface states 65
1.4.4 Examples of Organic – Inorganic Hybrid systems 68
1.4.5 Problems with OI hybrids 69
1.5 Overview and Scope of the thesis 70
CHAPTER 2 74
MATERIALS AND METHODS 74
2.1 Introduction 74
2.2 Semiconducting Polymers 75
2.2.1 pBTTT – C14 76
2.2.2 P3HT 78
2.2.3 N2200 (n type polymer) 79
2.3 Inorganic Semiconducting Material 80
2.3.1 n-Doped Gallium Nitride 81
2.4 Buffer layers and metal electrodes 84
2.4.1 Work Function requirements 84
2.4.2 Problems with thermal deposition of top metal electrodes 87
2.4.3 Advantage of Buffer layer 89
2.5 Device Architecture and Fabrication 91
2.6 Charge Transport Characterization Technique 93
2.6.1 Current – Voltage (I-V) curves 94
2.6.2 Spectral Photocurrent response 95
2.6.3 Capacitance Spectroscopy 97
2.6.3.1 Capacitance – Voltage Technique 98
2.6.3.2 Capacitance – Frequency measurement 101
2.6.4 Intensity Modulated Photocurrent Spectroscopy (IMPS) 102

CHAPTER 3 106
STEADY STATE AND TRANSIENT STUDIES 106
3.1 Introduction 106
3.2 Measurement and Analysis 111
3.2.1 Current – Voltage Characteristics (I –V curves) 111
3.2.2 Capacitance – Voltage measurement 123
3.2.3 Capacitance – Frequency Measurement 126
3.2.4 Intensity Modulated Photocurrent Spectroscopy 130
3.3 Summary 132
CHAPTER 4 134
SPECTRAL PHOTOCURRENT RESPONSE OF HYBRID PHOTODIODE STRUCTURE 134
4.1 Introduction 134
4.2 Measurement and Analysis 136
4.2.1 n-Gallium Nitride/Polymer diode 137
4.2.1.1 Illumination from n-GaN side 138
4.2.1.2 Illumination from top electrode 142
4.3 Effect of different control parameters on spectral photocurrent response 145
4.3.1 Effect of Electrical Bias 145
4.2.2 Thickness dependence of spectral photocurrent 148
4.2.3 Background illumination dependence 148
4.4 Summary 150
CHAPTER 5 152
MODELING SPECTRAL PHOTOCURRENT RESPONSE 152
5.1 Introduction 152
5.2 Device Modeling 153

5.3 Modifications Required 160

5.4 Implications 162

CHAPTER 6 164

SUMMARY AND FUTURE DIRECTIONS 164

REFERENCES 168

PREFACE

Organic – inorganic hybrid semiconductor heterostructures exhibit interesting combination of properties originating from the two distinct families of semiconductors. The hybrid structures are formed from conventional doped-inorganic semiconductor layer and layer of organic/polymer thin film which can have either a donor or acceptor type characteristics. The polymer semiconductor offer an advantage of solution processability on the wafers of inorganic material and is a less-elaborate method compared to controlled sublimation procedures for depositing low molecular weight organic molecules. The first few studies carried out by Forrest et.al using n-type and p-type silicon and small (organic) molecules showed that these structures are not very similar to normal p-n junctions. The initial picture of charge transport was sketched in terms of thermionic emission in low current regime and space charge limited current under high current regime. Later new and exciting materials including inorganic materials like GaAs, InP, Ge etc and organic materials like MEHPPV, P3HT, CuPC etc, where studied for hybrid device applications. Since then the properties observed for organic-inorganic hybrid systems have shown a continuous development with remarkable 10% power conversion efficiencies from n-type Si/P3HT cells and field effect mobilities ~ $1cm^2/V.s$ for perovskite based hybrid materials. Concept of hybrid exciton at the organic inorganic interface containing the property of Frenkel and Wannier Mott excitons was proposed by V. M. Arganovich et.al. The nature of the heterostructure between the organic and inorganic semiconductors has remained debatable as the predictions in the general trend in the properties have not been accurate. The interface has a key role to play in the electrical charge transport and optical properties of the hybrid structures. Formation of new states, traps and recombination centers have much to decide the fate of an organic – inorganic hybrid device. In this respect we try to explore both the role of bulk and the interfacial contributions in organic – inorganic hybrid structures. The effects on the charge transport in the bulk and at the interface and the associated transport parameters have been studied for a variety of n-GaN/Polymer hybrid structures.

The choice of this system is motivated from the idea that, p –type donor semiconducting polymers are available in large number and with large variety of band gaps, compared to n – type acceptor polymers. Similarly the n- doped inorganic semiconductors are readily available. The

second advantage, as in the case of n- doped gallium nitride, is that the layer provides a transparent window for visible and near infrared region while blocking/absorbing the UV component. This visible-IR pass filter helps in direct excitation of polymer without much reflection losses, and protects from UV exposure of the polymer layer. These interesting model systems also demonstrate the possibility for applications as UV – Visible – IR detectors band selective detector. Hence, the spectral responses of the photoelectric properties of these structures form an integral part in these studies both from the understanding and application perspectives.

The chapter 1 of this thesis gives a brief introduction about the bulk organic and inorganic semiconductors properties and related electronic and optical mechanisms. The structure of hybrid devices, difference from a normal p-n homojunction, current-voltage characteristics models, and interface states for hybrid systems are discussed in details. Chapter 2 presents a detail characterization of organic and inorganic materials used in current work. The fabrication steps for an n-GaN/polymer device have been summarized. The device fabrication requires solutions to many basic problems related to electrode shorting and work function selections, a detailed description on this regard has been presented. An introduction to the charge transport characterization techniques used in this study has been presented along with experimental setup, calibration and measurement details, and relevant models to explain the experimental results have been presented.

In chapter 3, results of steady state measurements have been presented, the current – voltage characteristics for three different energy structures has been shown, which shows a characteristic difference. An attempt has been made to calculate the barrier height and diode ideality factor, which shows a dependence on the type of energy structure and top electrode used. The light response of these hybrid structures is strongly dependent on the type of energy structure and top electrode used. Small signal impedance measurement has been performed to evaluate the built in field present inside the device. The values obtained are not reasonable as they are much higher than expected, which suggests the requirement of modification of the model applied to this structure. Admittance spectroscopy gives a picture of the trap state response which is different for different donor polymers. A clear peak in conductance versus frequency curve of n-GaN/pBTTT hybrid structure is observed which also corresponds to a step

in the capacitance measured as a function of frequency. This peak is a signature of shift from bulk to interface depletion capacitance. An approximate interface state density has been calculated, which is found to be of the same order of magnitude as the expected surface state density of n-GaN. The Intensity modulated photocurrent spectroscopy was performed to track the interface and bulk trapping and recombination events. A characteristic peak at 10 kHz has been observed which is characteristic to the donor polymer pBTTT. The wavelength dependent response is interesting; such a response has not been understood completely, it is speculated that the three different responses originate from three distinct regions of inorganic bulk, organic bulk and inorganic – organic interface.

Chapter 4 contains the results for spectral photocurrent measurement; this experiment has been used to study the effect of basic physical process like generation, transport, trapping, and recombination on the photoconductivity of the hybrid devices. In present work this study has been used to understand the transport and photoconductivity in the bulk as well as interface. A characteristic symbatic and antibatic response has been observed for forward and reverse biased devices. Effect of various external control parameters has been studied on the photoconductivity of the hybrid structures. In our studies, a completely different response for type I and type II structure was seen under zero external bias condition.

In chapter 5, the existing methods to model the spectral photocurrent response of organic and inorganic semiconductors has been presented. Many models have been predicted for modeling the spectral response of inorganic as well as organic small molecules. The extensions to polymer semiconductors are limited by many assumptions which are made while applications. A total current density expression has been derived by combining the spectral response from different layers of the n-GaN/polymer hybrids. To improve the agreement between the experimental and modeled response, possible areas of modifications required in the existing models have been mentioned. Chapter 6 summarizes the results of the thesis and gives an over view of future works required to be done to understand the transport properties and interface effects in n-GaN/Polymer hybrid heterostructures.

List of Figures

Figure 1.1: Schematic of photodetector application in data communication..... 31
Figure 1.2 : Visualization of light absorption, electron hole creation and light induced current in p-n junction diode. 31
Figure 1.3 : a) σ- and π- bonds in ethene, example of simplest conjugated system. b) energy levels of π conjugated system and electronic excitation between bonding π and anti bonding π^* orbital 35
Figure 1.4 : a) Energy diagram of two interacting carbon atoms, b) band structure emerging with increase in the conjugation length 37
Figure 1.5 : Trans-polyacetylene a) before distortion b) after distortion. c) E versus k before distortion d) E versus k after distortion..... 38
Figure 1.6 : Schematic representation of Gaussian distribution of state in energy and position space..... 42
Figure 1.7 : a) First Brillouin zone for WR crystal structure and b) E versus k diagram for WR GaN 51
Figure 1.8 : Energy band diagram for p-n homojunction diode. 58
Figure 1.9 : a) Flat band Energy diagram and b) equilibrium energy diagram for inorganic s-s heterostructure..... 59
Figure 1.10 : Energy band diagram for trap dominated s-s heterostructure interface. 60
Figure 1.11 : Energy band diagram for OI hybrid structure with n-doped inorganic layer and donor polymer semiconductor. 60
Figure 1.12 : Schematic representation of forward biased and reverse biased OI heterojunction band diagram 61
Figure 1.13 : Schematic representation of a) perpendicular b) parallel alignment between substrate and molecule. 66
Figure 1.14 : A schematic diagram for band bending and dipoles present at the interface. 67
Figure 1.15 : Common donor type polymer semiconductors. 71

Figure 2.1 : Chemical structure of pBTTT-C14, P3HT and N2200 Polymers 75

Figure 2.2 : Normalized absorption and PL emission for pBTTT. Absorption peak is at 520 nm and PL peak is at 720 nm. 76
Figure 2.3 : Plot of absorption coefficient (α) of pBTTT as a function of wavelength (λ). 77
Figure 2.4 : Cyclic voltammeter plot for pBTTT. 77
Figure 2.5 : a) Absorption spectra and b) absorption coefficient for P3HT films. 78
Figure 2.6 : a) Schematic representation of 'a' type stacking in P3HT films and b) corresponding XRD peak, ($2\theta = 5.23^0$) 79
Figure 2.7 : Absorption spectra for N2200 polymer film (50nm). 80
Figure 2.8 : Absorption and PL emission for n-GaN films grown through MOCVD. 83
Figure 2.9 : Absorption coefficient for n-GaN films, as calculated for 3μm thick n-GaN films.. 83
Figure 2.10 : Work function mismatch in non contact mode for a) n –type and b) p – type semiconductor. Barrier formed for c) n- type and d) p –type semiconductor..... 85
Figure 2.11 : I-V plot for In/n-GaN/In structure, showing ohmic nature for In/n-GaN contact placed. 86
Figure 2.12 : I-V plots for a) pBTTT and b) P3HT, the I-V shows that the buffer layer (PProDOT) contact with pBTTT and P3HT is ohmic. 87
Figure 2.13 : I-V plots for n-GaN/pBTTT OI diode a) without PProDOT buffer layer and b) with PProDOT buffer layer. 89
Figure 2.14 : Chemical structure for PEDOT:PSS and PProDOT..... 90
Figure 2.15 : Transmission spectrum form n-GaN before (black) and after (red) polishing. Glass transmission (blue) has been shown for reference. 91
Figure 2.16 : A schematic structure for n-GaN/pBTTT OI hybrid heterostructure device. The pBTTT layer is replaced by other polymers. 92
Figure 2.17 : Schematic diagram for I-V measurement of OI hybrid heterostructure device. 94
Figure 2.18 : Schematic diagram for spectral photocurrent measurement. The bias source and/or LED are active only when they are required for the measurement..... 97
Figure 2.19 : Schematic diagram for Capacitance – Voltage and Capacitance – Frequency measurement 100
Figure 2.20 : Schematic diagram of IMPS setup using LED and beam expander to have a uniform illumination of the sample..... 104

Figure 3.1 : a) PL emission from n-GaN for 320 nm excitation. b) Excitation wavelength versus PL emission intensity at 550 nm for n-GaN. 108
Figure 3.2 : Overlap between the absorption of pBTTT (red) and emission of n-GaN defect state (black). Overlap area has been shaded. 108
Figure 3.3 : PL emission from n-GaN/pBTTT hybrid interface at different wavelength. PL emission intensity versus n-GaN excitation wavelength (inset). 109
Figure 3.4 : Energy levels of inorganic and organic semiconductors under noncontact mode, type I (black) and type II (green) energy structures has been shown. b) Possible band bending at the OI interface under contact. 110
Figure 3.5 : Linear and semi log Plot of dark I –V curve for n-GaN/pBTTT hybrid diode. 112
Figure 3.6 : Thermionic emission model fit to forward current – voltage characteristics for n-GaN/pBTTT hybrid devices. 113
Figure 3.7 : a) The Dark and light I-V for n-GaN/pBTTT system. Inset shows the log – normal plot of dark and light I-V. b) Wavelength dependence of I-V. 114
Figure 3.8 : I) $JSc \propto I\alpha$ fit to J_{Sc} versus I plot. II) $VOC \propto Sln {}^{I}/_{I_0}$ fit to V_{OC} versus I plot. III) J_{Sc} versus photon flux showing almost linear behavior. IV) V_{OC} versus photon flux on a log – linear plot shows the saturation nature of open circuit voltage. 115
Figure 3.9 : Energy band diagram for n-GaN/P3HT hybrid system. 116
Figure 3.10 : I –V plot for n-GaN/P3HT hybrid devices a) linear and b) semi logarithmic. 117
Figure 3.11 : Thermionic emission model fit for forward I-V of n-GaN/P3HT devices for lower current density (~ 1mA/cm^2). 118
Figure 3.12 : Light and dark I –V for n-GaN/P3HT devices. The light response is similar to the n-GaN/pBTTT hybrid devices. 119
Figure 3.13 : Energy band structure for n-GaN/N2200 n-n heterostructure. 120
Figure 3.14 : Dark I-V linear and semi logarithmic for n-GaN/N2200/Al and n-GaN/N2200/Au. It should be noticed that there is no offset in the dark I –V. The space charge effects are clearly visible for gold electrode. 121
Figure 3.15 : Thermionic emission (Green) and space charge (red) fit to n-GaN/N2200/AU and nGaN/N2200/Al devices. Where the Au top electrode devices fit better to the space charge model. 122
Figure 3.16 : Light and dark I-V for n-GaN/N2200/Al devices. 122

Figure 3.17 : C – V and $1/C^2$ – V plot for n-GaN/pBTTT hybrid diodes. The Nature of the curve is not like an abrupt or linearly graded junction. 124
Figure 3.18 : Approx doping profile in n-GaN/pBTTT region where the position is measured from the highly doped region into the lightly doped region. 125
Figure 3.19 : C_j versus V_A and $1Cj2$ versus V_A plot with second order polynomial fit for n-GaN/P3HT hybrid diodes. A monotonic decrease in capacitance with applied voltage is visible in C_j versus V_A plot. 126
Figure 3.20 : Conductance and capacitance plot versus frequency for n-GaN/pBTTT device. . 127
Figure 3.21 : Equivalent circuit for single time constant model. 128
Figure 3.22 : Single time constant fit for G_P/ω (the loss factor) versus frequency for pBTTT/n-GaN hybrid diode. 128
Figure 3.23 : Capacitance and conductance versus frequency curve for n-GaN/P3HT. As compared to n-GaN/pBTTT devices these devices do not show any peak in conductivity. 129
Figure 3.24 : Average power of different wavelength LED as a function of modulation frequency. 130
Figure 3.25 : IMPS response from two different devices measured at different wavelength at room temperature. 131

Figure 4.1 : An approximated band diagram showing additional field for hole transport and expected direction of hole current under zero bias. 137
Figure 4.2 : a) Spectral photocurrent response from n-GaN/pBTTT device, A schematic of direction of illumination has been shown. b) The dc photocurrent measurement shows the intensity dependence of photocurrent. 139
Figure 4.3 : Spectral responsivity and EQE % for n-GaN/P3HT device. Direction of illumination has been shown in the figure. 140
Figure 4.4 : Spectral response (black) and EQE (red) plot for n-GaN/N2200/Al devices, illumination from n-GaN side. Direction of illumination has been indicated. 141
Figure 4.5 : a) Normalized Responsivity for illumination from top (Au) electrode (black) and bottom n-GaN (red), b) schematics of direction of illumination. 142

Figure 4.6 : Normalized Responsivity for illumination from top Au electrode (black) and bottom n-GaN/polymer interface (red). 144
Figure 4.7: Spectral photocurrent response a) n-GaN, b) pBTTT under applied reverse bias, direction of illumination is from n-GaN side. 146
Figure 4.8 : The forward biased spectral photocurrent response from n-GaN/pBTTT devices, illumination from n-GaN side. 147
Figure 4.9 : Spectral photocurrent response from n-GaN/pBTTT OI hybrid devices, a) illumination from n-GaN and b) illumination from gold electrode, under forward and reverse biased conditions. 147
Figure 4.10 : Spectral response from n-GaN/P3HT devices for 130 nm and 90 nm P3HT films. 148
Figure 4.11 : Spectral photocurrent response from n-GaN/pBTTT devices in the presence of background illumination a) response from n-GaN, b) response from pBTTT. 149

Figure 5.1 : Schematic representation of OI HJ semiconductor diode with bulk and barrier layer band diagram. a) light illumination from ohmic and b) barrier electrode. 153

List of Tables

Table 2.1 : material properties for n-GaN films grown on sapphire..... 82

Table 3.1 : Summarized transport parameters for n-GaN/Polymer hybrid structure..... 132

Notations/Abbreviations

Abbreviations	Details
DOS	Density of States
HOMO	Higher occupied molecular orbital
LUMO	Low occupied molecular orbital
PProDOT	poly(3,4-propylenedioxythiophene)
PEDOT:PSS	poly(3,4-ethylenedioxythiophene):Polystyrenesulphonic acid
MEH-PPV	Poly(2-methoxy 5-[2'-ethylhexyloxy]-p-phenylene vinylene
P3HT	Poly–[3– hexylthiophene]
pBTTT	Poly(2,5–bis(3–tetradecyllthiophene–2– yl)thieno[3,2 -b]thiophene)
N2200	Poly{[N,N' - bis(2-octyldodecyl)-napthalene-1,4,5,8-bis(dicarboximide)-2,6-diyl]-alt-5,5'-(2,2'-bithiophene)} (P(NDI20D-T2)
n-GaN	n- doped Gallium Nitride
SPR	Spectral photocurrent response
OI HJ	Organic – Inorganic Heterojunction
I-V	Current - Voltage
IMPS	Intensity Modulated Photocurrent Spectroscopy
UV	Ultraviolet
IR	Infrared

C-V	Capacitance - Voltage
C-F	Capacitance - Frequency
GDM	Gaussian Disorder Model
SM	Scher-Montroll

CHAPTER 1

GENERAL INTRODUCTION

1.1 Introduction

Semiconductors were discovered in early 19th century, when a decrease in resistance with increasing temperature was observed in certain materials [1]. Metal-semiconductor diodes and junction diodes were studied in 1870's [2] and used widely in radio frequency receivers during Second World War [3]. The first solid state transistors made of germanium was demonstrated by Bell labs in 1947 [4]. These solid state devices were capable of replacing bulky vacuum tubes with even better electrical characteristics. The potential of transistors in data storage and processor applications attracted a large focus from scientific and industrial community. The advances in semiconductor device technology, thus made over a period of time have brought a major breakthrough in modern day technology and development. With the development of light emitting diodes and photodetectors the possibility of optical data communication was realized [5], which brought about revolution in the world of modern communication and paved the path for further path breaking discoveries in the field.

Photodetectors essentially convert optical signals into electrical signals, primarily by absorbing optical photon and generating charge pairs which give rise to electrical signals. The process of converting received optical signal into electrical signal must involve minimal loss of the information. Figure 1.1 shows a basic role of photodetectors in optical communication systems, the LED or laser are transmitters, optical fibers are the wave guiding medium and the photodetectors are receivers, where the transmitted optical signal is converted back to electrical

signals. Owing to these properties, the photodetectors are used as integral part of remote control systems, circuit isolators, intruder alarms, and many other consumer electronics.

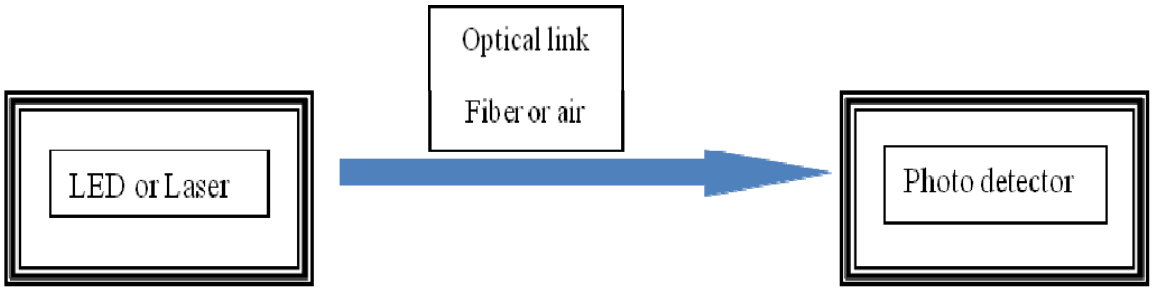

Figure 1.1: Schematic of photodetector application in data communication.

A normal p-n junction can be used as a photodetector, when a photon with energy sufficient to excite an electron, strikes the diode, it create a free electron – hole pair. If the photon is absorbed in the p-region or n-region within unit carrier diffusion length, or the depletion zone, the carriers are swept away from the junction under the built in field of the depletion region. The hole moves towards anode and electron moves towards cathode giving rise to photocurrent. The schematic of photodetector working has been shown in Figure 1.2. The photocurrent is a sum of dark and light current. Photodetector with higher sensitivity should have low dark saturation current density.

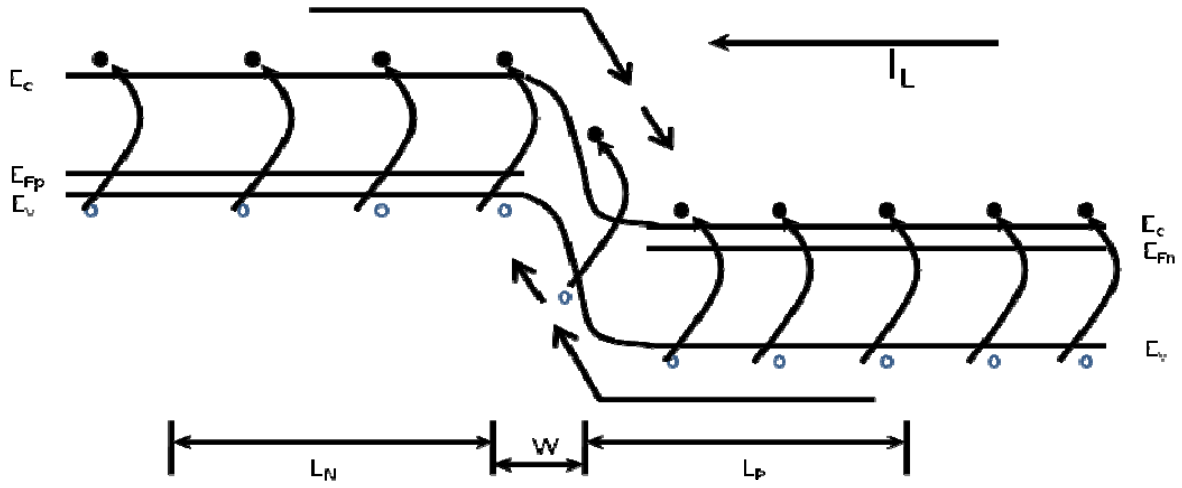

Figure 1.2 : Visualization of light absorption, electron hole creation and light induced current in p-n junction diode.

Mode of operation

A photodetector can work in two different modes,

Photovoltaic mode

When a photodetector is used in zero bias or photovoltaic mode, the current flowing out of the device is restricted, which gives rise to voltage build up. Using in this mode exploits the photovoltaic effect of semiconductor, which is also the basis for solar cell.

Photoconductive mode

In the photoconductive mode, the detector is held at the reverse bias. The reverse biased detectors have increased responsivity and reduced response time, but at the cost of increased level of electrical noise.

The junction depletion region can be viewed as a capacitor with capacitance value given by [6],

$$C_{junction} = \frac{\varepsilon_S A}{W} \tag{1.1}$$

In equation 1.1, $C_{junction}$ is junction capacitance, ε_s is the permittivity of semiconductor material, A is the area of the photodetector (photo diode), and W is the width of the depletion region. Applying reverse bias increases the width (W) of the junction causing decrease in junction capacitance, which results in faster response time, but also increases the electrical noise.

Performance of any photodetector depends on three critical parameters,

Responsivity

Responsivity is defined as the ratio of generated photocurrent to incident light power, and is typically expressed in units of A/W (Ampere per Watt) when operating in photoconductive mode. It can also be expressed as *Quantum Efficiency,* or probability of an electron-hole pair generation for each incident photon. For a good photodetector, the responsivity should be high (~ 0.1A/W) [7].

Dark Current

It is defined as the current flowing through the photodetector in the absence of light, when operated in photoconductive mode. It includes photogeneration by background radiation and the saturation current of semiconductor junction. For a good photodetector, the dark current must be very low (~ nA) [8].

Noise Equivalent Power (NEP)

It is the minimum input optical power required to generate photocurrent, equal to root mean square (rms) noise current in the 1Hz band width. The related characteristic detectivity (D) is defined as 1/NEP. Specific detectivity (D^*) is the detectivity normalized to the area (A) of the photodetector.

$$D^* = D\sqrt{A} \tag{1.2}$$

Sensing wavelengths from UV to infrared is vital for applications in various fields like industrial, scientific, environmental, communication, remote control etc. To detect wavelengths starting from UV to near infrared, different materials are being used as sensors, GaN (spectral range 0.2 μm to 0.35 μm) [9], Si (spectral range 0.40 μm to 1.1 μm) [10] and InGaAS (spectral range 0.9 μm to 1.7 μm) [11] are used for detection in UV, visible and infrared bands respectively. Availability of polymer semiconductor with advantages of high optical absorption coefficient (α ~ 10^5 cm^{-1}) [12], large and ultrafast nonlinear responses [13], colour tunability [14], large active area and low processing cost over inorganic semiconductors [15], gives another possibility for fabrication of cheaper and wide spectral coverage photodetector. Polymer semiconductor based photo diodes have been reported with high detectivity and spectral range [16,17,18].

Yet another area of interest exists, in the field of organic – inorganic (OI) hybrid semiconductor systems, where the idea is to make use of the best properties of both the materials. The advantages offered by OI systems includes, I) wider, and wavelength selective absorption range and operation, II) wider and selective range of transparency, III) an integrated combination

of LED and photodetectors in sub-micron dimensions, and may more. OI hybrid semiconductor photodetectors have been reported with quantum efficiency ~ 85% and optical response time of 5ns [19]. OI semiconductor photodetectors have been fabricated with various small molecule and polymer organic semiconductors to give a wide range of spectral coverage [20,21].In the next sections the bulk properties of transport and photo-excitation in polymer semiconductors will be explained.

1.2 Polymer Semiconductor

Polymer semiconductors have brought a revolution in the field of plastic electronics. Though organic semiconductors are not new, first studies of dark and photoconductivity in anthracene crystals date back to the early 20th century [22,23]. Discovery of electroluminescence [24] in polymer diode structure triggered intense research, these investigations could establish the basics of the processes involved in charge carrier transport and photo-excitation. Systematic studies of conducting polymers started with the discovery of very high conductivity and controlled doping of conjugated polymers [25,26]. Demonstration of efficient photovoltaic cells made of organic heterojunction [27] and thin film transistor from conjugated polymers [28,29] opened up tremendous possibility in the field of organic electronics. With large academic and industrial efforts during the last two decades, organic light – emitting devices (OLEDs) [30,31], organic photovoltaic (OPVs) [32,33], and organic field effect transistors (OFETs) [34,35] have progressed rapidly and are entering in consumer market.

Organic semiconductors are conjugated systems where carbon atoms are linked together with alternating single and double bonds along the main chain providing path for carrier transport. A Carbon atom in its ground state has $1s^2 2s^2 2p^2$electronic configuration, in conjugated system 2s, $2p_x$ and $2p_y$ orbital hybridize to form three sp^2 hybridized orbitals which forms strong sigma bonds with hybridized or unhybridized orbitals of other atoms. The unhybridized $2p_z$ orbital stays perpendicular to the plane of sp^2 hybridized orbital and carries one unpaired electron. Neighboring $2p_z$ orbitals overlap to form delocalized π-electron cloud in the plane perpendicular to the plane of sigma bonds giving rise to electron delocalization along the conjugated backbone.

Due to the Peierls instability* [36] in symmetric 1-D electron distribution, these delocalized electron clouds form alternating single and double bond structure. Rearrangement of electron cloud along the polymer backbone gives rise to the formation of delocalized energy bands, known as bonding (π) and anti-bonding (π^*) orbital. The bonding orbital is lower in energy and is termed as Highest Occupied Molecular Orbital (HOMO), while the anti-bonding orbital is higher in energy and is known as Lowest Unoccupied Molecular Orbital (LUMO) in long conjugated chains [37,38], as shown in Figure 1.3. The energy gap, between π and π^* as a result of electron rearrangement, has a value between 1 – 3 eV for long conjugated segments. Such segments are, by definition, semiconducting in nature.

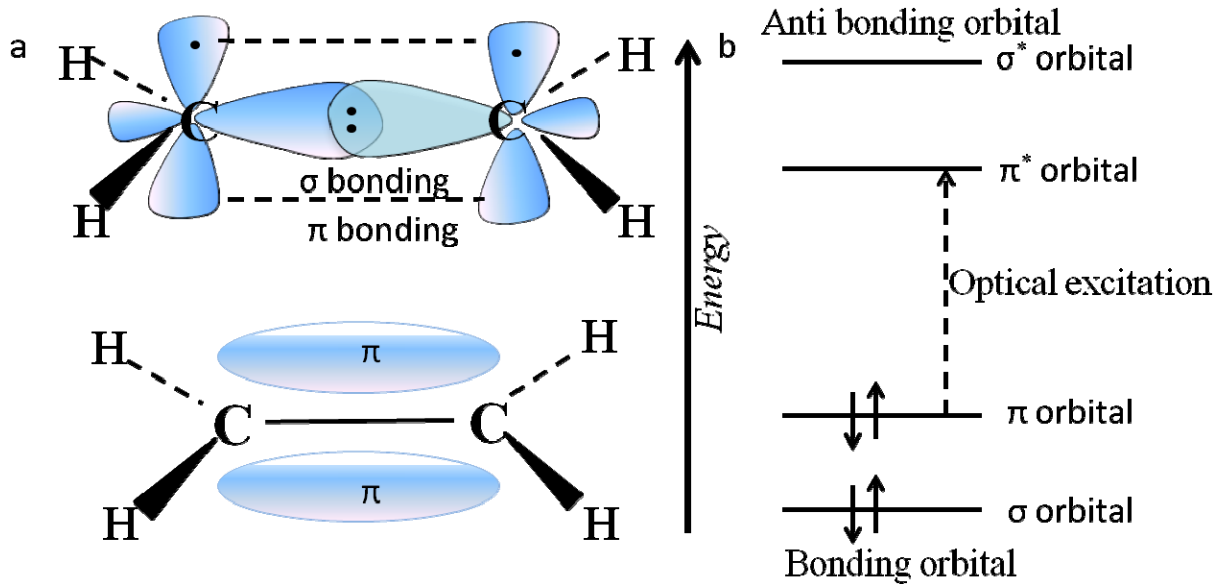

Figure 1.3 : a) σ- and π- bonds in ethene, example of simplest conjugated system. b) energy levels of π conjugated system and electronic excitation between bonding π and anti bonding π^* orbital, (Adopted from [39]).

Molecules in organic semiconductor bulk are bonded through weak van der Waals forces, which give rise to different mechanical, electrical and thermal properties like softness, lower

* Peierls Instability: Any symmetric 1-D electronic structure is unstable towards doubling of unit cell, which gives rise to alternate single and double bond. Such doubling of unit cell causes opening of energy gap at the Fermi level [36], as shown in figure 1.5.

melting point and lesser delocalization of electronic wave functions. Organic semiconductors are different in comparison to inorganic semiconductors in various aspects,

1. Organic semiconductors have charge carrier mobility ($\mu \sim 10^{-2}$ to 10^{-5} $cm^2/V.s$) [40] which is $10^4 - 10^6$ times lesser than inorganic semiconductors ($\mu \sim 10^2$ to 10^4 $cm^2/V.s$) [41].
2. Diffusion lengths of primary photoexcitations (exciton) in disordered organic materials (L_D (exciton) ~ 5-10 nm) [42] is very less compared to diffusion length for charge transport in inorganic semiconductors (L_D (Si) ~ 700 nm, L_D (GaAs) ~ 10 μm).
3. A key process in photon to current conversion in polymer semiconductors is exciton dissociation, which usually requires strong field owing to large binding energies (ΔE ~ 0.1 – 1.0 eV) [43].
4. Organic semiconducting materials have higher absorption coefficient ($\alpha \geq 10^5$ cm^{-1}) [44] compared to inorganic semiconductors ($\alpha \geq 10^4$ cm^{-1}) [45], which partly compensates for other less efficient processes.
5. One of the biggest advantages of organic semiconductors over any other family of semiconductors is the easily tunable band – gap and low cost, large scale processing. Band gap tuning is also possible for InAlGaN family [46], but it comes at a much higher cost.

One of the origins of defects in polymer semiconductors can be traced to, bending and twisting of polymer chain backbone and variations of radius of curvature. Another important feature of these materials is the interchain interaction which strongly depends on the local order. Structural studies of polymers show development of inhomogeneously placed disorder, crystalline regions along with relatively well packed chains present with regions of very short range interchain correlation. Local morphology of polymer films is very sensitive to their preparation methods, materials of same chemical structure can have different electronic properties, which would greatly depend on the processing conditions of films and devices.

A prime focus of the field have been on understanding the energy band structure, charge carrier transport, charge generation and photo-physics, and the loss mechanisms for charge carriers. In the next section a brief introduction of electronic structures in organic semiconductors will be given.

1.2.1 Electronic Structure

Conjugation is a basic requirement for an organic molecule to be semiconductor. As defined previously, conjugation is an arrangement of single and double bonded carbon atoms in a chain, which causes splitting of energy levels and delocalization of charges in these levels. Carbon atoms in conjugated molecules are in sp^2 hybridization, hybridized orbitals form strong σ bonds with other carbon atoms along the chain and side groups. Unhybridized p_z orbitals of neighboring carbon atoms overlap to form delocalized π and π^* molecular orbital's, splitting between π and π^*, as shown in Figure 1.4, is in the range of 1 – 3 eV which is typical for semiconductors. Molecules like polyethylene, which have only σ bonds, the gap is much larger and hence they are not semiconducting. In principle, a polymer is a chain of alternately single and double bonded carbon atoms of infinite length, effect of polymer chain lengths on their HOMO – LUMO splitting has been shown[47]. When polymer molecules are packed in solid films form, the average energy gap is further reduced as a result of van der Waals interaction between neighboring molecular orbitals. When the splitting between HOMO – LUMO is relatively small and a large electron delocalization occurs, the terms HOMO and LUMO are be replaced with valance band (VB) and conduction band (CB) respectively.

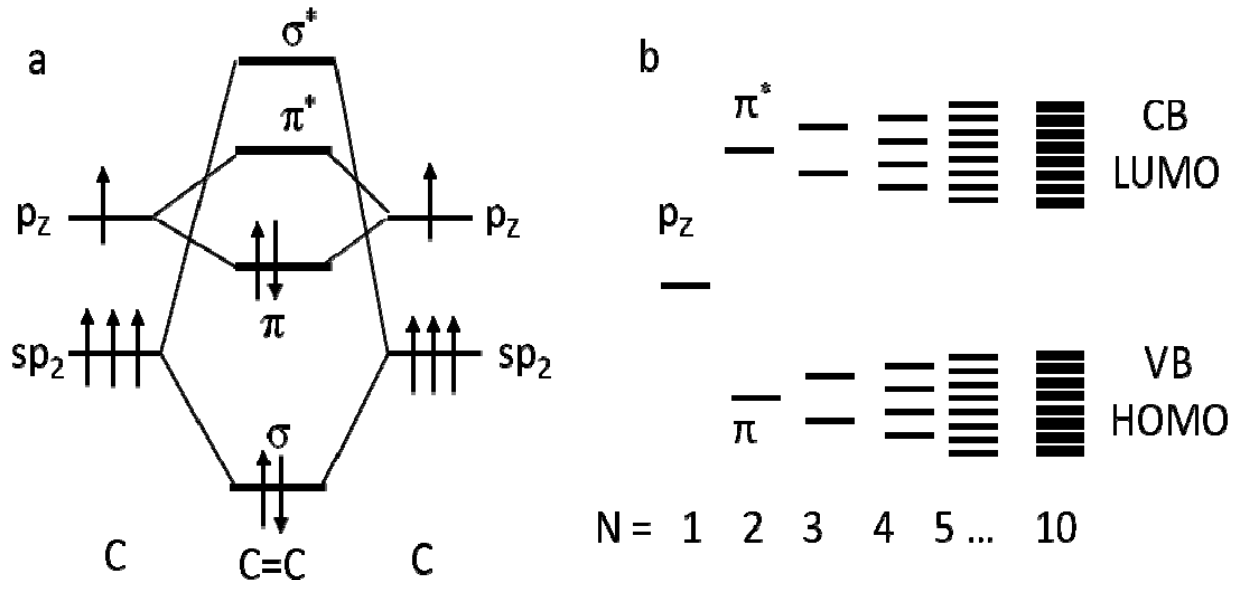

Figure 1.4 : a) Energy diagram of two interacting carbon atoms, b) band structure emerging with increase in the conjugation length (Adopted from [48]).

Using a very simple model of semi-classical particle in a 1-D box problem, it can be easily seen that the gap between the energy levels decreases with increasing length of polymer chain. We can assume delocalized π electrons along the conjugated chain as particles in a 1 – D box. For a box of length L, the energy levels and difference in the energy levels are given by,

$$E_n = \frac{\hbar^2\pi^2}{2m_eL^2}n^2 \text{ and } \Delta E = \frac{\hbar^2\pi^2}{2m_eL^2}(2n+1) \tag{1.3}$$

Considering the polymer of length L as a chain of 2N recurring units each of length a. If each monomer contributes *m*π electrons, than total number of states occupied is *Nm/2*.

$$\Delta E = \frac{\hbar^2\pi^2}{2m_eL^2(Na)^2}\left(2\left(\frac{Nm}{2}\right)+1\right) = \frac{\hbar^2\pi^2}{2m_ea^2}\left(\frac{m}{N}+\frac{1}{N^2}\right) \propto \frac{1}{N} \tag{1.4}$$

Thus, the gap between the two consecutive levels is inversely proportional to the length of polymer chain, energy E as the function π/a is a continuous curve. This type of material has no gap at the Fermi energy. Looking at the π electrons, one can consider this material as a quasi – one – dimensional system with *m*π electron per repeated unit. As such this is a metal with exactly half filled band. As pointed out by Peierls [36] such materials are unstable and go through doubling of unit cell, which leads to formation of alternate single and double bonds and opening of a gap at the Fermi level. Figure 1.5 shows the effect of doubling of unit cell on the band structure of trans-polyacetylene.

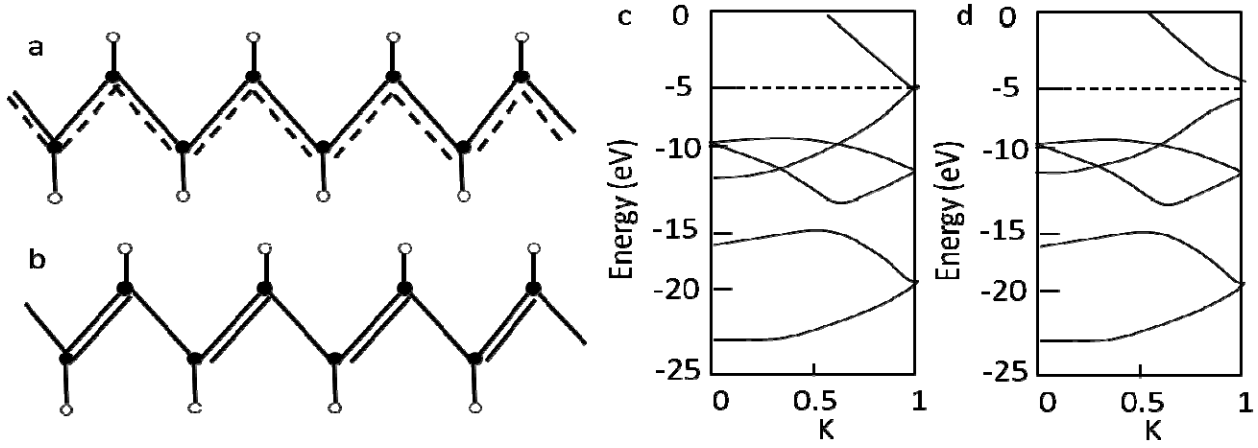

Figure 1.5 : Trans-polyacetylene a) before distortion b) after distortion. c) E versus k before distortion d) E versus k after distortion, (with kind permissions from Springer science + business

media: Organic Electronic materials conjugated polymers and low molecular weight organic solids, Theoretical studies of electronic properties of conjugated polymers, Vol. 41, 2001, 42, M. Springbore, K. Schmidt, H. Meider and L. De Maria, Fig. 2.4a-b, R. Farchioni, G. Grosso, Springer , (2001) [49]).

For a detailed description of energy band calculation in polymer semiconductors other references [49] can be consulted.

Energy band structure in amorphous organic materials

Organic materials are useful for applications when cost is a major factor. Single and poly – crystals are expensive and mostly amorphous materials satisfy the needs for cheaper materials. Amorphous materials are full of traps and the edge of conduction and valance band can be approximated as a distribution for conduction band state [50]. This distribution can be approximated by two exponential decaying functions one for conduction state and one for trap state, where conductive state are also called tail states [51]. It has also been argued by Tessler and Roichman that exponential distribution of states is not compatible with Gaussian distribution of states [52]. As an example of above argument, for positive charge state we can use [48]

$$ln(N_V(E)) = ln(N_{V0}) - E/kT_1 \quad \text{(Conduction band tail states)} \qquad (1.5)$$
$$ln(N_T(E)) = ln(N_{T0}) - E/kT_2 \quad \text{(Trap states)}$$

In equation 1.5, N_{V0} and N_{T0} are density at reference energy (here E = 0) and $-E/kT_1$ and $-E/kT_2$ are slope of distribution when plotted in a logarithmic scale.

Effect of traps on electrical characteristics of devices can be summarized as [48]

- Low conductivity, which can also be possible because of low mobility.
- Thermal activation of current.
- Long lived transient effects. For exponentially distributed density of states (DOS), power law transients are expected in constant bias.

- In admittance, a non-constant Mott – Schottky plot is otherwise used to profile the acceptor concentration.
- Thin film transistors (TFT's) have nonlinear output and transfer curves and thermal activation energy depending on bias (Meyer – Neldel Rule).
- Anomalous Time of Flight (ToF) transients.

1.2.2 Charge Transport in Disordered Polymer Semiconductor

A basic understanding of charge carrier transport is essential for optimizing and improving the performance of devices based on polymer semiconductors. Transport in these disordered materials is governed by local structural and energetic disorder [53]. As far as basic conduction mechanism is concerned, free carriers and polarons [54] or bipolarons [55] are the two possible candidates for transport. Conduction can occur either via band transport or hopping transport model, where in band transport charges are delocalized and can travel freely. These charges may spend most of their times on localized deep state, not contributing to current and reducing average mobility. Poole – Frenkel conduction is an example of such mechanism, this mechanism includes field dependence of mobility. Multi – trap – and – release is another such example which is same as Poole – Frenkel but field dependence is removed. In hopping transport model only the localized sites exists or are important, as the delocalized levels are too far or temperature is too low to excite trapped carriers thermally [56]. Charges spend all their time on such localized states except during instantaneous hop between these states. As shown by the simulations of Bässler [57] such transport can also cause field and temperature dependence of mobility. Ambegaokar *et al.* [58] extended the work of Mott on hopping/percolation theory which predicts temperature dependence of conductivity as $\sigma \propto \exp\left[-(T_0/T)^{1/4}\right]$. Other mechanism of transport contains two band formalism, a conduction band and a defect band [59]. When defect band is dense enough, hopping can occur from defect to defect giving enough current [60]. This method can be nearest range hopping or variable range hopping (VRH) [61,62]. According to VRH charge carriers can hop up or down between two energetic states either by emitting or absorbing a phonon respectively. Carriers can hop over large distance with low activation energy or low distance with high activation energy.

Mobility of charge carriers is one of the important parameters in semiconductor physics, as the switching and other transport properties of devices depends on mobility of carriers. Mobility of the carriers strongly depend on the amount of disorder present in the system, there are several models which try to explain the disorder in the system. Scher and Montroll model (SM) describes the positional disorder in the system. Most commonly used model is Gaussian Disorder Model (GDM) which considers energetic disorders as well.

Scher and Montroll (SM) Model

In 1975, H. Scher and E. W. Montroll proposed a model [63] for transport in a-As_2Se_3 as well as trinitrofluorenone-polyvinylcarbazoles to explain the featureless current transient observed in Time of Flight (ToF) mobility measurement. Polymer semiconductors have many properties similar to amorphous inorganic semiconductors, thus when SM model is applied to polymer systems it can explain many of transient photocurrent features observed.

It is assumed that a Gaussian charge packet maintains its form [$\psi(t) \backsim \exp(-t/\tau)$] in non – dispersive transport till it reaches an electrode. While for dispersive transport they move non – uniformly, in SM model this property of Gaussian packet is described as time dependent random walk under electric field. The dispersion of hopping time is proposed to follow inverse power law as given by the equation 1.6.

$$I(t) \sim Const \times \begin{cases} t^{-(1-\alpha)} for \frac{t}{t_{tr}} < 1 \\ t^{-(1+\alpha)} for t/t_{tr} > 1 \end{cases} \quad (1.6)$$

In equation 1.6, $0 < \alpha < 1$ and t_{tr} is the carrier transit time across the device. In SM model, the assumption made is that due to the positional disorder there is a large distribution of hopping sites, which causes large waiting time between successive hopping. Thus the mean carrier velocity decreases and gets separated from the peak in time.

It is the inherent disorder in material which causes dispersive transport. SM model does not consider the energetic disorder and cannot explain temperature dependence of current transient. To explain the temperature dependence of transport in disordered materials other models were developed, like the GDM which considers the energetic disorder of the system.

Gaussian Disorder Model (GDM)

Fluctuations in local conjugation length, structural disorder and DOS in organic semiconductors are well represented by a Gaussian like distribution of molecular orbitals [50,64,65,66]. The transport between the localized sites is described by variable range hopping. The main assumptions that are made for this model are:-

1) A charge carrier can hop between localized states, which are distributed randomly in space and energetically according to some DOS function. In many calculations, the density of states is assumed to be Gaussian in nature [48]. Thus this model is also known as Gaussian disorder model. A schematic diagram for Gaussian distribution has been shown in Figure 1.6

2) The carrier has no information about previous hop, thus the "continuous band" like transport is excluded

3) The hopping rate between the sites is given by Miller – Abrahams rate or polaronic rate

4) The energies of adjacent sites are uncorrelated. This assumption was excluded by Novikov[67] and Gartstein – Conwell [68]

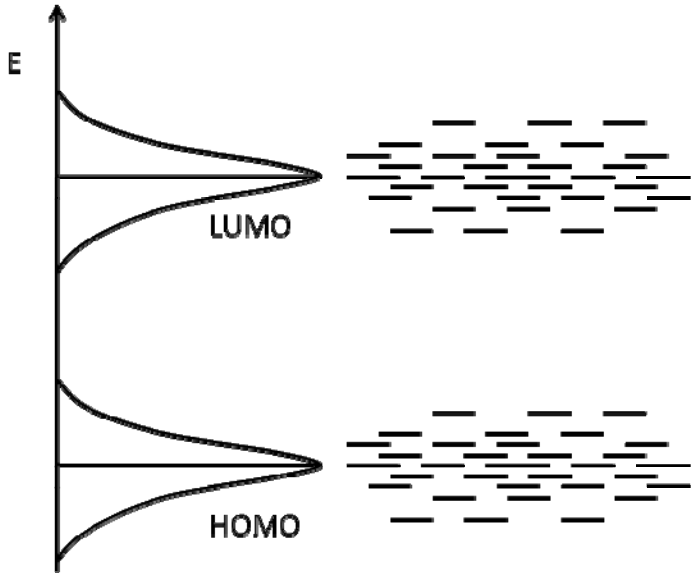

Figure 1.6 : Schematic representation of Gaussian distribution of state in energy and position space.

Field and temperature dependence of mobility as calculated from the GDM is given by

$$\mu(F,T) = \mu_o exp\left[-\left(\frac{2\sigma_E}{3k_BT}\right)^2\right] \times exp\left[C_0(\sigma_E^2 - \Sigma^2)\sqrt{F}\right] \quad (1.7)$$

It has been seen that the model shows large increase in mobility in a typical electric field $E \approx kT/R$ (where R can be localization radii) when the energy correlation is not considered, thus the Poole – Frenkel like behavior $\mu \sim exp(-\alpha(T)E^{0.5})$ cannot be explained. In materials with narrow DOS the mobility shows a negative slope when the temperature crosses T_0 [69]. Thus the polaronic effect on the hopping rate has to be taken into account [70,71], by including Marcus rate into GDM or by inserting Holstein theory with [72] or without [73] considering charge dipole interaction.

1.2.3 Photophysics of polymer semiconductors

Conjugated polymers can be described as quasi – one – dimensional semiconductors, with energy gaps typically such that in undoped material the absorption edge is in visible or near infrared regions of the spectrum. Second important characteristic of conjugates polymer is disorder, the chain length may be quite long, but the conjugation can be intruded by defects, which can be curves or bends, foreign atoms, cross links etc. For example, an average conjugation length in Poly(p-phenylenevinylene) (PPV), as deduced from many different evidences is 6 – 8 monomers. The optical properties of polymers, with degenerate ground state, like trans-polyacetylene are different from those with non-degenerate ground state (NDGS). Illumination of polymer sample with light, past the absorption edge, results in excitations of varity of entities or particles. It is not always clear if a given entity is primary or secondary excitation. Upon absorption of photon past the absorption edge, an electron is raised to the conduction band of LUMO and a hole is left in valance band or HOMO. There are many possibilities for the state of resulting electron hole pairs, which are summarized below,

Polarons

A primary requirement for the formation of polaron is that the electron and the hole should be separated far enough, such that they do not interact, which may result in formation of an exciton. This can happen if the electron and hole separate onto different chain, within femto

seconds of creation. Another possibility can be that, an electron or hole gets captured, within femtosecond time scale, by an impurity that provides lower energy level. Presence of an isolated electron or hole on a chain causes the deformation or relaxation of the chain, the relaxation time for polyacetylene chain has been calculated to be ~ 100 fs [74] . A polaron is a complex of charge and the resulting deformation, which is represented by P^+ or P^- depending upon the charge of the carrier. Generation of polaron by light is well known for PPV [75].

Singlet Exciton

An electron-hole pair can stay on the same chain bound by their coulomb force of attraction and chain deformation or relaxation; occurrence of such an event causes the formation of an exciton. They are singlet since the electron and hole created have opposite spin. Because of the existence of multiple levels in valance band and conduction band, in general more than one type of exciton can be created. The lowest energy exciton created between top most level of valance band and lower most level of conduction band is quite extended; for PPV the extent is of the order of 6 monomers(~ 4 nm) [76].

Biexciton

The biexciton can be seen as an excitonic molecule; it results from the excitation of a second exciton close to first on a given conjugated polymer segment. Biexciton in π – conjugated polymers have been predicted to be a stable excitation [77]. Biexcitons observed in PPV oligomer films are found to be unstable and decay to form interchain species in sub – picoseconds time scale [78].

Triplet exciton

Exposure of above band gap light creates singlet excitons, but can be converted to triplet by intersystem crossing [79,80]. The bound electron-hole pairs in triplet excitons have parallel spins. They are more strongly bound than singlet and have longer lifetimes.

Biploaron

Two like charges having opposite spins when bound together within the same length of conjugated polymer, gives rise to bipolaron. They occupy two levels in the energy gap. Existence of bipolaron in doped NDGS polymer has been accepted, orders of magnitude increase in conductivity, while only a slight change in magnetic susceptibility is an evidence for the existence of bipolaron in doped NDGS polymers. Calculations have shown that stability of biploaron in the absence of oppositely charged ion is questionable [81].

Excimers

An excimer is a complex formed between the excited and non excited state of the same molecular species, i.e. excited state of the molecule and its ground state. Stability of excimer arises from the overlap between π orbitals of two molecules. Molecules must be close enough in the range of 0.3 to 0.4 nm for sufficient interaction [82]. For a good π interaction, chains must be parallel over a distance of few monomers. An important feature of excimer is a lower frequency emission compared to molecule excited in isolation because of lower energy in the excimer state. Emission from excimers is long lived because of symmetry forbidden radiative transition to ground state.

Aggregates

Aggregates have their electronic wave function delocalized over two or more chains in excited as well as ground state. Thus aggregates provide an additional absorption as well as additional emission compared to dissolved polymer [82].

Polaron pairs

Portions of a polymer chain with insufficient length can give rise to an interchain excitation which is not as symmetric as excimers. An electron and hole on non-parallel nearest neighbor chains can give rise to characteristic chain deformation respectively. This type of excitation is called a polaron pair. It is bound by coulomb attraction of the pair, which is considerable when the chain is few tenths of nanometer apart. This excitation may also be called as charge transfer exciton or an indirect exciton [82].

Soliton

Ground state structure of trans–polyacetylene is degenerate [26], which gives rise to another type of defect or excitation called soliton *S* or anti–soliton $\overline{S}$. A soliton oe an anti-soliton is a portion of chain or a domain wall which separates two region of different bond alteration. These solitons are delocalized over 7-8 atomic sites. From a symmetric Hamiltonian like SSH Hamiltonian, it is found that the localized electronic state associated with the soliton lie at the midgap. Solitons can be neutral with spin half or charged positive or negative with spin zero [26].

The generated electron hole pair can move via drift or diffusion and give rise to photoconductivity. It has been seen that the singlet exciton binding energy in NGDS polymers is ~ 0.4 eV. The possible carriers of photocurrent in NGDS polymers are polarons and bipolarons rather than free electrons. The fast current transient photoconductivity, in conjugated polymers could be explained by displacement current generated by electric fields induced polarization of bound excitons instead of free charge carriers [83]. This proposal has been countered by number of arguments, like required exciton polarizability are far too large in comparison with measured value in single crystal polydiacetylene, which also represents well for PPV [84].

Singlet exciton, properties and dissociation

Singlet exciton binding energy E_b is defines as $E_b = E_g – E_a$. Where E_g is energy gap and E_a is absorption edge, value of E_g and E_a varies with conjugation length of the polymer. Since dissociation of excitons in polymers causes creation of polarons, the exciton binding energy may be defined as the energy required for dissociating an exciton into a pair of separated polarons. An exciton may decay radiatively or nonradiatively at room temperature with a typical life time ~ 100 ps. Singlet exciton life time in PPV is ~300 ps. Exciton decay profile may not be exponential, showing involvement of more than one process. It is expected that electronic excitations of the lattice leading to vibronic structures in emission and absorption. Effects are visible in emission at lower temperature as exciton tends to migrate to lower energy site, specifically to segments with longer conjugation length [85] before emitting. This idea is supported by the fact that photoluminescence is over a narrow range of frequencies than the

associated absorption. Along with the fact that emission observed after few ps of excitation is red shifted. These processes have been studied in site selective fluorescence spectroscopy, where emission spectrum is measured as a function of excitation energy. Occurrence of threshold in excitation energy, known as localization energy is a proof for exciton migration. It is determined by relative rates of exciton migration and decay [86,87].

Exciton decay can be caused by introduction of carbonyls [88,89] which can be introduced through photo-oxidation. The decay occurs with capturing of electron from exciton by the electronegative carbonyl oxygen, causing dissociation of exciton. Exciton dissociation, causing quenching of photoluminescence, can occur under high electric field. It has been demonstrated for MEH PPV that under a field of $2 \times 10^6 \mathrm{V/cm}$, 40% quenching occurs which increases with higher field [90]. Quenching evolves on a ps time scale, for excitation close to the absorption edge quenching has been modeled by Monte Carlo simulation. Fit to experimental data estimates the exciton binding energy at ~ 0.4 eV [91] or 0.3 ± 0.1 eV [92].

1.2.4 Charge Carrier loss mechanism

Loss of charge carriers is an important factor responsible for low efficiency of organic semiconductor based devices. In organic semiconductors, the recombination mechanisms can be dependent on the concentration of carriers, which decides how often two carriers see each other it can also be field driven. The carriers injected into the material can be captured at the trap centers for some time or can be lost through recombination. Any material contains impurity which forms localized states, which can be distributed or confined in the forbidden band gap region. Such states form traps or recombination centers. Recombination centers are qualitatively different from trap centers. A trap centre can specifically act as an electron trap or hole trap, while a recombination centre can first capture an electron (hole) and then the probability of annihilation of that charge by recombining with hole (electron) is higher as compared to being re-excited back to transport levels. A localized state can function as either trap center or recombination center depending upon various parameters like its position in the forbidden energy gap, concentration of charge carriers (free electrons and holes) and the capture cross section for electrons and holes.

The process of free carrier recombination can be classified in two major classes depending upon the process is radiative or nonradiative [93].

A) Radiative recombination

I) Band – to – band recombination by collision between free electron and hole.

II) Recombination through a recombination centre.

III) Two localized centers can recombine with each other.

IV) Exciton annihilation.

B) Non – Radiative recombination

I) Free electron and free hole recombine and energy is dissipated as phonon energy

II) Auger or impact recombination, which can involve electron-electron or hole - hole collision or electron – impurity collision.

III) Recombination through surface states.

Recombination which involves one free carrier at a time, like recombination through recombination centers is generally referred to as monomolecular recombination. The recombination involving two carriers in bimolecular mechanism, like in band – band recombination are called as bimolecular recombination. Recombination like Auger intrinsic recombination, which involves three bodies at a time are called as tri molecular or three body recombination.

For the recombination process which occurs through band – to – band transport and generally at high carrier densities the recombination rate can be defined by equation 1.8 [93].

$$\frac{dn}{dt} = \frac{dp}{dt} = -R = -C_r np \tag{1.8}$$

In equation 1.8, C_r is given by [93] ,

$$C_r = \langle \vartheta \sigma_r \rangle$$

Here, ϑ is microscopic relative velocity and σ_r is the recombination cross section. The indirect recombination can occur through recombination centers where free carriers of one type are captured first and then recombine with carriers of other type. For this type of recombination, the rate is given by [93],

$$R_a = \langle \vartheta \sigma_n \rangle n(N_{ra} - n_{ra})$$

$$R_a = \langle \vartheta \sigma_p \rangle p n_{ra} \tag{1.9}$$

For acceptor type recombination center, N_{ra} is the density of all the acceptor recombination centre and n_{ra} is the density of captured electrons. For donor type recombination center, the recombination rate is given by [93],

$$R_D = \langle \vartheta \sigma_p \rangle n n_{rd}$$

$$R_D = \langle \vartheta \sigma_p \rangle p(N_{rd} - n_{rd}) \tag{1.10}$$

In equation 1.10, N_{rd} and n_{rd} are the density of donor type recombination center and density of captured holes respectively. A monomolecular recombination rate can be approximated by n/τ. Non-geminate or bimolecular recombination rate can be given by Langavin theory where $R \propto \gamma(np - n_i^2)$ [94,95], where γ is Langavin recombination factor which for pristine material is given by $\gamma = e(\mu_e - \mu_p)/\varepsilon$, where ε is the dielectric constant of the material and n and p is free electron and hole concentration.

The organic semiconductors make one half of OI devices, while the other half is inorganic semiconductor. In present study we have used n- doped gallium nitride (n-GaN) as inorganic material. n-GaN is a member of nitride family of semiconductor. In the next section a brief introduction about the bulk properties of nitride semiconductors and GaN in particular will be presented.

1.3 Nitride Semiconductors

Inorganic semiconductors includes the elemental (Si, Ge) and compound (II-VI, III-V, IV-IV) semiconductor families. Among these semiconductors the current semiconductor industry mainly

runs on Si as the raw material, with more than 95% of fabrication carried out using Si wafers [96]. While II-VI family of compound semiconductors showed an alternative path for high speed and high power semiconductor electronics, it's the III-V family of semiconductor which drew more attention by showing applications in high power blue and UV LED. Among the III-V family, the family of nitrides has holds special importance, as the three members InN, GaN, and AlN cover the whole visible spectrum. The special interest in GaN arose from the fact that this semiconductor made the blue LEDs and UV lasers possible [96]. Among the vast family of nitrides, consisting of binary, ternary, and quaternary alloys, the GaN has been studied the most. Nitrides are partly ionic in nature and their band gap varies over a large range. AlN in wurtzitic form has a band gap of 6.2 eV, Wurtzite GaN has a band gap of 3.4 eV and the band gap of InN is 1.9 eV [97]. Nitride semiconductors and mostly GaN crystals are grown using epitaxy, bulk growth by dissolving nitrogen into melt gallium at 10 Kbar and 1600 ^{0} C is still not a viable method. Metal organic vapor phase epitaxy (MOVPE) techniques have been utilized for growth of GaN and its alloys. An efficient p – type doping of MOVPE grown GaN films [98] enables the step towards commercialization of GaN based LEDs.

GaN is different from another famous member of III – V family, GaAs. It is transparent with large band gap but still can conduct, the ionization energies of donor and acceptor, binding energy of exciton and phonon energies are much larger in GaN compared to GaAs. GaN based wide band gap semiconductors have several advantages over other wide gap semiconductors like SiC, they can be doped by both p- and n- type impurities, they are direct band gaps semiconductors and can form heterostructure favorable for device applications.

1.3.1 Crystal structure and Band diagram

Group III – nitrides crystallize in three common structures the wurtzitic (WR), zincblende, and the rock salt. At ambient conditions the WR structure is most stable for GaN, AlN, and InN [99]. The stable thin films of zincblende structure of GaN and InN has been grown on (001) crystal planes of cubic substrates, where the tendency to form WR polytype is overcome by topological compatibility. The rocksalt structure of GaN, AlN, and InN are stable at high pressures. The WR polytypic has a hexagonal unit cell, where the two lattice constants for GaN crystal are c = 5.185 Å and a = 3.189 Å. The structure contains six atoms of each type per

unit cell. The structure consists of two interpenetrating networks of hexagonal closed pack sublattices; each made of only one type of atoms and placed along the c axis with an offset of 5c/8. Space group of GaN in WR structure is $P6_3mc$ (C_{6v}^4) [100]. The unit cell of zincblende structure is cubic with four atoms of group III and four of nitrogen. The space group is $F\bar{4}3m$ (T_d^2). The cohesive energy per bond is 2.88 eV, 2.2 eV and 1.93 eV for AlN, GaN, and InN respectively [101]. Growth conditions, impurity concentrations, and film stoichiometry has significant effect on the lattice constant of III-N compounds. The Lattice constant for GaN grown with higher growth rates were found to be larger.

Theoretically several band structures have been presented for AlN and GaN with some crystal structures [102,103,104]. Most of them present charge density calculations, density of state calculation and other structural properties. The electronic band calculation for WR structure was performed using full potential linearized augmented plane wave (FLAPW) method by Masakatsu Suzuki et.al. [105]. Figure 1.7 (a) shows the first Brillouin zone for WR crystal structure and Figure 1.7 (b) the E versus k diagram for WR GaN without spin – orbit interaction.

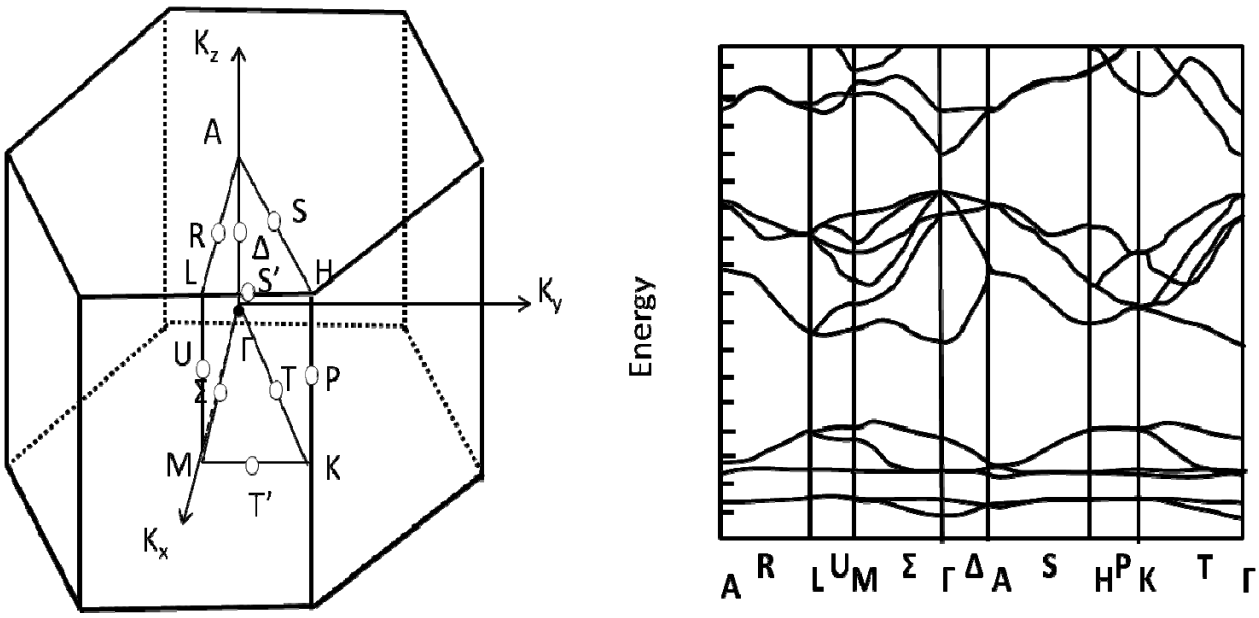

Figure 1.7 : a) First Brillouin zone for WR crystal structure and b) Schematic E versus k diagram for WR GaN. (E versus K adopted from [105])

The effective density of state in conduction band and valance band at 300 K is calculated to be ~ 10^{18} cm^{-3} [106]. The electronic band diagram shows that GaN is a direct band gap semiconductor, where the conduction band minimum is located at the Γ point (k=0).

1.3.2 Photo – excitation and charge transport

Nitride semiconductors are crystalline materials with optical band gap varying between 1.9 eV to 6.4 eV. The optical excitation of AlN is not possible in visible range of excitation. While GaN has been the most studied nitride among others, and is the inorganic part of our OI hybrid structure, we will look at the optical, photo conductivity and electrical transport of GaN in this section. GaN in its thermally stable form stays in WR crystal structure. The dielectric constant of this material is around 8.9 [107] and refractive index of 2.29 [108] at 300 K. Refractive index changes with temperature and photon energy and increases with increasing photon energy [106].

Photo – excitation

The intrinsic free excitations are the lowest energy excitation in GaN; the free excitation can be described by the Wannier – Mott type approximation. The electron and hole are treated to be independent, interacting via coulomb fields. This interaction causes lowering of bound state energy by an amount equal to exciton binding energy. The total energy of bound electron hole pair is given by the expression [109],

$$E_K = E_a + \hbar^2 \vec{K}^2 / 2(m_e^* + m_h^*) \tag{1.11}$$

In equation 1.11, m_e^* and m_h^* are effective masses of electron and hole and E_a is given by [109]

$$E_a = e^2 \mu / 2(4\pi \hbar e)^2 n^2 \tag{1.12}$$

Here, $\mu = \left({}^{1}/_{m_e^*} + {}^{1}/_{m_h^*}\right)$ is the reduced mass. Bound exciton is a complex formed between exciton and impurity. This can happen when an impurity captures a free exciton or it captures an electron or hole and then carrier of other charge. Exciton can get bound to neutral or ionized donor or acceptor. An important recombination process is annihilation of bound exciton [109].

Photoconductivity

Conductivity of a semiconductor material is a sum of free electron and hole conductivity, and is given by,

$$\sigma = q(\mu_e n_e + \mu_h n_h) \tag{1.13}$$

In equation 1.13, τ_e and τ_h are free electron and hole life times. When exposed to excitation wavelength, extra electron-hole pairs are created giving rise to photoconductivity $\Delta\sigma$. The corresponding photo induced current is proportional to flux of incident photon, the generation efficiency of electron-hole pair, area of the semiconductor, and charge of carriers.

$$I_{ph} = q\eta A\phi g \tag{1.14}$$

In equation 1.14, η is quantum efficiency of the material, ϕ is the input photon flux and g is the photoconductive gain. Photocurrent measurements using thermally simulated current and photoconductivity experiment can give information about the activation energy and energy level of deep traps respectively [110].

In many studies of photoconductivity, it is possible to make two simplified assumptions [111]

1) Conductivity is dominated by one of the carrier (majority carrier) so that the contribution of the other can be effectively neglected.
2) The crystal stays neutral during the photoconductivity process without any build up of appreciable space charge in the crystal; i.e. $\Delta p = \Delta n$.

A key parameter to understand photoconductivity is carrier life time. If f number of charge pairs are generated after photo excitation then $\Delta n = f\tau_n$ and $\Delta p = f\tau_p$. Where τ_n and τ_p are the free electron and hole life time. The photoconductivity is given by,

$$\Delta\sigma = fe\left(\tau_n\mu_n + \tau_p\mu_p\right) \tag{1.15}$$

This makes the role of lifetime important in photoconductivity. Free carrier life time, excited state lifetime, pair life time, minority and majority carrier life times are important in the studies of photoconductivity of nitride semiconductors.

Charge transport in Nitrides

For epitaxially grown GaN films, the carrier transport is assumed to be in plane perpendicular to growth direction. The GaN films grown on c-plane sapphire are polarized; they can be either N – polar or Ga – polar depending upon which face is on top. The carrier transport

is generally described through band transport. The carrier transport can be either a vertical junction transport or a lateral transport depending upon which way the carrier moves. Vertical transport controls the transport in devices like diodes and other two terminal structures, lateral transport controls the motion in channel, between source and drain in field effect transistors.

The vertical junction transport can be modeled using one dimensional drift diffusion charge control model. In this model the semiconductor interface is treated as an abrupt interface, and the boundary condition for heterojunction interface is given by [112],

$$\epsilon_1 E_1 + P_1 = \epsilon_2 E_2 \tag{1.16}$$

In equation 1.16, $\epsilon_1$and ϵ_2 are the dielectric constants of two sides, E_1 and E_2 are the electric field at the two sides of the interface and P_1 the polarization. Under this boundary condition, Poisson's equation can be written as [112],

$$\nabla^2 E_c = -\frac{\rho}{\varepsilon} \tag{1.17}$$

The variation in charge and polarization is only along z axis, thus the Poisson's equation can be converted to one dimensional form along z axis [112],

$$\frac{d^2}{dz^2} E_c(z) = -\frac{\rho(z)}{\varepsilon} \tag{1.18}$$

The charge density ρ(z) is given by [112],

$$\rho(z) = q(N_d^*(z) - N_a^*(z)) - nf_{free}(z) + p_{free}(z) - \sum_i n_i \psi_i^*(z)\psi_i(z) \tag{1.19}$$

In equation 1.19, $N_d^*$and N_a^* are effective doping concentration and n_{free} and p_{free} are free carrier concentration. The occupation n_i is given by [112],

$$n_i = \frac{m_i k_B T}{\pi \hbar^2} ln\left[1 + exp\left(\frac{E_i - E_F}{k_B T}\right)\right] \tag{1.20}$$

Sub-band envelop function, ψ_i, is obtained by solving time independent Schrödinger equation. The drift-diffusion equation is solved for injected current in the device. While the current is flowing in the device the Fermi level splits in two quasi levels, which can be obtained by solving drift – diffusion equation given by [112],

$$J_n = -\mu_n n(z)\frac{dE_c}{dz} + qD_n\frac{dn(z)}{dz} \tag{1.21}$$

$$J_p = -\mu_p p(z)\frac{dE_v}{dz} + qD_p\frac{dp(z)}{dz} \tag{1.22}$$

Now, using continuity equation, this is given by [112],

$$\frac{dJ_n}{dz} = qR \text{ and } \frac{dJ_p}{dz} = -qR \tag{1.23}$$

R is the Shockley – Read – Hill rate. Calculated quasi Fermi level can be used with Poisson equation to model charge transport along vertical direction. Effect of trap centers can be included by including terms for electron and hole traps in the charge density ρ(z) expression. The tunneling current in 3D can be given by using WKB approximation [112].

$$J_{3D} = q\int_{E_{n2D}}^{\infty}\int_{0}^{\infty} \nu(E_l, E_f)D_{iD}(E_l)E_{2D}(E_t)\Big(f\big(E_{tot}, E_{fs}, T\big) - f\big(E_{tot}, E_{fm}, T\big)\Big) \times T(E_l, E_t)dE_l dE_t \tag{1.24}$$

Thermionic emission in the material can be accounted by increasing the range of energies above the height of classically forbidden barrier.

For lateral movement of carriers, the transport is simulated using Monte Carlo method. Fermi – Golden Rule is used to describe the scattering of carriers caused by the surface roughness, dislocations and other factors.

Some experimentally measured charge transport parameters for GaN in WR crystal structure are,

1) Drift Velocity ~ 10^7 cm/s at 10^2Kv/cm [113]
2) Dark Conductivity σ ~ 0.5 $\Omega^{-1}cm^{-1}$ at 300 K [114]
3) Electron mobility $\mu_n \leq 440$ cm^2/Vs at 300 K [114]
4) Hole mobility $\mu_p \leq 200$ cm^2/Vs at 300 K [115]
5) Diffusion Coefficient of electron, D_n 25 cm^2/s, at 300 K[115]
6) Diffusion Coefficient of hole, D_p 5 cm^2/s at 300 K [115]

These basic transport parameters depend on material quality and defect concentration. The value changes with temperature and carrier concentration.

1.4 Organic – Inorganic Hybrid Systems

The hybrid organic – inorganic (OI) device structures have been studied extensively for applications in solar cells [116,117], hybrid LED's [118] photodetectors [19,119,120] and hybrid transistors [121]. Hybrid semiconducting materials and device structures give a versatile class of new semiconductors that can offer completely new optoelectronic properties. The search of new hybrid semiconducting materials and device structures were motivated by the fact that these hybrid structures do not require any lattice matching for growth. For epitaxially grown OI epilayer the lattice mismatch constraints can be relaxed greatly, this type of structures also give an access to a completely new type of properties [122]. A great deal of effort has been given for chemical route of synthesis of OI hybrid structures [123,124,125].

Along with chemical route for synthesizing functionally hybrid materials, the studies on hybrid structures fabricated using thin film deposition techniques have also shown tremendous potential in tailoring the electronic and optical properties [126,127]. Thermally deposited organic thin films on Si and GaN have been studied extensively for their novel optoelectronic properties [128,129]. Solution processable polymer thin film methods can provide a still lower cost device fabrication alternative for hybrid structures [130,131]. Solution based methods provide low temperature fabrication method for OI hybrid device structures which can be easily employed for large scale fabrication.

A better understanding of devices operation requires better understanding of the basic charge transport mechanisms, and efficiency limiting processes like trapping and recombination. In the following sections a basic charge transport mechanism in OI hybrid structures will be presented. A basic idea about the structural defects and related trapping and recombination mechanisms will be discussed. A glimpse of possible directions for applications

of OI hybrid heterojunction devices will be given. The Motivation for this work is to explore the basic mechanisms underlying the complex processes in OI devices.

1.4.1 p-n junction versus OI junction

An OI HJ is very different from a traditional p-n junction, more specifically p-n homojunction. A p-n junction (homojunction) is made up of same semiconducting material with different doping atoms and levels, which gives rise to p- or n- doped regions. The doping concentration may vary from p- to n- side. The key features of a p-n homojunction can be summarized as:

1) Formation of space charge region across the metallurgical junction
2) Zero mobile carrier space charge in the depletion region
3) A continuous band bending across the interface, with almost zero trap states.
4) Electric field varies linearly in the space charge region. The strength of electric field is largest at the metallurgical junction, and twice the average value in magnitude.
5) Under thermal and electrical equilibrium, the field is present only across the space charge region, for comparable doping concentration on either side.
6) Electric potential variation parabolic in the space charge region.
7) In a p^+/n type junction the space charge layer is mainly on the lower doped side of the p^+/n boundary.
8) The current voltage characteristics is given by Shockley diode equation [132],

$$J = J_{sat}\left[exp\left(qV/k_BT\right) - 1\right] \tag{1.25}$$

In equation 1.25, J_{sat} is the saturation current density given by [132],

$$J_{sat} = J_{p0} + J_{n0} = \left(qD_pP_n/L_p\right) + \left(qD_nN_p/L_n\right) \tag{1.26}$$

In equation 1.26, q is the electrical charge, D_p is the minority hole diffusion coefficient on n-side, P-n is the minority hole concentration and L_p is the minority hole diffusion length on the n-side.

Similarly D_n, N_p and L_n are the diffusion coefficient, electron concentration and electron diffusion length of minority electron on p-side respectively. Figure 1.8 shows equilibrium energy band diagram for a p-n homojunction. Standard notations have been used for energy levels. qV_{bi} represents the built in filed and χ is the electron affinity of the semiconducting material.

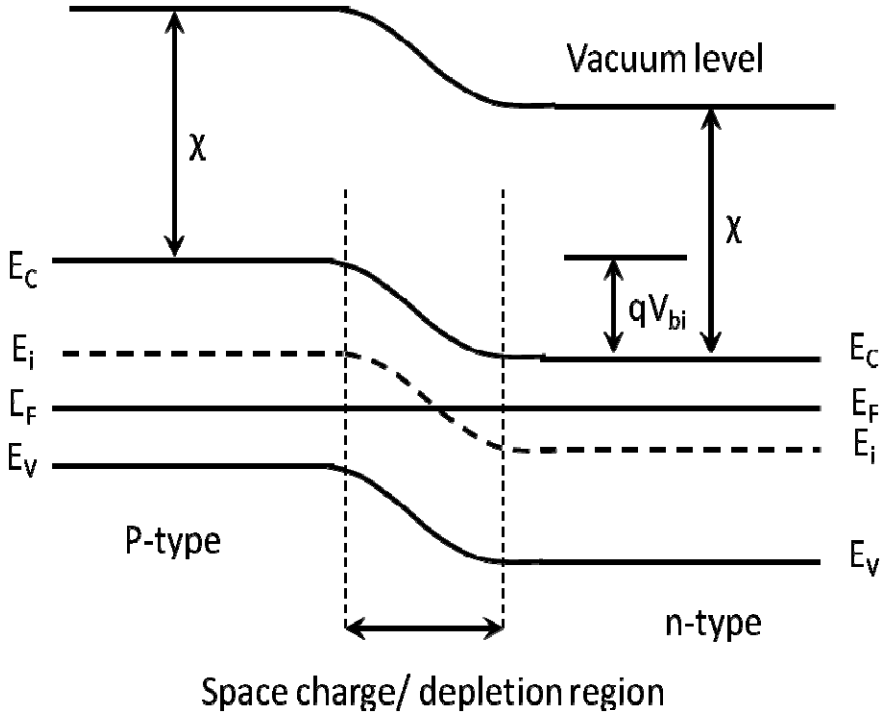

Figure 1.8 : Energy band diagram for p-n homojunction diode.

The terminal current in case of p-n homojunction is limited by carrier recombination – generation in the space charge region under reverse bias or below the forward injection voltage V_{Th}. For low forward current and above V_{Th}, the minority carrier diffusion recombination in the two quasi neutral layers determines the terminal current.

The junction between the organic and inorganic layer in OI HJ devices are closer to crystalline semiconductor–disordered semiconductor (s-s) heterojunction, which are made of two dissimilar semiconductor materials. Figure 1.9 (a) shows the flat band diagram and Figure 1.9 (b) equilibrium band structure for crystalline s-s heterostructure. The interface properties in a true s-s heterostructure are dominated by the traps which originate from dangling bonds, lattice mismatch and presence of foreign impurity atoms. If charged the traps can alter the amount of

energy band bending at the two semiconductor surfaces. This will give barrier height for electron which will differ from work function difference ΔE_{C21} Figure 1.10 shows a band structure for trap filled interface.

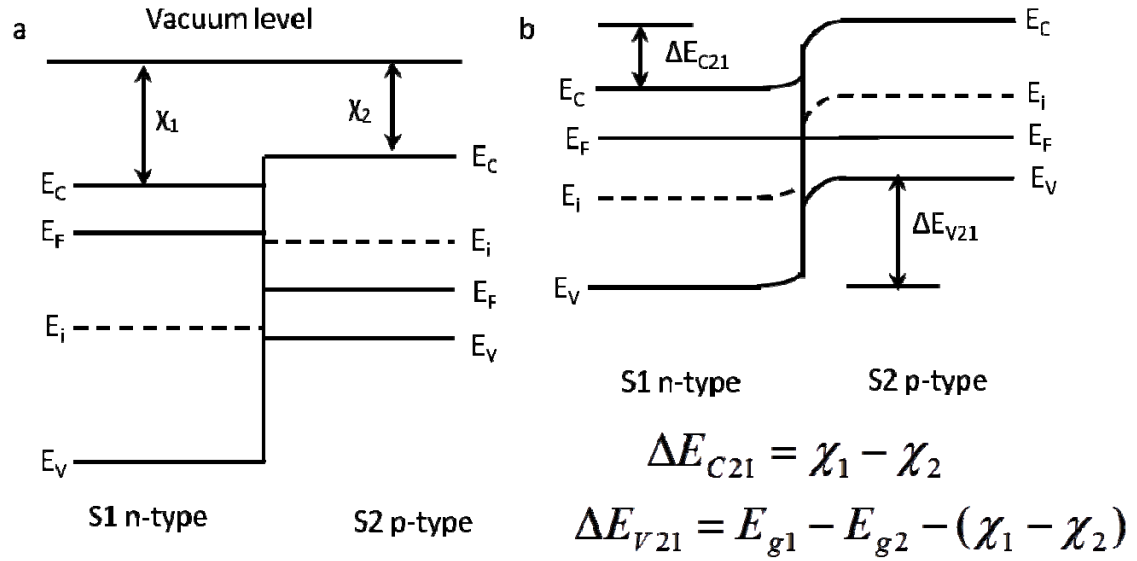

Figure 1.9 : a) Flat band Energy diagram and b) equilibrium energy diagram for inorganic s-s heterostructure [132].

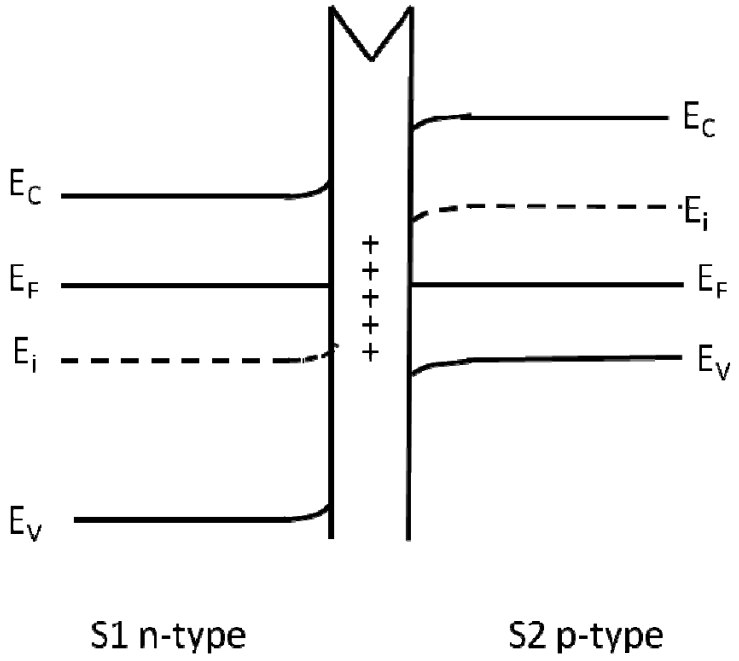

Figure 1.10 : Energy band diagram for trap dominated s-s heterostructure interface.

The current voltage characteristics of s-s heterostructure can be derived from the Shockley and SNS diode equations with apparent discontinuity at the heterointerface boundary. In case of OI HJ systems one active layer is donor or acceptor polymer semiconductor which do not have any doping carriers. The energy structure for OI structures can be different compared to actual s-s heterostructure. Unlike the case of doped semiconductor junction, in polymer semiconductor the electric field may not be confined only to depletion region but can be distributed over entire bulk of the polymer. Thus the bulk energy band structure, for organic semiconductors, will deviate from the flat band consideration. Figure 1.11 shows a schematic band structure for OI HJ, effect of field on the bulk of semiconductor has been shown, along with band discontinuity and interface band bending.

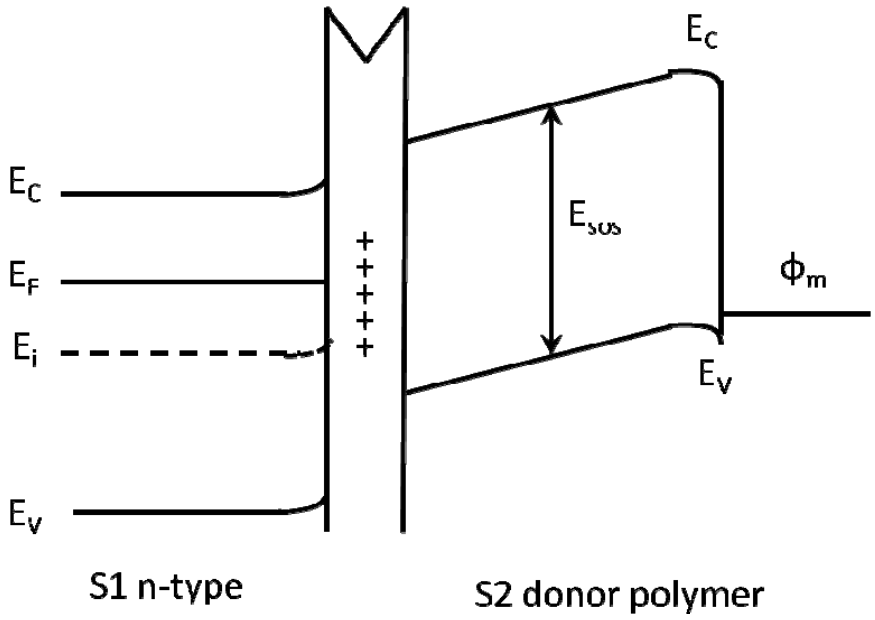

Figure 1.11 : Energy band diagram for OI hybrid structure with n-doped inorganic layer and donor polymer semiconductor.

1.4.2 I-V models

The charge transport or current – voltage characteristic of metal-organic-inorganic device can be understood by assuming that transport within the organic material is determined by carrier injection from the contacts, and ultimately by the space charge in organic semiconductor. To

have a basic understanding of carrier transport mechanisms in these OI devices, we can take an example of insulator with one ohmic and one blocking contact. A band diagram for n-type inorganic and p-type organic semiconductor OI HJ has been shown in Figure 1.12, where t is the organic layer thickness and W is the width of depletion layer. Barrier energy of $q\phi_B$ exists at the OI semiconductor interface. V_F is the externally applied forward bias and V_R is the externally applied reverse bias. Dashed line represents the energy band structure under forward bias and solid line represents energy band structure under reverse bias.

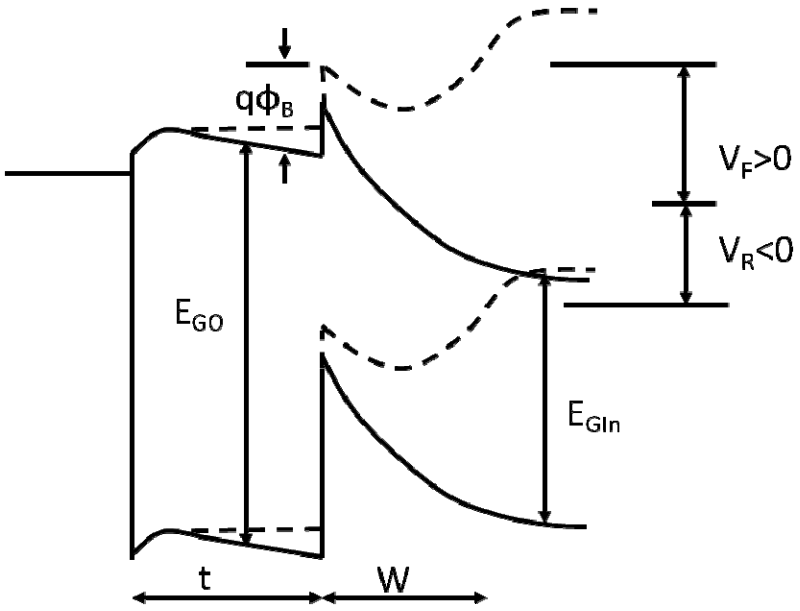

Figure 1.12 : Schematic representation of forward biased and reverse biased OI heterojunction band diagram (Adopted from [133]).

The current density for electron and hole transport can be given by,

$$J_n = q\mu_n nE \tag{1.27}$$

$$J_p = q\mu_p pE \tag{1.28}$$

Total current density J_{tot} is given by, $J_{tot} = J_n + J_p$

(n,p) are the total carrier density given by [133]

$$p = p_0 + p_{inj} = N_v \exp\left[\left(E_v - F_p\right)/kT\right] \tag{1.29}$$

N_v is the density of states at the valance band edge (E_v). F_p is the quasi Fermi energy for hole.

From continuity equation,

$$\frac{dJ_{tot}}{dx} = \frac{dJ_n}{dx} = \frac{dJ_p}{dx} = 0 \tag{1.30}$$

In the absence of recombination, this argument is valid for all x, using equation 1.27, 1.28 and 1.30 along with Poisson's equation; the electric field distribution in the space charge layer [133] can be given by,

$$E_{Sc}(x) = \left(\frac{-2J_{tot}x[\xi - 1]}{\varepsilon(\mu_p + \mu_n\xi)}\right)^{1/2} \tag{1.31}$$

Where $\xi = {}^{n}/_{p} = constant$

Electric field $E_{SC} = 0$, at the ohmic injection electrode. Using $E = -{}^{dV}/_{dx}$ and setting x = d, current density in the film of thickness t can be given by [133],

$$J_{tot} = -\frac{9}{8}\frac{\varepsilon(\mu_p + \mu_n\xi)}{\xi - 1}\frac{V_{Sc}^2}{t^3} \tag{1.32}$$

In equation 1.32, V_{Sc} is the drop across the space charge region. At a very small applied voltage, the density of electron at the blocking interface is given by [133],

$$n_d = N_C exp\left(-q\phi_B/_{kT}\right) \tag{1.33}$$

In equation 1.33, ϕ_B is the barrier for electron at the interface. For $q\phi_B \approx 1$ eV, n_d will be vanishingly small and the space charge current density equation gives rise to Mott – Gurney [134] equation.

$$J_{tot} = -\frac{9}{8}\varepsilon\mu_{carrier}\frac{V_{Sc}^2}{t^3} \tag{1.34}$$

At low current density, injection limited processes dominate and continuity of electron and hole current leads to the expression for thermionic emission in OI HJ [133].

$$J_{Th} = J_{Sat}\left\{exp\left(qV_D/nkT\right) - 1\right\} \tag{1.35}$$

The saturation current density J_{sat} is given by [133],

$$J_{Sat} = A^*T^2 exp\left[-q(\phi_B - \Delta\phi)/kT\right] \tag{1.36}$$

In equation 1.36, $\Delta\phi$ is the image force barrier lowering, and n is the diode ideality factor.

The analogy of MS Schottky barrier may not be completely correct for OI HJ. As the inorganic side at low voltages does not have the same boundary conditions as that for the metal layer. A bias dependent barrier height can be expected at higher voltages. In order to have a detailed picture of charge transport in OI HJ two quantities are essential [135],

a) Position of the non equilibrium or quasi Fermi level.

b) Charge carrier velocity throughout the heterojunction region.

Using these quantities, the surface states of inorganic material can be quantified using a technique called organic – on – inorganic surface analysis spectroscopy. When organic layer is deposited over inorganic material, a rectifying heterojunction is formed which determines the I-V characteristics. An assumption is made that the current density in the low current limit is controlled by the thermionic emission across the OI HJ interface and in the high current limit is dominated by the trap-free space-charge effects. The potential and field distribution inside the device can be determined using Gauss's law assuming single carrier hole injection [135].

$$\frac{dE}{dx} = \frac{q[\rho(x) - \rho_0]}{\varepsilon} \tag{1.37}$$

In equation 1.37, ρ_0 is the equilibrium hole concentration and ρ (x) is the sum of equilibrium and injection carriers. Under an assumption of constant carrier mobility under small field, the current density within the film can be given by [135],

$$J = q\rho(x)\mu_{carrier}E(x) \tag{1.38}$$

This equation is independent of position, and is a result of charge conservation (with the assumption of no trapping). The solution to these equations for a voltage drop V_0 across the organic film of thickness t is given by [135]

$$\frac{q^3\rho_0^3\mu_{carrier}^2 V_0}{\varepsilon J^2} = u_t^2 - u_t - ln(1+u_t) \tag{1.39}$$

The current J is given by [135],

$$J = q^2\rho_0^2\mu_{carrier}t/\{[1-u_t-ln(1-u_t)]\varepsilon\} \tag{1.40}$$

In equation 1.40, $u_t = {}^{\rho_0}/_{\rho(t)}$, at x = t,

Voltage across the thin film can be calculated by solving the above equations for a given J. When $V < V_0$, $J \propto V$ and when $V > V_0$, $J \propto V_0^2$, where V_0 is the transition field. For small forward voltage and even for leaky OI HJ, the quasi Fermi level is determined by the injected carrier concentration. To calculate the potential distribution across the film the V_0 is replaced by V(x) and solved for u(x) < u(t), where x is calculated using [135],

$$\frac{q^2\rho_0^2\mu_{carrier}x}{\varepsilon J} = -u(x) - ln(1+u(x)) \tag{1.41}$$

Charge distribution as a function of x can be calculated using u(x) and V(x). The current on the organic side of the heterojunction can be expressed as [135]

$$J(t) = J = q[\rho_s(V_D) - \rho_s(0)]\langle v_c\rangle \tag{1.42}$$

In equation 1.42, $\rho_s(V_D)$ is the hole density at the OI interface corresponding to the lowest point in the VB maxima at the inorganic semiconductor interface, V_D is the voltage drop across the inorganic substrate. This equation suggests that the injected current from the OI interface into organic thin film is limited by the rate at which carrier moves to the other electrode. The average carrier velocity $\langle v_c\rangle$ is calculated using x dependence of mobility and electric field. This formalism considers only drift current, but the diffusion component becomes important at $V_0 \cong kT/q$. When diffusion component is significant, the drift velocity is replaced by [135],

$$\langle v_c \rangle = \left({}^{D}/_{\tau} \right)^{1/2} = \left({}^{\mu kT}/_{q\tau} \right)^{1/2} \tag{1.43}$$

The current on the inorganic side of the HJ is given by [135]

$$J = qD_{sc}\left(\frac{q\rho E}{kT} - \frac{d\rho(x)}{dx}\right) \tag{1.44}$$

Here, D_{sc} is the diffusion constant for holes in the inorganic semiconductor. This equation can be solved for spatial dependence of charge density and current on the organic side of the heterojunction to give a total current density given by [135],

$$J = [qN_{vs}\langle v_c \rangle/(1 + \langle v_c \rangle/v_d)] \times \exp\left({}^{-q\phi_B}/_{kT}\right)\left[\exp\left({}^{-qV_D}/_{kT}\right) - 1\right] \tag{1.45}$$

In equation 1.45, ϕ_B is the barrier height and v_d is the carrier diffusion velocity in inorganic material. This expression for current density is similar to one obtained for thermionic emission in Schottky barrier [136], with the exception that the ϕ_B can be voltage dependent under the strong forward biased current injection for OI diodes. The conduction mechanism approaches an ideal Schottky barrier under strong forward injection. From the voltage consideration, it can be said that at lower applied voltages current is exponentially dependent on applied field and at higher forward voltage, the current density dependence on applied field is given by $J \propto \sim V^2$. Band bending parameter and quasi Fermi level on either side of the OI HJ can be calculated using valance band effective density of states and spatial distribution of charge density.

1.4.3 Interface states

Structural and electronic properties of the interface between organic and inorganic component of OI HJ devices is an important issue in device performance, as it determines the charge injection and charge flow in the device. Along with the knowledge of barrier height at the interface, type of interaction, physisorption or chemisorption can also significantly affect the

device performance. For many cases, charge transfer or chemical reaction has been observed between organic molecule and potential electrodes [137,138]. Such a situation can result in localized electronic states, which can act as charge carrier trap [139,140]. It has been seen that the device characteristics are dependent on the anisotropy of the transport properties in the organic thin films [141].

Interfacial electronic properties can depend on the crystal perfection and surface roughness of inorganic material [142], the way an organic semiconductor is adsorbed to the surface. Various growth modes observed on various substrates can be explained in terms of substrate molecule interaction. When the molecule – molecule interaction is greater than molecule – substrate interaction, molecules will be adsorbed standing on the substrate (i.e. molecular plane will be perpendicular to the substrate plane), as shown in figure 1.13. (a), while in other case, they will be adsorbed in lying geometry (i.e. molecular plane will be parallel to the substrate plane), as shown in Figure 1.13 (b). This effect has been observed for many metal, semiconductor and alkali halide substrates [143,144]. For a polycrystalline substrate, there is no well defined adsorption site for a large organic molecule because of the roughness of the surface on a molecular scale. Thus, a standing geometry is favored for a significant part of first monolayer, which is the determining process for the growth mode [145].

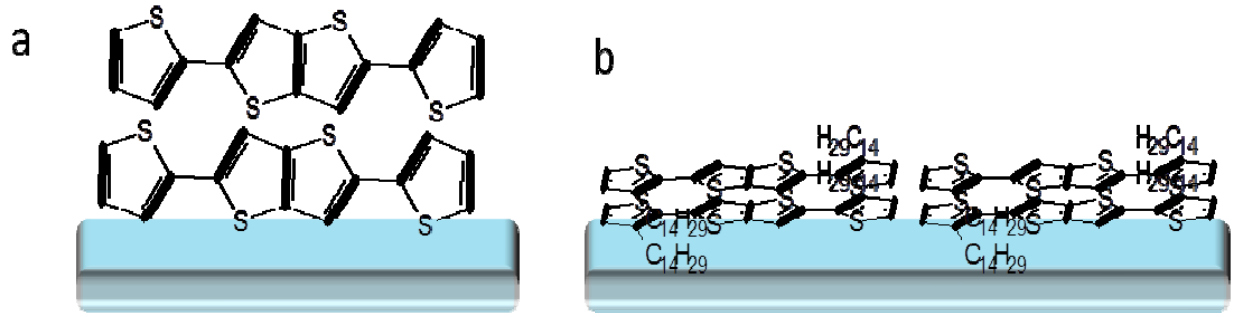

Figure 1.13 : Schematic representation of a) perpendicular b) parallel alignment between substrate and molecule.

A contact between organic and inorganic layer allows thermal equilibrium by equalizing the chemical potential. This may also results in formation of interface dipoles or bending of bands near the interface [146], as shown in Figure 1.14. Studies show a huge variation of the energy level of the organic semiconductor within few nm from the interface and rather small variation at larger distance. This observation has been interpreted as the formation of local

interface dipoles [147]. A number of mechanisms have been proposed for the formation of interface dipoles including chemical reaction, ion formation, mirror forces on the surface electronic rearrangement as well as the presence of permanent dipole at the interface in case of some organic molecules [147,148].

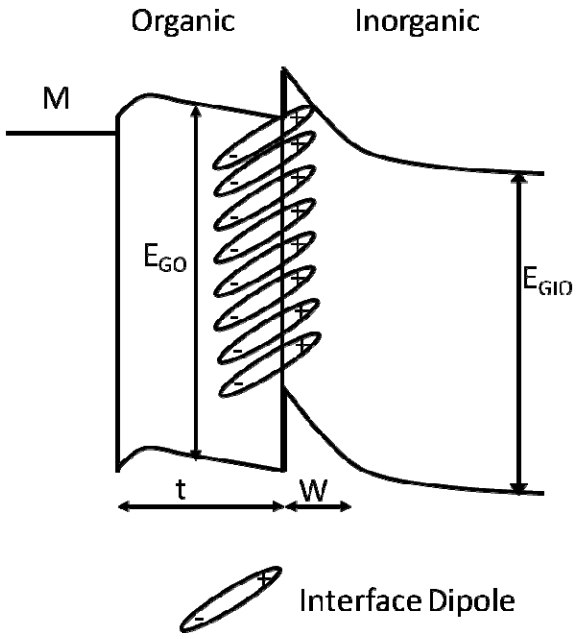

Figure 1.14 : A schematic diagram for band bending and dipoles present at the interface**.**

Localized interface states can act as the trap states for the charge carriers. If the rate of release from such a trap is less than the recombination rate then the trap centers can also act as recombination centers. The same state may act like a trap or a recombination center depending upon the conditions like temperature, majority to minority carrier ratio. Traps affect strongly the charge transport properties; their coulombic charge will influence the electric field distribution in the device and the transport. If the release rate from a trap is sufficiently low, than the time required to reach quasi thermal equilibrium conditions will be large. This can cause delay and hysteresis effect in electrical characteristics. Several effects of trapping have been observed in terms of the mobility parameter, few are listed below,

1) Dependence of space charge mobility on contact metal electrode.
2) Thermal activation of carrier mobility.
3) Dependence of carrier mobility on crystallinity of thin film.

4) Thermal activation of conductivity.

The effect of trap states on space charge current is seen as an introduction of effective mobility in place of free electron mobility in Mott-Gurney expression for space charge [133].

$$J_T = \left({}^{9}/_{8}\right)\varepsilon\mu_{eff}\,{}^{V_{sc}^2}/_{d^3} \tag{1.46}$$

$$\mu_{eff} = \theta\mu_p, \theta = {}^{p}/_{p_T} < 1 \tag{1.47}$$

In equation 1.47, p_T is the number of trapped carriers. Under the trap dominated transport, the space charge equation leads to Child – Langmuir law $J_t = B\left(d, \mu_p, T\right)V_{sc}^2$. The activation energy of space charge current can give the energy level of trap.

The presence of interface states will have an effect of screening the space charge layer in the bulk, giving rise to change in the slope of $\ln(I)$ versus V plot, which will be prominent in case of high surface states density [149].

1.4.4 Examples of Organic – Inorganic Hybrid systems

Hybrid semiconductor heterojunction systems are not very new, the first reports on such systems dates back to early 80's [150, 120,151]. Since then a continuous development in the studies on various OI HJ hybrid systems have been observed [152,153,154]. A complete description of dark charge transport properties and interface band structure for silicon – PTCDA (3,4,9,IO-perylenetetracarboxylic dianhydride) OI HJ has been presented by Forrest et.al. [19,133,135,]. An important point while exploring the properties of OI hybrid heterostructure lies in the understanding of interface states and charge transport across the OI HJ interface.

1) **Organic/Silicon OI HJ hybrid** – Hybrid structures using n-Si or p-Si are very well studied. Small molecules like PTCDA [19], CuPc [155], P3HT [156], MEH PPV [157] etc, have been used along with silicon to make hybrid diodes and solar cells. These devices show large rectification ratios and in some cases good power conversion efficiency (~ 10%) [116]. Fast detectors with large band widths have been made using Si/Organic hybrid materials [19,158].

These structures form an efficient model system for understanding the transport in OI HJ hybrids.

2) **Organic/GaAs OI HJ hybrid** – Hybrid structures using GaAs as inorganic material has also been studies widely [159,160]. With high rectification ratios and applications in organic – inorganic amplifier this structure promises a potential application. A nonradiative energy transfer from GaAs quantum well to organic over layer has been shown [153], which provides a nonradiative, noncontact method for carrier injection into the polymer.
3) **Organic/GaN OI HJ hybrid** – This system has been given a considerable importance because of the UV absorbing and emitting properties of GaN which is not available in other inorganic material. Blue LED and its market has seen a large progress with the introduction of GaN based LED's. As the detector technology evolves, the GaN based detectors are showing potential applications. Using organic donor layer with n-doped GaN provides an alternative for p-doped GaN, which is difficult to grow because of the background n-concentration present in the epitaxially grown films. Variety of organic – GaN based hybrid structures have been studied by various groups which show considerable effects of organic layer on the interface band bending.

Thus it can be inferred that the organic – inorganic hybrid systems show a considerable amount of potential for various semiconductor device applications. Combining the novel properties of organic and inorganic materials to give new optoelectronic properties and better device structures require a great deal of effort in understanding the basic dark and photoconductivity mechanisms. The introduction of oxide based layers in OPV's [161,162,163] also requires a better understanding of charge transport mechanism and efficiency limiting steps between the organic and inorganic semiconductor materials.

1.4.5 Problems with OI hybrids

Though the OI hybrid materials have shown potential for application in the field of various semiconductor technologies, many engineering and scientific challenges need to be answered. Hybrid systems have the advantage of utilizing the properties of organic and inorganic materials simultaneously, which include higher mobility of inorganic materials, large bandwidth of absorption of organic materials, significantly higher absorption cross section and ease of

fabrication. With these large amounts of benefits, there are many problems with these devices, which stem from the fact that the natural structure of these two components is not identical. Inorganic semiconductors offer a high degree of crystallinity and high carrier mobility which is lacked by the organic polymeric semiconductors. Thus, the junction between the organic and inorganic materials in OI hybrid is not only a metallurgical junction, but is a junction of different electronic, optical, mechanical and thermal properties. These striking changes in various properties give rise to many defects and interface states in the OI devices. As was discussed in the previous sections, the interface properties between inorganic and organic semiconductors is a function of their workfunction, charge density, bonding mismatch, surface roughness, and many other factors. The influence of these defects and disorders can modify the electrical and optical properties significantly, giving properties completely different from those expected.

In order to have miscellaneous applications of OI HJ devices in the active semiconductor technology, definite solutions to structural problems are expected in terms of structural engineering and material modification. A better understanding of charge transport in the bulk and across the interface along with the influence of interface states and traps is required. The photo-physics of OI devices depend largely on the generated photo carrier density and respective carrier lifetimes, which have a significant contribution from the interface and bulk traps. Modeling the current-voltage characteristics and spectral photocurrent response of OI devices are essential to understand the observed characteristics and related physical mechanisms.

1.5 Overview and Scope of the thesis

Organic – inorganic hybrid heterostructures are a relatively new class of electronic structures, incorporating the novel features of both the generations of semiconductors into a single device structure. Even though the initial studies date back to early 80's, the studies cannot be generalized for all the materials and structures. Recently, the possibilities of exploring wider range of materials have created a considerable interest in the area of OI hybrids. A thorough understanding of the charge transport, interface states and photoconductivity is essential for successful application of these new materials in consumer market. In this regard we have carried out studies on the GaN/polymer based hybrid system, to understand the steady state properties and photoconductivity as a function of various parameters which are important for determining the electronic transport in an OI hybrid system

The model OI HJ system selected for current study consists mainly of p-type donor polymer semiconductors, and n-doped GaN. N-type acceptor polymer N2200 has also been studied in some cases. The choice of this system is motivated by the fact that donor polymer semiconductors are readily available with a wide range of spectral coverage and band gap; a few of the commonly used donor polymers have been shown in Figure 1.15. Availability of such a large variety of materials gives flexibility of selecting the absorption region and device structure for application. The donor polymers selected are pBTTT (Poly(2,5–bis(3–tetradecyllthiophene–2– yl)thieno[3,2 - b]thiophene)), which is a relatively stable, liquid crystalline polymer which shows high hole mobility, and P3HT (Poly–[3– hexylthiophene]) which is a very well studied donor polymer system. The choice of n-GaN as the inorganic semiconducting material over other inorganic materials is based on three major advantages offered by n-GaN, 1) n-GaN provides a UV blocking and visible pass window, which is useful for exciting the polymer and also protects it from direct UV exposure, which can severely damage the polymer chains. 2) While absorbing in UV it can also give photocurrent, which can be useful for UV-Vis detectors based on n-GaN/Polymer hybrids 3) n-GaN has high electron mobility (~ 270 cm^2/Vs), which is expected to be helpful in fast response of the hybrid devices.

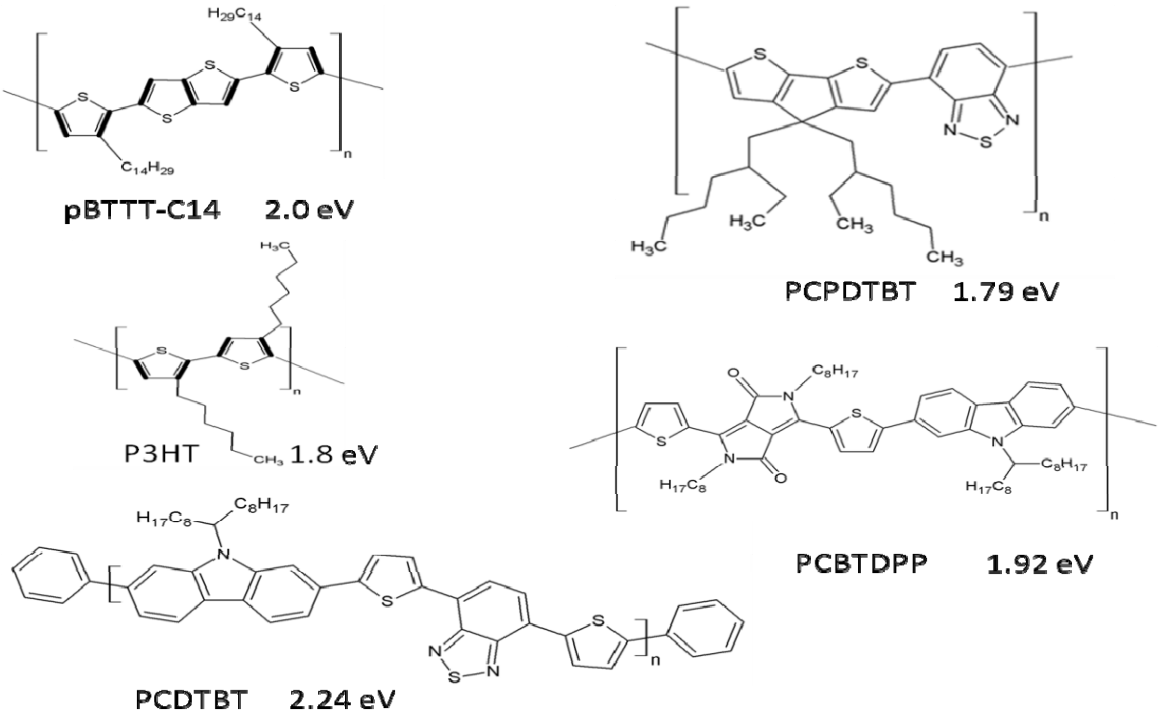

Figure 1.15 : Common donor type polymer semiconductors.

A systematic understanding of device architecture and measurement details has been presented in chapter 2. Basic problems faced while OI device fabrication and importance of various layer in improving the device efficiency has been shown. In chapter 3 photoluminescence (PL) emission from the n-GaN/pBTTT hybrid structure has been shown. PL emission at 632 nm is observed from the OI device which is not present for any of the pristine materials, the peak wavelength (632 nm) is higher in comparison to n-GaN PL peak (550 nm) but lower compared to pBTTT PL peak (720 nm), the actual origin of such PL shift is not understood, it is speculated that the emission is from interface states. Steady state measurements have been used to probe the device performance under direct current (DC) bias and small ac signal. The effect of interface states and bulk transport are reflected in the transport parameters calculated for n-GaN/polymer diode. An attempt has been made to calculate the barrier height and built in voltages. Intensity modulated photocurrent spectroscopy (IMPS) measurements show a characteristic peak in the modulated photocurrent response around 10 KHz. Additional features at lower frequencies and for n-GaN excitations have been observed, suggesting the involvement of other parameters in determining the response.

Followed by the steady state measurement, photoconductivity measurements have been performed; details are presented in chapter 4. It is seen that the energy level alignment is not just a function of workfunction offset but other interface parameters also play a significant role. The bulk transport through the organic thin film layer depends largely on the energetic band arrangement. Effect of energy levels, applied field, thickness and background illumination has been studied to probe the effect of various parameters on the transport of the charge carriers in the organic layer. A completely different response, from that expected, was observed for donor polymer semiconductors.

Theoretical models used for modeling the photocurrent response from the polymer semiconductors have been described in chapter 5. The models were developed originally for inorganic materials. The application of such models for organic semiconductor photocurrent action spectrum is subject to many approximations one has to make. Such approximations assumed during the modeling are also described. Further, an attempt has been made to extend the model for organic – inorganic hybrid materials. Possible modifications required to improve the model for better fitting to the experimental curves has been highlighted.

CHAPTER 2

MATERIALS AND METHODS

2.1 Introduction

Materials are the prerequisite for device fabrication. The choice of correct material is essential for framing appropriate questions and verifying models. Energy level matching, material purity, processability as thin film or electrode, stability in different testing condition are required for efficient devices. While working with semiconductors, the materials need to have less defect or impurity to avoid charge carriers trapping which decreases the average mobility of carriers. For high efficiency solar cell, single or polycrystalline materials with good match with solar spectrum and high absorption coefficients are best suited. A wide coverage of visible spectrum with higher absorption coefficients are available in organic semiconductors, but they are generally more disordered and have low carrier mobilities (~ 10^{-1} – 10^{-5} $cm^2/V.s$). Some of advantages of organic semiconductors are band gap tuning, solution processing of thin films, flexibility, and a wide class of materials available. These properties are hard to find in inorganic semiconductors, with have high carrier mobility (~ 10^{1} – 10^{3} $cm^2/V.s$) and thermal stability of inorganic materials. The synergy of the two components and processes in a hybrid device can open up a completely different set of optoelectronic properties.

In this chapter we will look at the material properties of organic and inorganic semiconducting materials used in studies of hybrid systems. Buffer layers and electrode materials and their requirements will be discussed in details. We will look into the device architecture and various steps related to device fabrication. In the last section we will discuss about the characterization techniques used for studies of charge transport and limiting factors in organic – inorganic (OI) hybrid heterostructure systems.

2.2 Semiconducting Polymers

Organic materials are the active component of OI devices, thus it is required to understand the basic material properties like optical band gap, carrier mobility, stacking natures and energy levels. Organic semiconductors can be small molecule or polymer semiconductor. Polymer semiconductors have larger conjugation length compared to small molecule, which gives better charge transport properties. For present study of OI diode the properties required from polymer semiconductors are, solution processability, less impurity concentration, absorption in visible and near IR wavelengths, and a type I and type II energy level alignment with Inorganic semiconducting material (n-GaN). The polymers used in this study satisfy above requirements to large extent. Here we will look at the material properties of pBTTT-C14, P3HT and N2200 polymers used in current study, Figure 2.1 shows the chemical structures of these polymers.

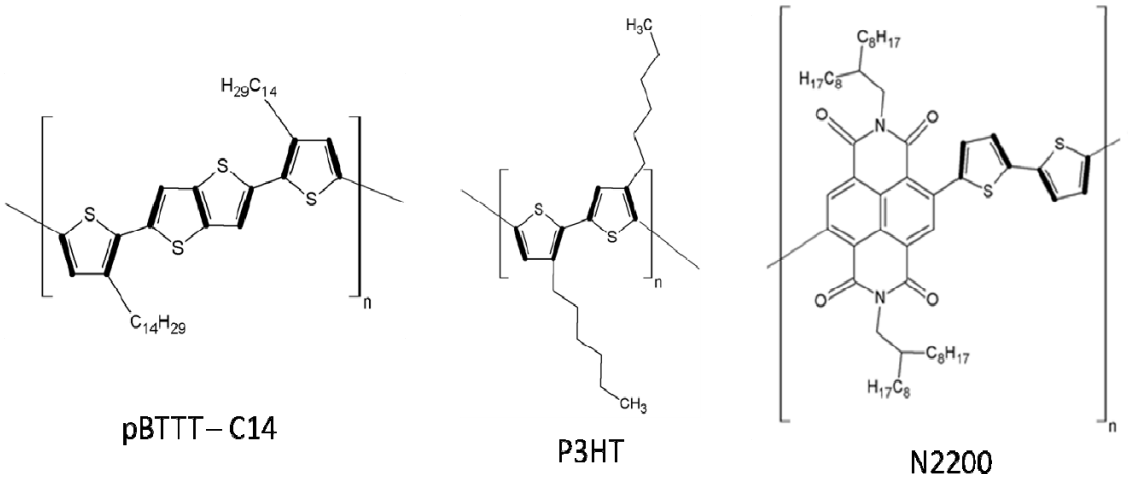

Figure 2.1 : Chemical structure of pBTTT-C14, P3HT and N2200 Polymers

2.2.1 pBTTT – C14

Poly(2,5–bis(3–tetradecyllthiophene–2– yl)thieno[3,2 - b]thiophene), commonly known as pBTTT. This is a p – type liquid crystalline semiconducting polymer with measured field effect hole mobility ~ 0.6 $cm^2/V.s$ [164], and thermally stable up to temperatures ~ 200 ^0C. The monomer is a thiophene based compound with optical band gap ~ 2.0 eV, and bulk hole mobility as measured through dark space charge limited current is ~ 3.8×10^{-4} $cm^2/V.s$ [165]. Degree of crystallinity depends largely on the molecular weight and conjugation length. pBTTT used in the studies of OI hybrid structure were of molecular weight ranging from 40 kDa to 80 kDa. The optical band gap as measured in UV–vis spectrometer (Perkin Elmer) is 1.94 eV, corresponding to an absorption edge of 640 nm. Peak absorption is at 520 nm and PL emission peak at 720 nm. Figure 2.2 shows the measured absorption and PL for pBTTT films (50nm) spin coated on quartz substrate. The absorption coefficient (α) has a maximum value of 1.5×10^5 cm^{-1} at 520 nm, as shown in Figure 2.3. The ionization potential measured from cyclic voltammeter (CV) is found to be at ~ -5.40 eV as shown in Figure 2.4. LUMO, as calculated from UV–vis data and ionization energy from cyclic voltammeter, is at ~ -3.46 eV. pBTTT-C14 is soluble in 1,2 – orthodichlorobenzene at an elevated temperature ~ 80 ^0C. The pBTTT-C14 used in present study where procured from luminescence corporation, Taiwan [166]

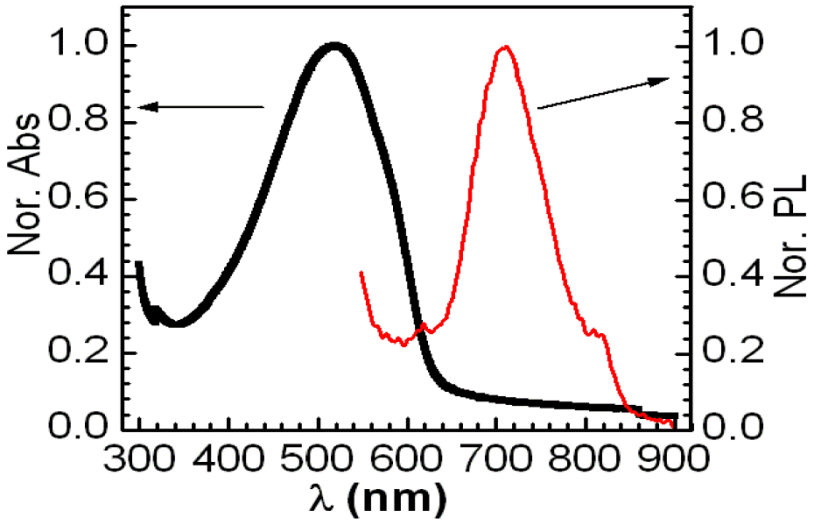

Figure 2.2 : Normalized absorption and PL emission for pBTTT. Absorption peak is at 520 nm and PL peak is at 720 nm.

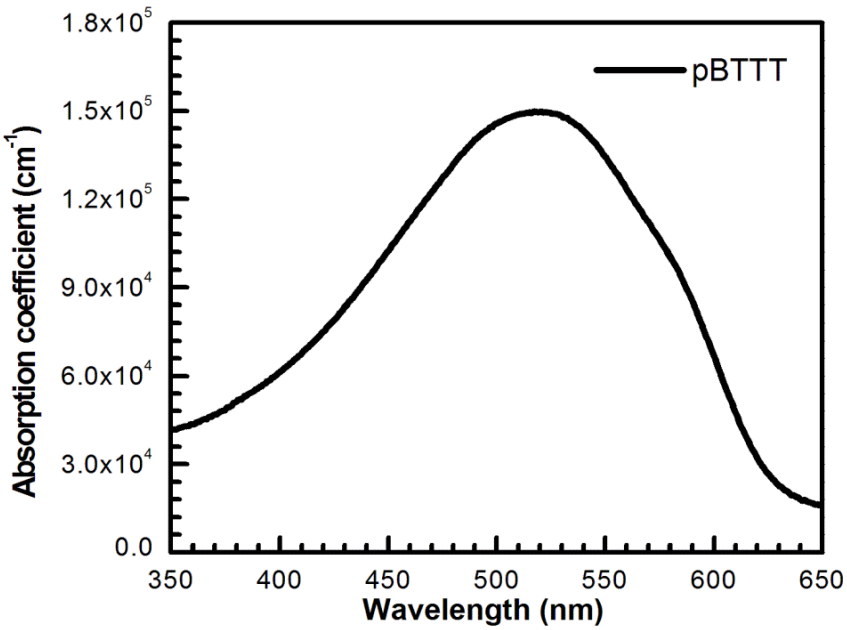

Figure 2.3 : Plot of absorption coefficient (α) of pBTTT as a function of wavelength (λ).

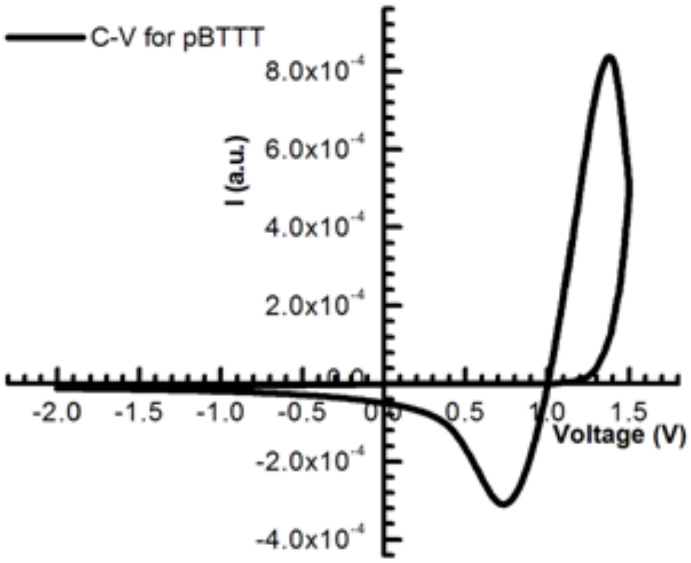

Figure 2.4 : Cyclic voltammeter plot for pBTTT.

2.2.2 P3HT

It is one of the most common semiconducting polymers in organic electronics. Poly–[3–hexylthiophene] (P3HT) is an alkyl substituted thiophene based compound with $T_g > 150\ ^0C$. The optical band gap is found to be ~ 1.9 eV [167]. Thiophene ring can be connected in head – head (HH), tail – tail (TT) and head – tail (HT) arrangement. P3HT can be classified in two categories, regioregular and regiorandom they vary in their electrical responses. P3HT films aggregate in a stacked interlock comb like structure [168]. P3HT used in current study has an optical band gap of 1.9 eV as measured from UV–vis spectroscopy; Figure 2.5 shows the absorption spectra and absorption coefficient α as a function of wavelength. The ionization energy (HOMO) measured through CV was -5.04 eV. The LUMO calculated using these data is -3.14 eV. P3HT films are known to show shows 3 types of stacking [169]. P3HT films coated on n-GaN shows a – type stacking with an inter chain spacing of 1.6 nm and 2θ value of 5.32^0. The a – type of stacking corresponds to thiophene rings parallel to each other and perpendicular to the substrate, the side chains are perpendicular to the substrate Figure 2.6 shows a schematics of a – type stacking in P3HT and corresponding XRD peak observed when coated on n-GaN films, it has been plotted after subtracting bare n-GaN XRD spectra. P3HT polymers used in this study were procured from luminscence incarporation, Taiwan [166]

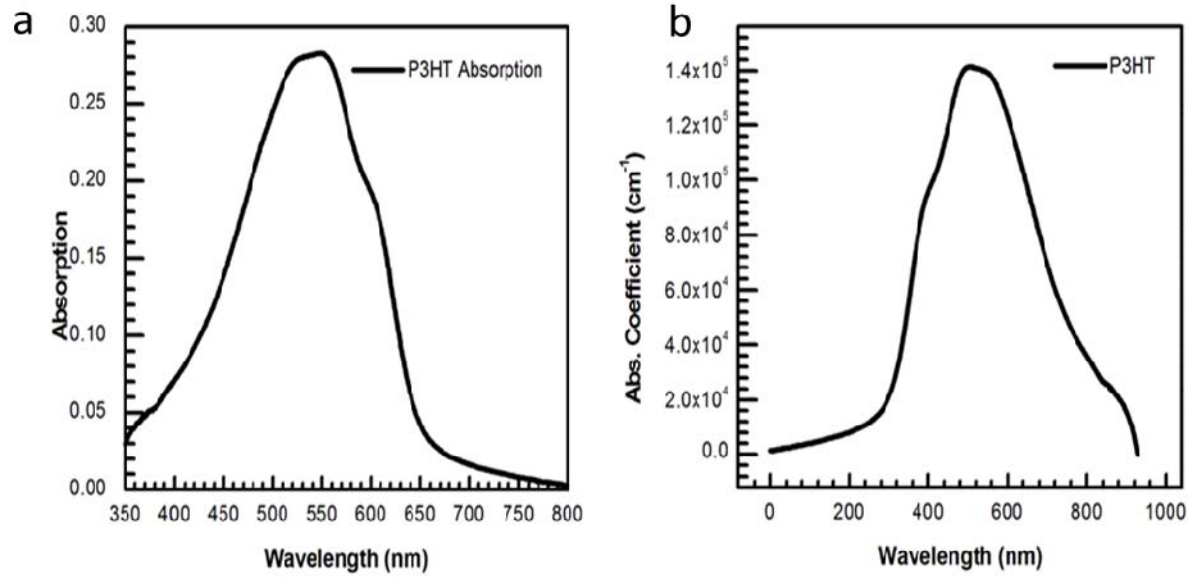

Figure 2.5 : a) Absorption spectra and b) absorption coefficient for P3HT films.

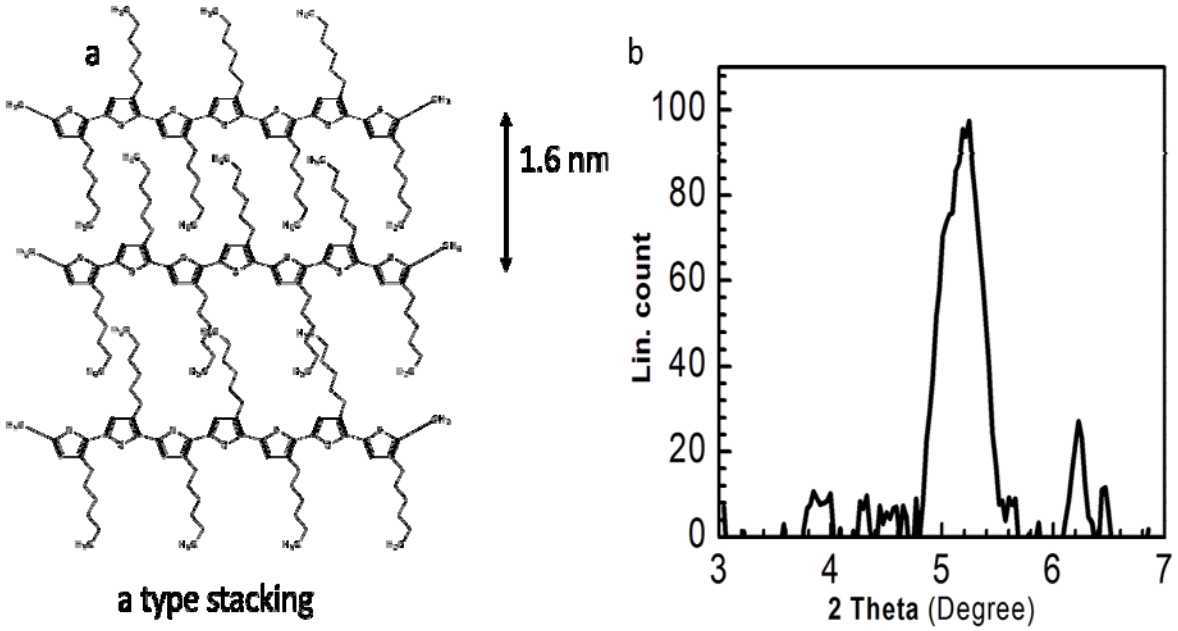

Figure 2.6 : a) Schematic representation of 'a' type stacking in P3HT films and b) corresponding XRD peak, ($2\theta = 5.23^0$)

2.2.3 N2200 (n type polymer)

Poly{[N,N' - bis(2-octyldodecyl)-napthalene-1,4,5,8-bis(dicarboximide)-2,6-diyl]-alt-5,5'-(2,2'-bithiophene)} (P(NDI20D-T2) , polyera ActiveInk N2200) is a napthalinediamide (NDI) based n-type polymer. High field effect mobility has been observed (~0.45 – 0.85 $cm^2/V.s$) [170] for this polymer. The NDI core provides electron depleted electronic structure which is a building block for polymer; it also provides a highly π – conjugated and regioregular backbone to the polymer. Optical band gap of N2200 is found to be ~1.45 eV [171], which is very less compared to naphthalene (~3 eV) or perylene-bis(dicarboximide) (~ 2 eV) [171]. Decrease in band gap confirms the presence of extended π – conjugation in the polymer. The LUMO of polymer is at -4.0 eV [170] and is stable up to temperatures ~ 300 ^0C [170]. The XRD scan shows no signature of crystallinity or stacking, large electron mobility with such amorphous nature of the film is quite unexpected. N2200 used in this study had a molecular weight of 125 kDa. Optical band gap as measured from UV–vis is 1.5 eV and corresponding HOMO and LUMO lies as -5.5 eV and -4.0 eV respectively. Peak in absorption is observed at 400 nm and 700 nm. Figure 2.7 shows the absorption as a function of wavelength. N2200 polymers used in present were studies were procured from Polyera [172].

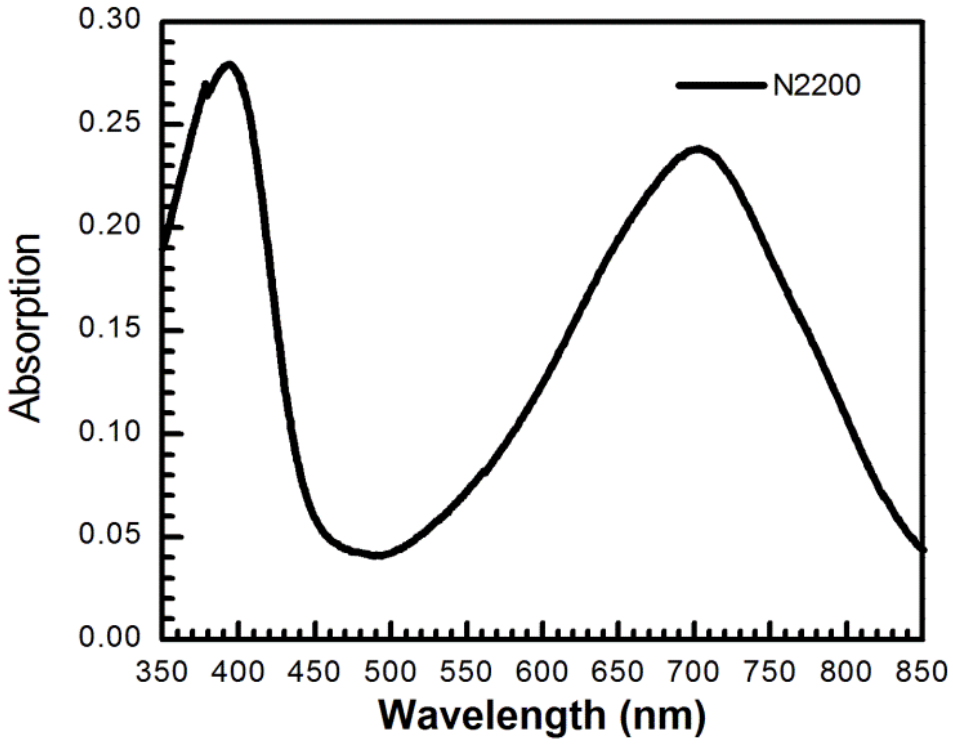

Figure 2.7 : Absorption spectra for N2200 polymer film (50nm).

2.3 Inorganic Semiconducting Material

Inorganic semiconductor is the active layer component in OI heterostructure. Inorganic semiconductors are generally pure, crystalline and exhibit high carrier mobility. The polarity or majority carrier concentration can be defined explicitly by external doping of donor or acceptor materials, giving rise to access of electron (n – type) or hole (p – type) respectively. Of the large family of elemental and compound inorganic semiconductors available, the nitride semiconductors (III-V family) have attracted special interest in terms of their properties and applications, especially in LED's. Epitaxial growth controlled doping, high carrier mobility and band gap tunability makes these semiconductors different from other families. In this study of the material properties desired from inorganic semiconductor part was wide band – gap corresponding to absorption in ultraviolet range, relatively high electron mobility. Material selected for this role was n doped gallium nitride which satisfies the requirements.

2.3.1 n-Doped Gallium Nitride

Among all the members of nitride family, gallium nitride (GaN) has been studied the most. The material and electronic property of GaN can be easily related to two basic property of nitrogen (N) atom (I) Size and (II) nature of chemical bond. It is the small size of nitrogen (covalent radius 0.7 Å) which results in significantly reduced lattice parameter and gives large bond energies 2.2 eV (GaN) [173] which implies high melting temperature. Relatively small size of N as compared to group III atoms plays important role in determining crystal structure. The thermodynamically stable structure of GaN and other nitrides (AlN and InN) is the hexagonal wurtzitic (WZ) structure. Though the high melting point gives better stability even at elevated temperatures, it poses problem for bulk growth, till date the preferred method of film growth is over foreign substrates. This heteroepitaxy causes defects and dislocations in the crystals, causing reduced performance. GaN films are grown heteroepitaxially on sapphire (lattice mismatch > 10%) [174] substrates which are easily available or on silicon carbide (SiC) (Lattice mismatch 3%) [175] substrates, which are much expensive compared to sapphire. Films grown via this method are generally n – type, without introducing any doping source [176, 177]. A large n-type background concentration (~ 10^{18} to 10^{19} cm^{-3}) makes p-type doping very unlikely. With the introduction of buffer layer the background concentration could be reduced below 10^{17} cm^{-3} and controlled further n – type doping could be performed using Si or Se atoms [177].

Material properties

"The two batches of n-GaN films grown on sapphire, used in current study, where grown at Albany, and were introduced to our group at JNC by Prof. Suchismita Guha, Department of Physics and Astronomy, University of Missouri, Columbia MO. These films were studied at JNC"

The quality of epitaxially grown film is terms of uniformity of film, background electron concentration, mobility of charge carrier and surface defect density depends largely on the growth parameters and methods. Thus it is required to look at the basic structural and electronic properties of n-GaN films used in current study. The table below summarizes the various measurable structural and electronic parameters and respective values for the n-GaN films used in current study.

Table 2.1 : material properties for n-GaN films grown on sapphire

n-GaN material parameter	Numerical values
Crystal Structure	Wurtzitic (WR)
Film thickness	~ 3 μm
Doping concentration	2.0×10^{18} cm^{-3}
Donor material	Si
Band Gap	3.4 eV
C.B. and V.B. maxima	-3.4 eV and -6.8 eV
Surface defect state density	~ 10^{9} cm^{-2}
Sheet resistivity	50 Ω cm
Electron mobility	~ 270 cm^2/V.s

The n-GaN films, used for present work are grown using MOCVD method at 1050 ^{0}C. The critical layer thickness of GaN is small and surface is relaxed as a large dislocation defect density (10^8 cm^{-2}) is present. Presence of huge amount of defect density is visible in the form of huge 550 nm broad PL emission from the films. Figure 2.8 shows absorption spectra and PL emission for excitation at 365 nm, the sinusoidal pattern in absorption curve can be because of the interference pattern formed by the light reflected from the two ends of n-GaN. The defect state PL emission has maxima at 550 nm and an optical width of 100 nm. A broad defect state emission is clearly visible at 550 nm. Figure 2.9 plots absorption coefficient (α) as a function of wavelength (λ).

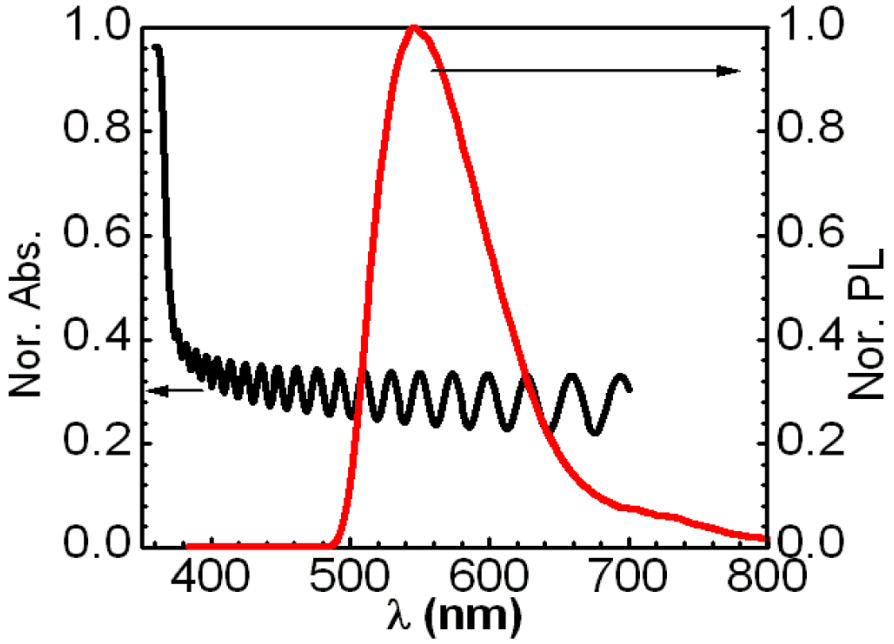

Figure 2.8 : Absorption and PL emission for n-GaN films grown through MOCVD.

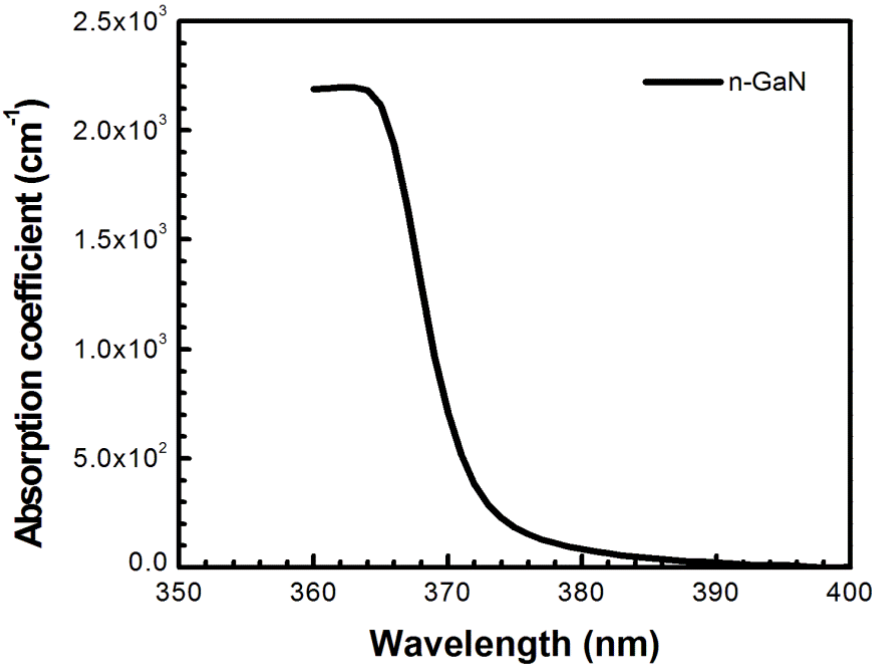

Figure 2.9 : Absorption coefficient for n-GaN films, as calculated for 3μm thick n-GaN films.

2.4 Buffer layers and metal electrodes

The role of buffer layer in improving film quality or device efficiency cannot be neglected. A few important roles that buffer layer plays when used in organic semiconducting devices are working as a gate, such that only one type of charges either electron (TiO_x , ZnO) [178, 179] or Hole (PEDOT:PSS, MoO_x) [180, 181], can pass through and the other type is blocked. This improves overall efficiency by reducing the recombination near electrode material. Another important role of buffer layer can be to avoid direct contact between polymer and metal electrode, which can cause degradation of organic layer by diffusion through [182,183] it or by damaging it during thermal evaporation of metal [184]. Another problem with top electrode deposition on polymer devices can be of shorting between top and bottom electrode. Buffer layer can help smoothing the abrupt change in energy levels [185]; buffer layers can provide hydrophobic (HMDS) [186] or hydrophilic ultra-thin (~ 5-10 nm) layers (MoO_x) for orthogonal film processing.

Electrodes are another important part of any semiconducting device. They provide a way for delivering photogenerated power to external circuit or a way to applying bias voltage to the device through external circuit. An ideal electrode should be highly conductive, chemically and electrochemically stable and should not cause the degradation of active material. For the present study, the choice of buffer layer and materials used for electrodes were an important part of the device fabrication as will be explained in later sections. In this section we will look at the problem related with the top electrode and how buffer layers are useful for efficient device fabrication.

2.4.1 Work Function requirements

Contact between two materials, either semiconductor-semiconductor or metal-semiconductor, is ohmic or rectifying depends on many factors like work function offset, surface states distribution etc. Contact of metal with semiconductor is ohmic or rectifying depends largely on the work function offset between the two sides. For a contact to be ohmic the work function of metal should have minimum offset with the chemical potential of semiconductor. While a higher offset result in larger barrier for charge transport across the interface, giving rise to rectifying I-V. The effect is not always too large but can be significant in particular cases. The same is true when using a buffer layer on top of semiconducting active layer. As shown in Figure

2.10 for n-type and p-type semiconductors, the mismatch between the work functions can cause formation of barrier for charge transport. Barrier height for n-type semiconductor – metal contact is given by

$$\phi_{ns} = \phi_m - \chi \tag{2.1}$$

In equation 2.1, E_m is the thermionic work function of the metal, and χ the electron affinity of the n-type semiconductor. Similarly for p-type semiconductor – metal contact the barrier height is given by,

$$\phi_{ps} = \chi + E_g - \phi_m \tag{2.2}$$

In equation 2.2, E_g is the band gap of the semiconductor. Thus it is clear that proper work function match is required for a charge transport free of injection barrier.

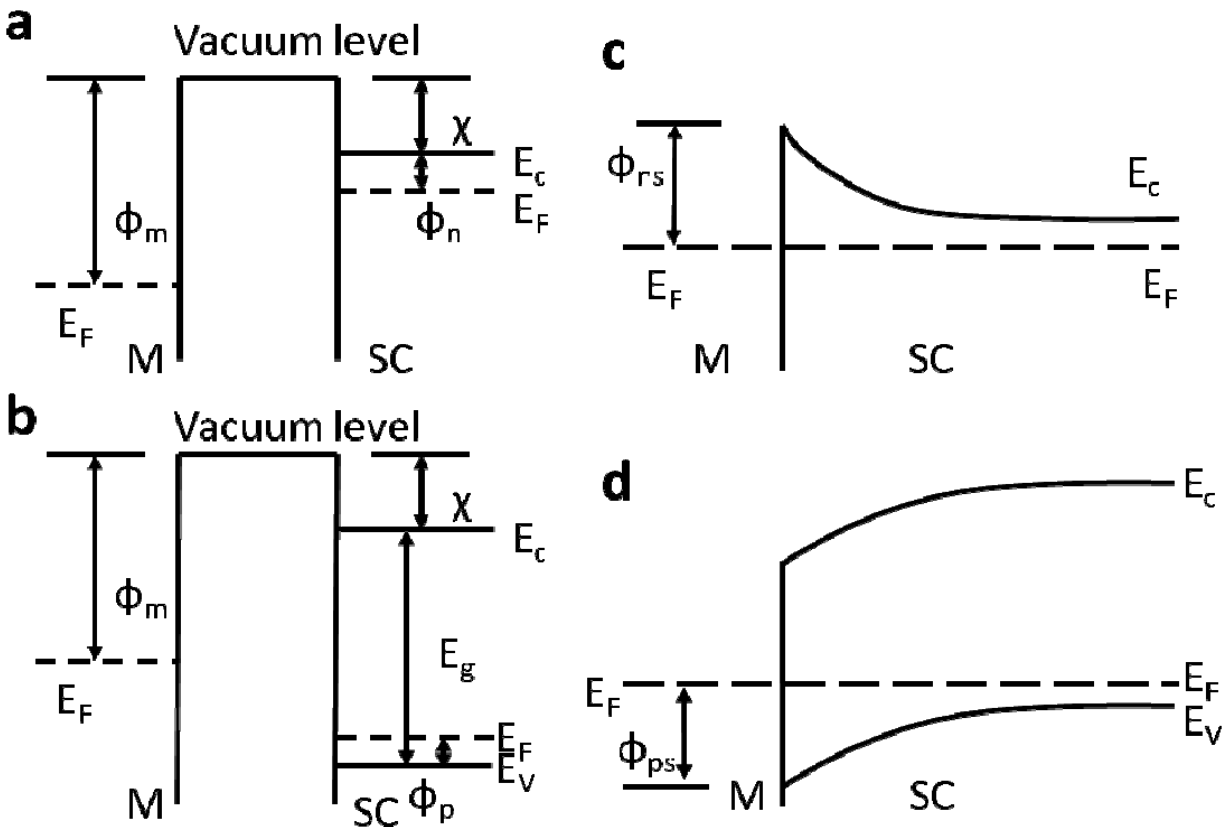

Figure 2.10 : Work function mismatch in non contact mode for a) n –type and b) p – type semiconductor. Barrier formed for c) n- type and d) p –type semiconductor.

A primary requirement, for studies of OI systems, is proper matching of workfunction of electrode with the electronic levels of semiconductors, such that an ohmic interface is formed. This implies a minimum injection barrier for charge transport between metals and semiconductor. The n-type material used in OI diode is n-GaN. An ohmic contact for electron transport requires, metal electrode with workfunction close to the Fermi level of n-GaN. Aluminum (workfunction -4.08 eV) [187] and indium (workfunction -4.12 eV) [188] are known to form ohmic contact with n –GaN [189,190]. Whereas the p-type materials used for OI diode are polymer semiconductor. The HOMO of p-type materials used lies below -5.0 eV (-5.04 eV for P3HT and -5.40 for pBTTT), these semiconductors are known to form ohmic contact with gold (Workfunction -5.1 eV) [191,192], ITO (workfunction – 4.7 eV) [193,194], PEDOT:PSS (HOMO -4.9 eV)[195,196]. I-V curves in Figure 2.11 and Figure 2.12 for In/n-GaN/In, ITO/PEDOT:PSS/pBTTT/PProDOT/Au and ITO/PEDOT:PSS/P3HT/PProDOT/AU shows the ohmic nature of contacts of polymers with respective metals and/or buffer layers. Thus the metal and buffer layer contacts with semiconductors do not pose any barrier for charge transport across the interface in the applied bias range.

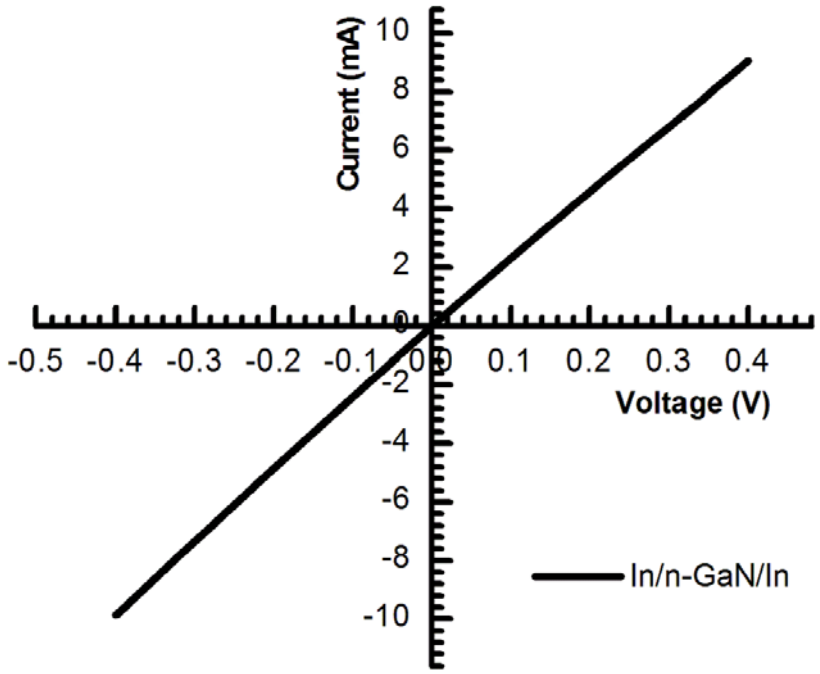

Figure 2.11 : I-V plot for In/n-GaN/In structure, showing ohmic nature for In/n-GaN contact placed.

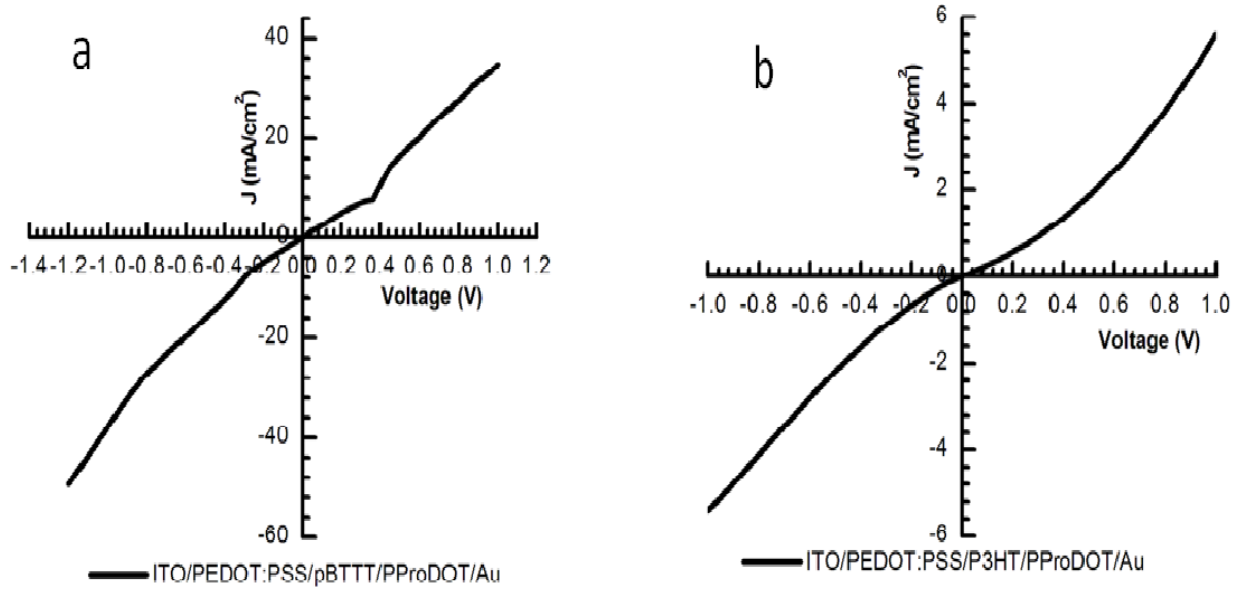

Figure 2.12 : I-V plots for a) pBTTT and b) P3HT, the I-V shows that the buffer layer (PProDOT) contact with pBTTT and P3HT is ohmic.

2.4.2 Problems with thermal deposition of top metal electrodes

When fabricating devices in sandwich structure, like diodes or capacitors, it is always required to deposit metal contacts on both ends of the semiconductor layer. Inorganic semiconductors also serve as substrates; metal electrode can be deposited easily on both ends without any problem as the wafers are thick (~ 2-3 μm) and stable at higher temperature, for example gallium nitride are stable up to 800-1000 ^{0}C [197]. Case for organic semiconductor materials is different, an efficient device made of organic semiconducting material requires a very thin layer of active material (80 – 200 nm) [198]. Deposition of top metal electrode (metal with higher work function) is not as straight forward as it was in inorganic semiconductors. Organic materials are soft and can get damaged easily with high energy particles which are evaporated during thermal deposition. During thermal evaporation the metals to be deposited are heated till they evaporate, these evaporated high energy metal atoms disseminate away from the source. When they collide with any surface they can transfer their energy to the surface atoms and can stick there depending upon their sticking coefficient. The polymer surface has weakly bounded polymer chains with van – der Waal attraction which can be easily damaged at higher energies. The damage caused by the high energy metal atoms is irreversible and cause defects or disorders at the metal – semiconductor interface, which give rise to interface trap states for

charge transport [199,200]. Effect of this impact can be reduced by decreasing the thermal energy of the polymer films i.e. by cooling the films to lower temperature prior to deposition, or decreasing the thermal energy of metal atoms by increasing the effective distance between sources and substrates. The non-uniformity is less for aluminum compared to gold [201]. There can be still other effects, like penetration or diffusion of metal atoms deep inside the organic materials, forming percolation path for metal atoms [202]. This effect decreases the shunt resistance between top and bottom contacts, which causes the current to pass through the metal channel without passing through the semiconducting layer. Few reasons that can cause shorting between the two metal electrodes are summarized below,

- High energy metal atoms: It can easily diffuse into the polymer. The problem of diffusion is more pronounced in thin film (~ 60 – 100 nm) devices where film thickness is not sufficient to stop diffusion.
- Bad thin film quality: presence of particles or pin holes, formed during spin coating, can provide and easy route for top electrode metals diffusion to bottom electrode.

In order to avoid shorting, better quality films with less particle and pin holes or cracks would be effective. This can be achieved by selecting solvents with better solubility of polymer, stirring at elevated temperature (70 – 80 ^{0}C) or filtering the polymer solution using fine pore size filters (example 0.2 μm). Molecular weight of the polymer also plays an important role in avoiding shorting, as higher molecular weight polymers will give thicker and denser films which can stop diffusion of metal atoms at shallow depths inside the polymer [203]. Along with these techniques, introduction of a very thin (~ 10 – 30 nm) layer of buffer material between polymer and metal electrode can also solve the problem. This can avoid shorting of electrodes through polymer or damage of polymer surface with hot atoms. Buffer layers can be deposited either by solution based methods [204,205] or via slow thermal deposition [206,207]. A wide variety of p – and n – type buffer layer materials are available, for example, the p – type buffer layer materials are PEDOT:PSS, MoO_x, PProDOT, etc. The n – type buffer layer materials are TiO_x, ZnO, LiF etc. A detailed description of buffer layers and their benefits in improving device efficiency will be presented in next section.

2.4.3 Advantage of Buffer layer

Buffer layers are known to play important role in organic and polymer semiconductor devices [208]. They have been employed to control the injection conditions, converting contacts which were blocking into ohmic [209]. Hole conducting buffer layers like PEDOT:PSS and its derivatives are known to influence short circuit current density, open circuit voltage, fill factor and rectification in case of solar cells. Along with the role of better charge injection and collection they can also help in stabilizing the active layer by reducing oxygen diffusion. Oxide buffer layers like ZnO, MoO_x, TiO_x are known to stop oxygen diffusion into the active layer, giving stability to the device [210,211,212]. A second most important role can be to provide a blocking layer for metal atoms diffusion into the polymer bulk, where a direct contact between polymer and metal atom can cause degradation of active material. For the study of OI hybrid heterostructure poly(3,4-propylenedioxythiophene) (PProDOT) was used as a hole transporting buffer layer between polymer active layer and top gold electrode. Introduction of this buffer layer helped in removing any shorting between top gold electrode and n-GaN. Figure 2.13 shows the difference in current – voltage characteristics with and without PProDOT. The rectification in the I-V without the PProDOT layer can be because of the fact that gold also forms a rectifying barrier with n-GaN.

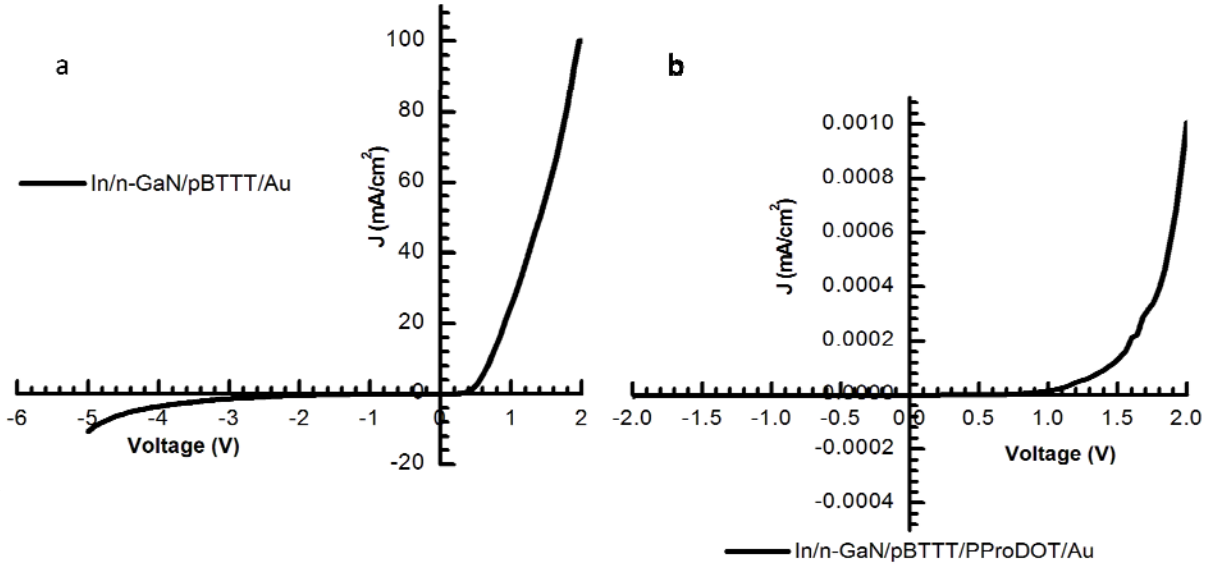

Figure 2.13 : I-V plots for n-GaN/pBTTT OI diode a) without PProDOT buffer layer and b) with PProDOT buffer layer.

2.4.4 Why not PEDOT:PSS ? Use of PProDOT

poly(3,4-ethylenedioxythiophene):Poly (styrene sulfonic acid) (PEDOT:PSS) is a very well studied hole conducting water based polymer. Use of PEDOT:PSS buffer layer in OPV's has been well established. The major role of PEDOT:PSS film in organic electronics devices is to selectively transport only holes and leave electrons out. Doping of PEDOT is carried out while polymerization of EDOT by the use of water based poly (styrene sulfonic acid) [213]. PSS is a water soluble polymer which makes PEDOT:PSS a water based dispersion [213], Figure 2.14 shows the chemical structure for PEDOT:PSS. For coating PEDOT: PSS layer on any surface, the surface should be hydrophilic in nature (contact angle << 90^0). As will be seen in next section the device architecture is such that the hole transporting layer needs to be coated on top of polymer. This requires an orthogonal solvent based polymer solution which can be coated on the hydrophobic surface of polymer. Water based PEDOT: PSS dispersion is orthogonal to polymer but cannot be coated on a hydrophobic surface because of the above mentioned reasons. For coating the hole conducting polymer layer on top of pBTTT and P3HT, a solvent system is required which is does not dissolves the active polymer layer (orthogonal) and is hydrophobic (surface wetting) in nature.

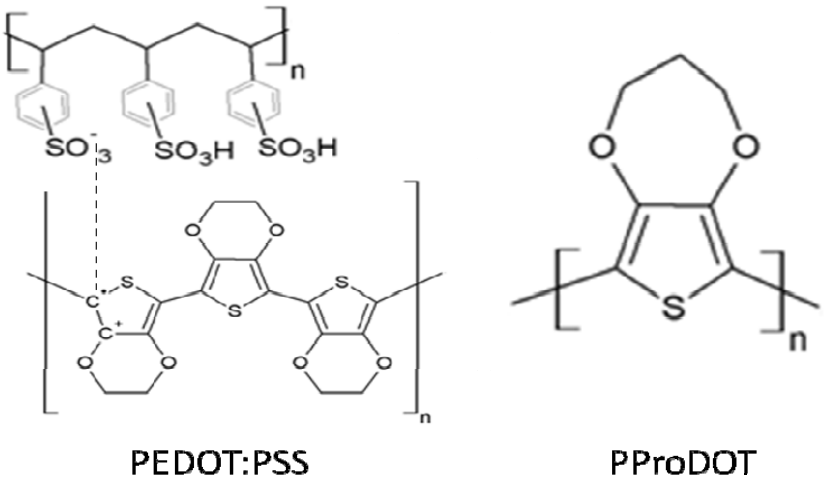

Figure 2.14 : Chemical structure for PEDOT:PSS and PProDOT.

"The PProDOT used in present work was obtained from Prof. Anil Kumar, IIT (B)" PProDOT is a thiophene based hole conducting polymer, which is doped with bromine, chemical structure shown in Figure 2.14. This polymer can easily be dissolved in many chlorine based

organic solvents like chloroform ($CHCl_3$), trichloroethylene (TCE), and dichloromethane (DCM). These solvents are suitable for coating on hydrophobic surface and also orthogonal to pBTTT (Chloroform, TCE) and P3HT (DCM). A very thin layer of ~ 10 – 20 nm PProDOT when spin coated on top of polymer active layer, can protect the active polymer layer from getting damaged.

2.5 Device Architecture and Fabrication

Till now we discussed about the active semiconducting layer materials, buffer layer materials and their importance and metal electrodes. In this section we will try to put them together in the form of OI hybrid heterostructure diode. We will look at the device architecture and significance of each layer, along with the fabrication details. The n-GaN which is also the n-type region for OI diode, works as a substrate for device fabrication. The n-GaN films are of 3 μm thickness and are grown over c-plane sapphire. The transmission of these sapphire substrates is on an average 8% as shown in Figure 2.15. To increase transmission sapphire substrates were polished using 9 μm polishing cloth, which increased the transmission by 8 times as shown in figure 2.15. These polished substrates were used for further device fabrication.

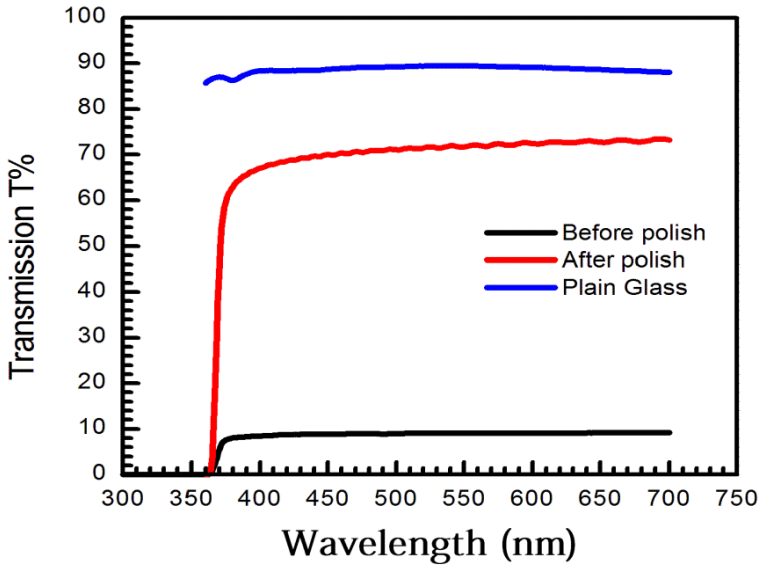

Figure 2.15 : Transmission spectrum form n-GaN before (black) and after (red) polishing. Glass transmission (blue) has been shown for reference.

The OI hybrid heterostructure device is a bilayer diode where n-GaN acts an n – type region and polymers (pBTTT, P3HT) act as p – type region. Indium (In) contact is placed on the same side as the polymer film, which gives rise to a diffusive transport in GaN layer. Gold (Au) is used as a hole collecting top electrode with PProDOT as the hole transporting buffer layer between metal electrode and polymer active layer. To isolate top contact region from n-GaN while taking contact, an epoxy bridge was used below the contact. Figure 2.16 gives the schematics of device structure.

Figure 2.16 : A schematic structure for n-GaN/pBTTT OI hybrid heterostructure device. The pBTTT layer is replaced by other polymers.

The first step of fabrication is to clean n-GaN substrate for removing any impurity or passivation layer. For cleaning the substrates, back polished n-GaN substrates were sonicated in 1:1:1 (volume ratio) solution of isopropyl alcohol (IPA), acetone, and chloroform for 10 min. Substrates were boiled for 3 min in TCE and IPA separately, followed by rinsing in deionized water and blow drying. After organic cleaning the insulating epoxy layer was spin coated on the patterned region, followed by curing at elevated temperature. Indium contacts were placed on n-GaN wafer using high temperature doctor's blade technique. In contact and epoxy layer was masked and the active region of n-GaN was plasma cleaned for 6 min, followed by immediate coating of polymer active layer. Polymer coating and further processing were carried out inside the N_2 atmosphere glove box (H_2O < 1 ppm; O_2 < 10 ppm). Polymer solutions were prepared in 1,2-orthodichlorobenzene, stirred at 70 – 80 ^{0}C for 6 - 8 hours. Polymer active layer thickness was ~ 100 -120 nm. Polymer active layers were annealed at 170 ^{0}C for pBTTT and 120 ^{0}C for P3HT and N2200. P3HT and pBTTT Polymers are known to form crystalline phase when annealed at elevated temperature [214,215]. The hole transporting PProDOT layer was coated from TCE (pBTTT) solution and DCM (P3HT) solution followed by annealing at 110 ^{0}C for 2 min. N2200 devices were fabricated using similar procedures, n-type polymer N2200 does not

conduct holes, thus no hole transport layer coating was required. Top metal electrode, Au (pBTTT and P3HT) and Al (N2200) was deposited on the masked samples at a pressure of 10^{-6} mbar. The evaporation rate was slow (~ 5Å per min) for first 10 nm of metal deposition. Two different top electrodes thicknesses were deposited one of 100 – 150 nm thick and second 10-15 nm thin metal electrode.

Generally light illumination was carried out from n-GaN side of the OI structure. For top illumination measurements thin electrodes of thickness 10-15 nm was used. These thin electrodes gave 70 - 75 % transmission for wavelengths in visible spectrum. In the following section we will discuss about the charge transport characterization techniques for OI hybrid heterostructure diodes used in this work.

2.6 Charge Transport Characterization Technique

This chapter discusses charge transport characterization method, which is the method to determine the response of OI devices to various electrical and optical parameters. It is the final part of the experiment. However a device is characterized as a whole, thus the interpretation of measured signals or data is complex. A lot of processes may give rise to a very simple and relatively feature less result, like current – voltage characteristics. Thus the challenge of characterizing any device lies not only in measurement of the samples but mostly in data interpretation, which depends mostly on device simulation.

A variety of characterization techniques can be employed. The current of OI diode can be measured as a function of applied bias, illumination intensity, wavelength of monochromatic illumination, diode temperature, position of illumination, frequency of illuminating light. The impedance of OI diode can be measured as a function of applied alternating voltage or frequency. In this section we will discuss all those techniques which were used for studies of charge transport and affecting factors, their practical implementation and device modeling to a certain extent. The techniques which will be discussed have been listed below,

1) Current – Voltage characterization
2) Spectral photocurrent response
3) Capacitance – Voltage and Capacitance – Frequency measurement
4) Intensity Modulated Photocurrent Spectroscopy

2.6.1 Current – Voltage (I-V) curves

Dark current-voltage curves are drawn by measuring current from the device as a function of applied dc bias voltage. Current is measured using an electrometer and voltage is applied using a voltage source like voltmeter. A simple diagram for I-V measurement setup has been shown is

Figure 2.17. The I-V curve for a p-n junction diode looks rectifying in nature, the resistance is less when diode is forward biased (positive voltage applied to gold) and corresponding current is high (~ μA to mA) through the device. When in reverse biased state (positive voltage is applied to Indium) the device resistance is high and current magnitude is low (~ nA to pA). Rectification ratio in OI HJ junction diode lies in the range of $10^3 – 10^5$. Forward I-V curves for OI hybrid diodes can be modeled using thermionic emission and space charge injection limited current, as mentioned in chapter 1. The basic information which can be extracted from the forward dark I-V curve is barrier height (ϕ_b), and diode ideality factor (n). While the reverse I-V can tell about the magnitude of saturation current and breakdown voltage, which are useful when operating diode in photoconductive mode.

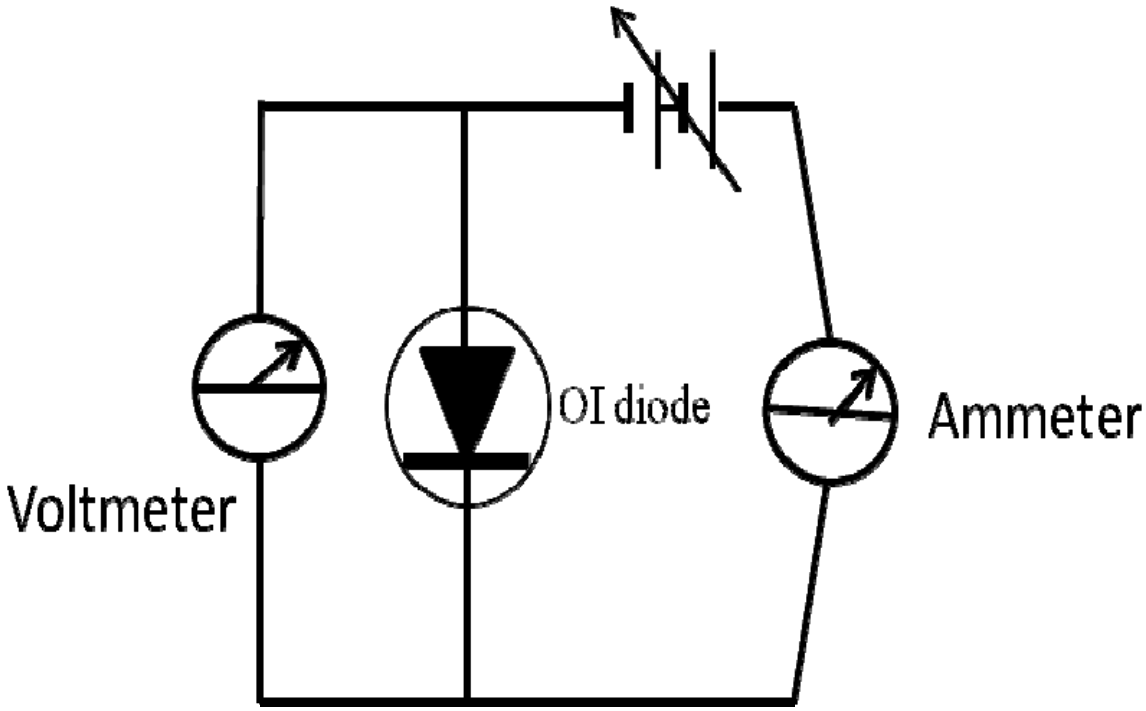

Figure 2.17 : Schematic diagram for I-V measurement of OI hybrid heterostructure device.

The voltage and current measurements are performed during the voltage sweep with a four point probe technique, that is, the current measurement is connected in series with the load resistance, while the voltage measurement requires two separate probes. The circuit containing the voltage measurement has a high resistance which avoids any resistive voltage drop which can affect the measurement.

I-V performed under light illumination can add additional information to dark I-V characteristics. The same I-V measurement setup can be used with a light source for illumination. The light I-V differs from the dark in the sense that apart from charge carriers injected in the device through the electrode, using an external source, there is also a constant source of charge present inside the device. These are photogenerated charges, which are generated inside the devices under constant photo illumination. When a diode is placed under light and charge carriers are generated as a result of illumination, the diode functions as solar cell. Even though the power conversion efficiency is not important, the Voc and Jsc can give an idea about extent of generation and recombination effects playing role in the diode. When studying from detector point of view, the information which is of importance is reverse saturation current, photocurrent at short circuit and percentage enhancement under reverse biased condition.

2.6.2 Spectral Photocurrent response

The current voltage measurement alone cannot give information about the origin of loss mechanisms that are responsible for the fact that not every photon incident contributes to photocurrent. An appropriate method to look at the reason for losses is spectrally resolved measurements of short circuit current, which is $J_{sc}(E)$ or $J_{sc}(\lambda)$. Measurement under different bias (positive and negative with respect to anode) gives an insight into the transport mechanisms in the bulk, which apart from being morphology dependent, also depends largely on the field conditions present inside the bulk of semiconductor. When looking from a detector point of view, the measure of responsivity is important to determine the wavelength span of detector. A wide spectral band coverage and higher responsivity are the essential prerequisites for a good photodetector. The responsivity of a photodetector is defined as,

$$SR(E) = \frac{dJ(E)}{d\emptyset(E)}\frac{1}{E} = \frac{qQ_e}{E} \; or \; \frac{dJ(E)}{dP(E)} \tag{2.3}$$

In equation 2.3, SR (spectral responsivity) is expressed in units of A/W (Ampere per watt), E is the energy of incident photon of monochromatic wavelength λ_E, J(E) is the photocurrent density as a function of E, Q_e is the quantum efficiency, ϕ(E) is the incident photon flux as a function of E and P(E) is the input power as a function of E.

To measure the responsivity of OI hybrid diode, a monochromator based setup is used. The advantage of monochromator based setup is high wavelength resolution and broad spectral range coverage. The area of illumination for a monochromator based setup is only a few mm. In the setup first white light from a Xe – arc lamp (OREL) is fed into monochromator (SPEX 500). The light from monochromator is focused and chopped using optical chopper. Reference of the optical chopper is fed to lock – in amplifier. The focused light is further split in two components using a 30R/70T beam splitter. The 30% reflected light is focused on the reference solar cell and 70% transmitted light is focused on the device (OI diode in this case). The setup is calibrated using a photodetector in place of device. The reference used of calibration can be a pyroelectric radiometer combined with a solar cell, for relative calibration or a photodetector for absolute calibration at a particular wavelength. Using a reference cell is useful as long as the reference cell has high quantum efficiency for all wavelengths of interest for the devices under test. Current signal from reference solar cell and device are converted into voltage by a current – to – voltage converter with a typical amplification ratio of 10^4 – 10^6 V/A. Voltage output from the converter serves as the input for the lock in amplifier (SRS 830), which uses the synchronized output of chopper control as reference frequency. The amplified signal of lock in amplifier is then recorded using computer.

The area of illumination of device and reference cell is kept constant to take care of area normalization. For bias dependant study, an external dc bias voltage source (Keithley 2400 source meter) is connected in series with the device. The scan interval and integration time of lock in are set such that response measured at each wavelength is generated by that particular wavelength illumination and no previous wavelength illumination effect is carried over. For background light dependent measurement, a white LED of 1W optical power was used. The optical power calibration was carried out using silicon reference cell with no distance between

LED and reference cell. Identical condition of distance was maintained during measurement of device response. The schematics of setup used for photocurrent measurement is shown in Figure 2.18; the voltage and light bias are active only when it is required.

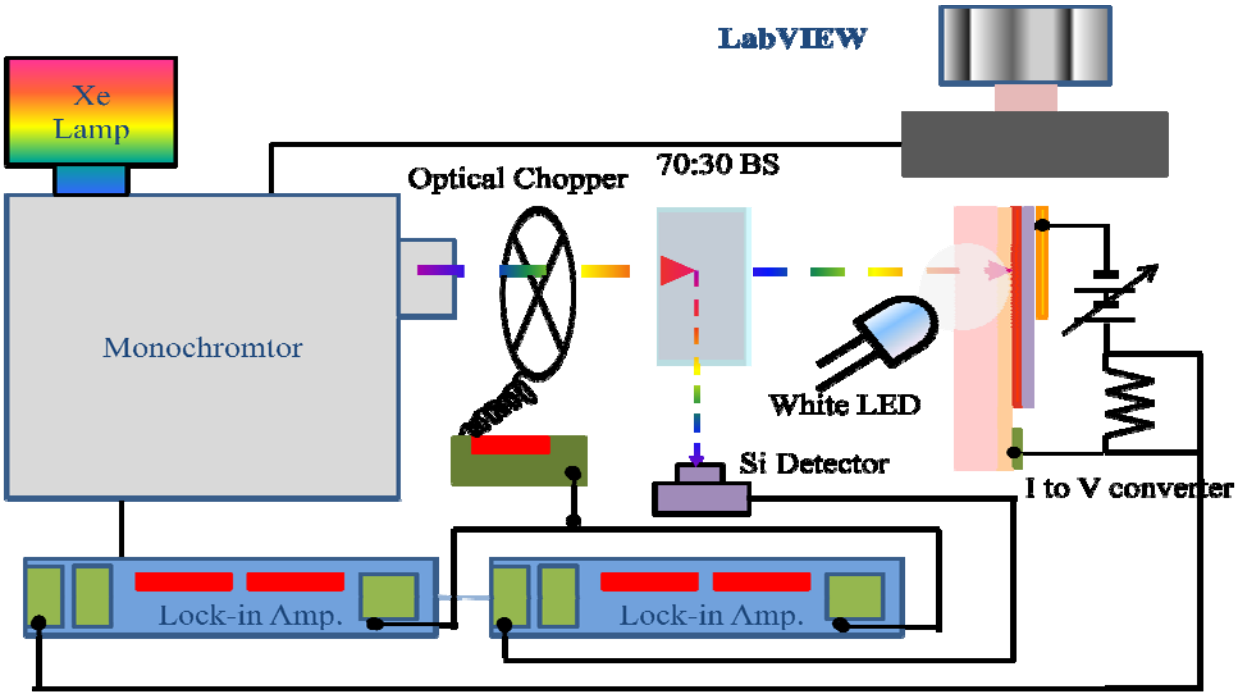

Figure 2.18 : Schematic diagram for spectral photocurrent measurement. The bias source and/or LED are active only when they are required for the measurement.

Information about the charge transport in OI diode requires modeling of device using generation and recombination terms along with drift and diffusion components of current. Bias dependent measurement gives information about field dependent transport in organic bulk layer. Background illumination dependent measurement gives insight into the transport where recombination effects are playing bigger role.

2.6.3 Capacitance Spectroscopy

Capacitance or, more generally, admittance measurements, are useful for probing bulk and interface properties of a buried layer in a working diode like structure. The small signal capacitance is by definition sensitive to carrier capture and emission from trap states, seen from the charge response δQ to a small voltage change δV, $c = \delta Q/\delta V$. A number of experimental techniques have been developed to make use of this sensitivity to map defect state density.

Capacitance – voltage (CV) profiling and admittance spectroscopy (AS). We will look at these techniques from the introductory concepts.

A small sinusoidal voltage v_a is taken to be superimposed on the applied bias giving rise to an a.c. current (i) flowing through the diode. For a passive device like diode, the a.c. response is specified by a small signal admittance, $Y = i/v_a$. The junction region response of a diode has capacitive and conductive components and in general exhibits an admittance of the form

$$Y = G + j\omega C \tag{2.4}$$

In equation 2.4, $j^2 = -1$ and ω is the angular frequency of a.c. signal. In reverse bias condition, the p-n junction diode becomes functionally equivalent to a capacitor; the only difference is that diode capacitance monotonically decreases with increasing reverse bias. The overall effect of an a.c. signal can be viewed as a small signal oscillation of the depletion width about its steady state value and associated charge density $\Delta\rho$ oscillation. This a.c. situation is identical to what takes place inside a parallel plate capacitor. In the same analogy the diode capacitance can be concluded to be,

$$C_j = \frac{\varepsilon_0 K_s A}{W} \tag{2.5}$$

In equation 2.5, C_j is junction or depletion layer capacitance, W is the depletion width, A is the area of diode and K_s is the dielectric constant of semiconducting material. To achieve oscillation, the carriers are assumed to move rapidly in synchronization with the a.c. signal. Under such condition the device is said to follow the a.c. signal quasistatically.

2.6.3.1 Capacitance – Voltage Technique

To obtain the precise capacitance versus voltage relationship as expected from diode, the W in equation 2.5 must be replaced by the appropriate expression relating W with applied voltage. W versus V_A relationship was found to vary with doping profile. For two very familiar doping profiles, the W versus V_A relationship has been given as [6]

$$W = \left[\frac{2K_s\varepsilon_0}{qN_B}(V_{bi} - V_A)\right]^{1/2} \quad \ldots asymmetrical\ step\ junction \tag{2.6}$$

For linearly graded junction the relationship is given by,

$$W = \left[\frac{12K_s\varepsilon_0}{qa}(V_{bi} - V_A)\right]^{1/3} \quad \ldots linearly\ graded\ junction \qquad (2.7)$$

In equation 2.7, 'a' is linear grading constant for linearly graded junction. A single generalized relationship can also be developed for W versus V_A. Considering the lightly doped side described by the power law,

$$N_B(x) = bx^m \quad , x > 0 \qquad (2.8)$$

In equation 2.8, b is greater than zero and m is a constant for a given profile. m = 0 and m = 1 corresponds to asymmetrical step junction and one sided linearly graded junction, for m > 2, [6]

$$W = \left[\frac{(m+2)K_S\varepsilon_0}{qb}(V_{bi} - V_A)\right]^{1/(m+2)} \qquad (2.9)$$

The junction capacitance is be given by,

$$C_j = \frac{K_s\varepsilon_0 A}{\left[\frac{(m+2)K_s\varepsilon_0}{qb}(V_{bi} - V_A)\right]^{1/(m+2)}} \qquad (2.10)$$

Using C_{j0}, given by,

$$C_{j0} \equiv C_j/_{V_A=0} = \frac{K_s\varepsilon_0 A}{\left[\frac{(m+2)K_s\varepsilon_0}{qb}\right]^{1/(m+2)}} \qquad (2.11)$$

The junction capacitance can be written as,

$$C_j = \frac{C_{j0}}{\left(1 - \frac{V_A}{V_{bi}}\right)^{1/(m+2)}} \qquad (2.12)$$

In general, any diode like device can be studied using the technique described here; the diode quality must allow the capacitive response from the space charge region to be clearly distinguished. To measure admittance, a small signal a.c. current response is measured as a function of applied a.c. voltage. The signal consists of two parts, the amplitude and phase; the current can be decomposed into a component in phase and another out of phase by 90^0. This

measurement can be performed using an LCR meter or a parameter analyzer (Keithley 4200 SCS). Figure 2.19 shows a schematic of admittance measurement setup.

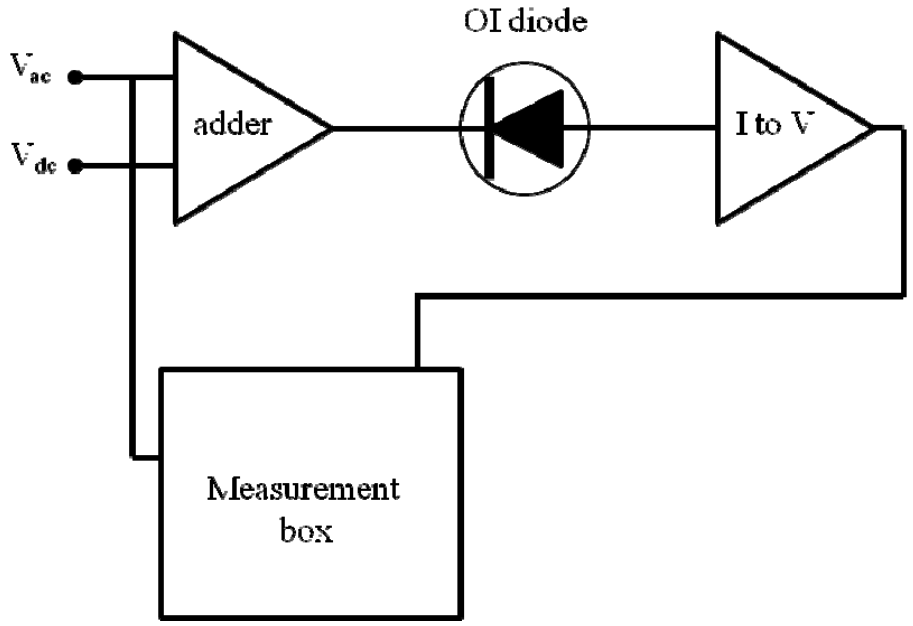

Figure 2.19 : Schematic diagram for Capacitance – Voltage and Capacitance – Frequency measurement [216]

A small a.c. voltage (~ 30 mv) is applied over a dc bias voltage at a probing signal of 100 KHz. The current is measured and corresponding admittance Y is calculated which is in complex plane. A careful calibration is required at each measurement frequency especially at frequencies above 1 MHz, care must be taken for circuit components, connections and calibration [217]. Also C-V data from a p-n junction can be used to determine device properties and interface states density in the OI heterostructure diode system. Plotting $1/C_j^2$ versus V_A, one should get a straight line for symmetrical step junction with a slope inversely proportional to N_B. Extrapolating $1/C_j^2$ = 0 intercept gives $V_{bi.}$

$$\frac{1}{C_j^2} = \frac{2}{qN_B K_s \varepsilon_0 A^2}(V_{bi} - V_A) \qquad (2.13)$$

If the diode area is known, N_B can be deduced from the slope of the plot. The doping variation with position $N_B(x)$ on the highly doped side of a junction can be derived directly from the C-V data.

$$N_B(x) = \frac{2}{qK_S\varepsilon_0 A^2 \left[d\left(\frac{1}{C_j^2}\right) \Big/ dV_A \right]} \quad , where\ x = \frac{K_S\varepsilon_0 A}{C_j} \tag{2.14}$$

The position x, is the distance of depletion layer into the lightly doped side of the diode as measured from the metallurgical junction.

2.6.3.2 Capacitance – Frequency measurement

Also known as admittance spectroscopy is measurement of sample admittance as a function of applied small signal a.c. frequency. This technique can yield the thickness of the film, the position of the Fermi energy in the bulk, the energetic position of dominant defect bands that occur between the Fermi energy and mid gap, and an estimate of the density of trap states. In admittance spectroscopy the applied frequency is ramped so as to cross the transition frequency above which the trap just start to respond. This method can detect traps between the band edge and mid gap [218]. At higher frequency, the carrier in the bulk do not move that fast, in and out of the depletion edge in response to the applied voltage, which causes a condition called freeze – out. Capacitance response in these case will be of bulk dielectric $c = K_s\varepsilon_0 A/\mathcal{T}$, where $\mathcal{T}$ is the distance between top and back contact. With increase in temperature or decrease of applied signal frequency the capacitance changes from bulk to junction $c = K_s\varepsilon_0 A/W$. As temperature increases or frequency decreases, the trap state can begin to respond. The demarcation energy E_d determines the cutoff energy for trap response at a given temperature and frequency.

A step in capacitance corresponds to a peak in G/ω, where G is the conductance. This peak arises because of their relation, which can be calculated using the Kramers – Kronig transformations, which relate the real and imaginary part of the susceptibility, $\epsilon'$and ϵ'', respectively [219,220]. While G/ω peak can be a good way to observe the position of the

capacitance step, the step can be hidden because of the leakage conductance in some samples. An analogous peak can be obtained from the derivative.

$$\frac{dC}{dE_d} = -\frac{\omega}{kT}\frac{dC}{d\omega} \tag{2.15}$$

An Arrhenius plot of $ln\left(\omega/T^2\right)$ as a function of 1000/T can give activation energy E_{na} and capture cross section σ_{na} for trap states.

2.6.4 Intensity Modulated Photocurrent Spectroscopy (IMPS)

This method involves sinusoidal modulation of the illumination intensity, it has been used extensively to investigate variety to understand the microscopic processes in amorphous Si solar cells and dye sensitized solar cells [221,222, 223,224]. The light source can be a Light Emitting Diode (LED) or a modulated laser beam. LED's are available with emission wavelengths ranging from blue to near IR, their output can be modulated by controlling the current. For linear analysis of response, the modulation can be a small fraction of total intensity. Alternatively a second light source can be used provide the dc component of the illumination.

The illumination intensity consists of a dc and an ac component [225]

$$I(t) = I_{dc} + I_{ac}\sin(\omega t) \quad , where\ \omega = 2\pi f \tag{2.16}$$

I_{ac} is the small fraction of I_{dc}, to ensure linearity in more complex system. The flux of minority carrier into the surface can also be resolved into corresponding dc and ac component [225].

$$g(t) = g_{dc} + g_{ac}\sin(\omega t) \tag{2.17}$$

The accumulated surface charge $Q_s(t)$ oscillates periodically, and the time dependent charging, transfer and recombination terms are replaced by the sum of their steady state and periodic equivalents [225].

$$Q_s(t) = \frac{qg_{dc}}{k_{tr}+k_{rec}} + \frac{qg_{ac}(k_{tr}+k_{rec})}{(k_{tr}+k_{rec})^2+\omega^2}\sin(\omega t) - \frac{qg_{ac}\omega}{(k_{tr}+k_{rec})^2+\omega^2}\cos(\omega t) \tag{2.18}$$

Thus we can write photocurrent density J_{photo} as [225]

$$J_{photo} = \frac{qg_{dc}k_{tr}}{k_{tr}+k_{rec}} + \frac{qg_{ac}(k_{tr}(k_{tr}+k_{rec})+\omega^2)}{(k_{tr}+k_{rec})^2+\omega^2}\sin(\omega t) - \frac{qg_{ac}\omega k_{rec}}{(k_{rec}+k_{tr})^2}\cos(\omega t) \quad (2.19)$$

This expression can also be expressed in dimensionless complex form [225].

$$\phi(\omega) = \frac{j_{photo}\,(\omega)}{qg_{ac}} = \frac{k_{tr}+i\omega}{k_{rec}+k_{tr}+i\omega} \quad (2.20)$$

The corresponding real components of the IMPS response are [225]

$$Re\left(\frac{j_{photo}}{qg_{ac}}\right) = \frac{(k_{tr}+k_{rec})k_{tr}+\omega^2}{(k_{tr}+k_{rec})^2+\omega^2} \quad (2.21)$$

The imaginary component is given by equation 2.22 [225]

$$Im\left(\frac{j_{photo}}{qg_{ac}}\right) = \frac{k_{rec}\omega}{(k_{tr}+k_{rec})^2+\omega^2} \quad (2.22)$$

Where, k_{tr} and k_{rec} are the rate of transport and recombination. These equations predict a semicircular plot in complex plain. It has been seen that diameter of the IMPS semicircles decreases as the potential becomes more negative, and the band bending increases. Intercept at higher frequency corresponds to electron current density when the recombination is absent, while the lower frequency intercept corresponds to steady state current. Sum of the rate constants (k_{tr} + k_{rec}) is derived from the frequencies, ω_{max} at which maxima in the semicircular plot appears. The $k_{tr}/(k_{tr}+k_{rec})$ can be obtained from the low and high frequency intercept after normalization.

The experimental setup consists of LED's of different peak wavelengths and fairly constant response over all frequency range, as measured in terms of average optical power output; they are modulated using a voltage source (frequency generator (Tektronics AFG 320)). The sample is illuminated uniformly throughout the electrode, the photocurrent from the device is measured at each frequency and frequency is varied over a wide range (1 Hz to 100 KHz). The device signal is measured using lock in amplifier (SR 830) which uses function generator TTL as reference. The Figure 2.20 gives a schematic diagram of the IMPS setup used.

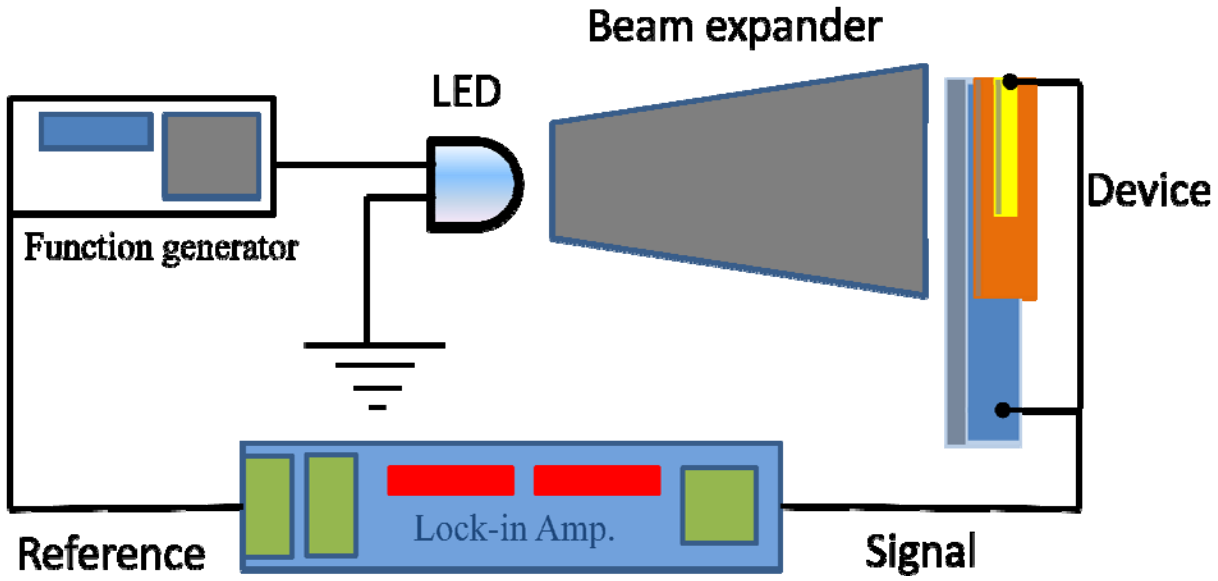

Figure 2.20 : Schematic diagram of IMPS setup using LED and beam expander to have a uniform illumination of the sample.

By modeling the equation for current, one can find out the rates for transport and recombination. The response at lower frequency can give idea about transport, either dominated by recombination of charge carriers or independent of recombination.

CHAPTER 3

STEADY STATE AND TRANSIENT STUDIES

3.1 Introduction

To study the OI hybrid heterojunction systems, it is required to understand methods of charge generation which can be through injection or photoexcitation, transport of charge carriers in presence of fields and trap states and finally the role of recombination. Photo – generation of charge carriers in these OI hybrid bilayer type devices are limited to the interface region between organic and inorganic semiconductors. The interface provides the potential for dissociation of exciton into free charge [226,227]. The charge generation in inorganic semiconductor is independent of this field as the exciton binding energy is very less (~ 25-50 meV) [228] and can be dissociated easily via thermal energy (k_BT =25meV at RT), thus the charges are generated equally at interface and bulk. In case of organic semiconductor the exciton binding energies are higher (~ 0.2 – 1 eV) [229] compared to room temperature thermal energy thus they require an external field to dissociate into free charge carriers. The charges generated at the interface can be easily trapped in the defect sites present at the interface of OI diode. The capacitance – Frequency measurement can give an estimate to the density of trap states present at the interface between organic and inorganic semiconductors. The IMPS measurement, which largely is modeled using the generation and recombination effects, can also give an idea of bulk recombination processes playing role.

In this chapter we will be dealing with the energy level alignment in the polymer/n-GaN hybrid diodes. The barrier height can be roughly estimated from the energy diagram figure 3.4. It will be seen that for these systems the built in voltage is not same for electron and hole transport. The offset in band alignment plays important role in the responsivity, as will be seen in next chapter. We will discuss the results of the steady state measurements performed on the OI hybrid heterostructure diodes and their implications. The known models have been used to extract various transport parameters, which are essential for further device applications.

Organic – Inorganic Hybrid heterostructure diodes

As mentioned in chapter 2, the inorganic semiconducting material used in OI devices, the n-doped Gallium Nitride is a wide band gap semiconductor with an E_g = 3.4 eV. It is almost transparent to wavelengths below 450 nm, with absorption coefficient less than 5×10^2 cm^{-1} [230]. The band gap of n-GaN corresponds to absorption at 365 nm. When excited at a wavelength of 320 nm, PL emission is visible at 375 nm along with a huge defect state emission centered at 550 nm and a band width span of 100 nm as shown in Figure 3.1 (a). The intensity of PL emission measured at 550 nm maximizes for 362 nm excitation as is shown in the plot of excitation energy versus emission intensity in Figure 3.1 (b). It can be guessed that the defect state density is large, which also corresponds to lower carrier mobility (250 cm^2/V.s). pBTTT has a band gap of 1.94 eV which has a maxima in absorption at 520 nm, the overlap between the emission width of n-GaN defect states and absorption band of pBTTT is large as shown in Figure 3.2. When pBTTT polymer layer is coated over the n-GaN substrates, the defect state emission decreases at 550 nm while the PL emission around 632 nm increases. This emission is at lower wavelength compared to the PL emission of the polymer, which is around 720 nm as shown in chapter 2 (Figure 2.2). For 365 nm excitation the PL emission at 632 nm is highest, as shown in Figure 3.3. This suggests the formation of some high energy state compared to polymer PL emission state at the interface of n-GaN and pBTTT.

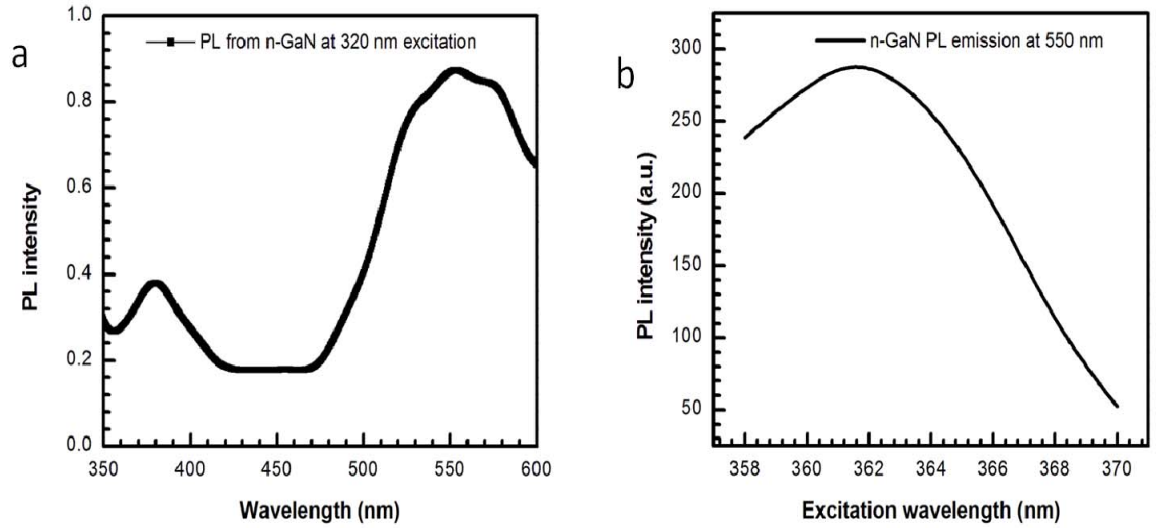

Figure 3.1 : a) PL emission from n-GaN for 320 nm excitation. b) Excitation wavelength versus PL emission intensity at 550 nm for n-GaN.

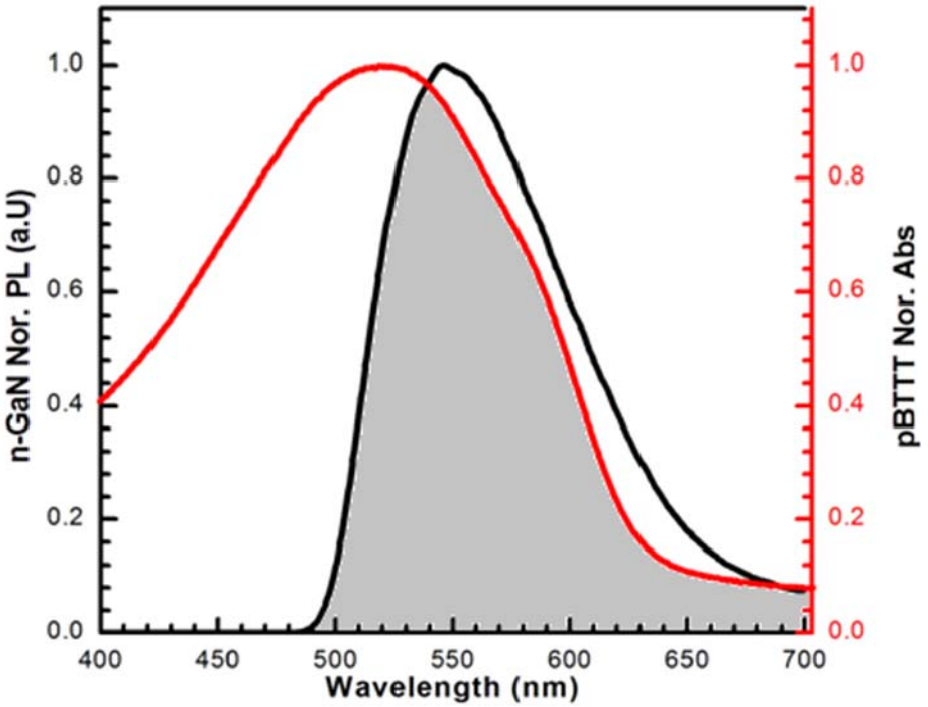

Figure 3.2 : Overlap between the absorption of pBTTT (red) and emission of n-GaN defect state (black). Overlap area has been shaded.

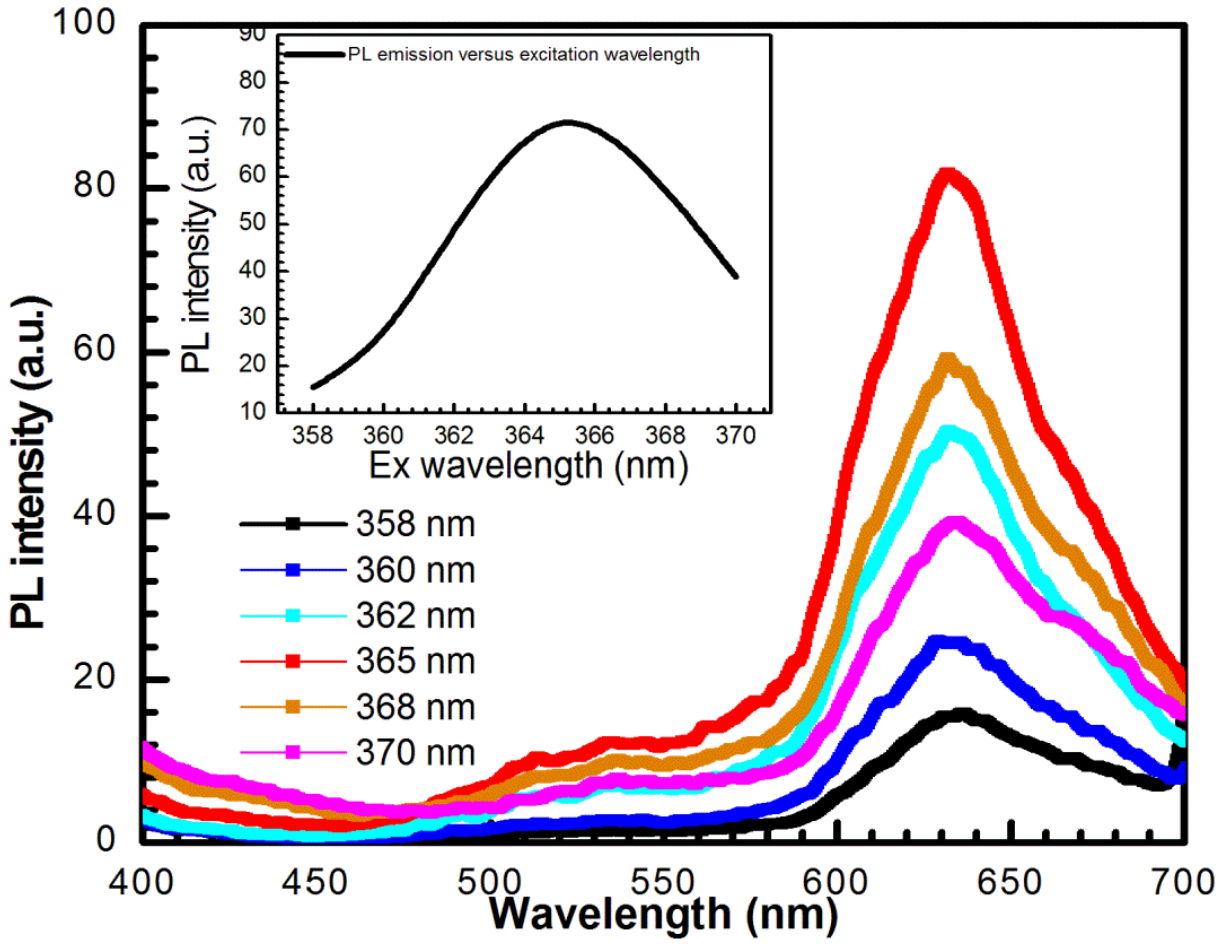

Figure 3.3 : PL emission from n-GaN/pBTTT hybrid interface at different wavelength. PL emission intensity versus n-GaN excitation wavelength (inset).

The conduction band minima for n-GaN lies at -3.4 eV, which is very close to LUMO of pBTTT (-3.46 eV) and P3HT (-3.3 eV), and the valance band maxima of n-GaN lie at -6.4 eV, which is well below the HOMO of pBTTT (-5.4 eV) and P3HT (-5.02 eV). Thus there is an extra offset between the valance band of n-GaN and HOMO of the polymers for hole transport as is shown in the Figure 3.4 (a). Figure 3.4 (b) shows a schematic of band alignment when the semiconducting layers are brought in contact.

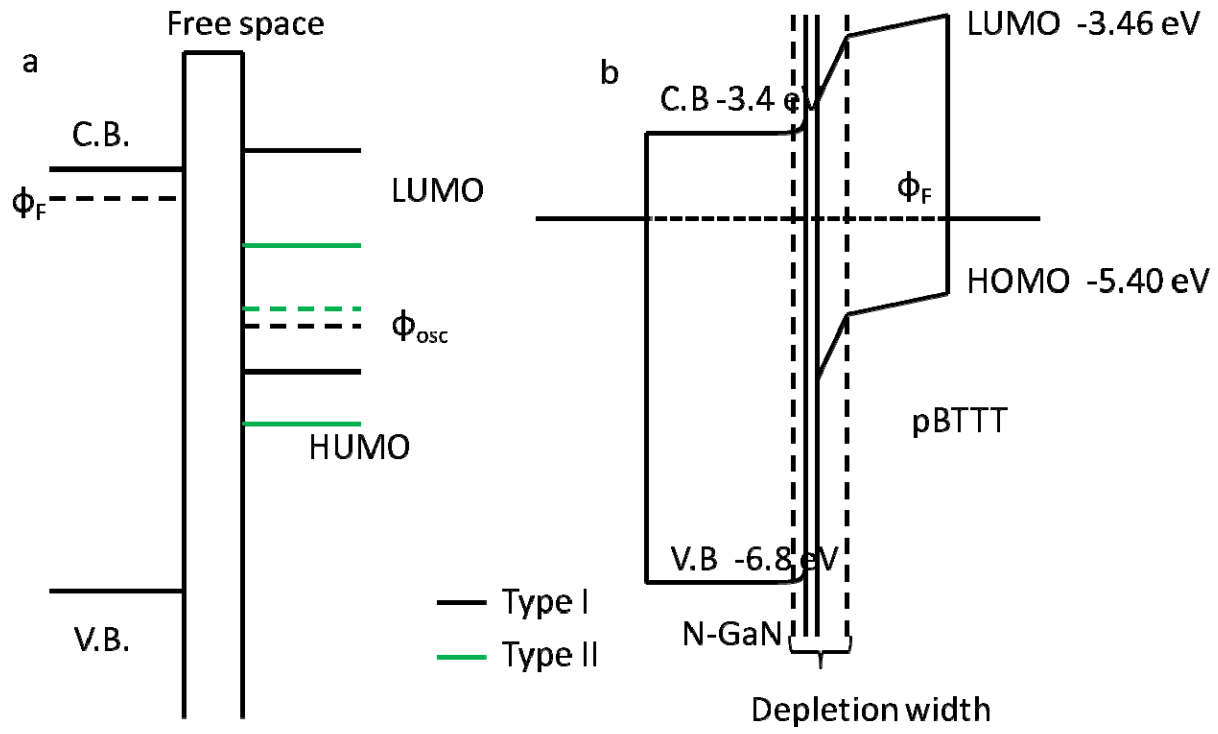

Figure 3.4 : Energy levels of inorganic and organic semiconductors under noncontact mode, type I (black) and type II (green) energy structures has been shown. b) Possible band bending at the OI interface under contact.

The case for type I band alignment which arises in case of pBTTT and P3HT are completely different from the case of type II band alignment as in N2200. For type I structure gold (Au) electrode is used for injecting holes into the HOMO of the polymer semiconductor and indium (In) electrode injects electron in conduction band of n-GaN. The offset in the Fermi levels for n-type and p-type regions causes the charge flow as soon as they are in contact. This charge flow causes the formation of built in field V_{bi} for p-n junction or a barrier ϕ_B in case of MS junction at the mechanical interface. There is also a formation of depletion region which is larger in organic polymeric semiconductor (W_{osc}) and smaller in inorganic region (W_{GaN}). This built in field present at the p-n junction gives rise to rectification in I-V curve. The saturation current density is limited largely by the temperature of diode while measurement and built in voltage. Using the expression $J_{Sat} = \mathcal{A}^* T^2 exp\left(-\frac{q\phi_B}{kT}\right)$, the barrier height can be calculated, where $\mathcal{A}^*$is the Ridhardson constant which is calculated using effective mass of the free charge

carrier in the semiconductor. Light illumination on the OI diode gives rise to photogenerated charge carriers. These charges give rise to an additional current in the reverse bias, which is due to the enhanced collection efficiency when operated in photoconductive mode. These devices also give a significant V_{oc} and J_{sc} when operated in the photovoltaic mode. The generation mechanism of these charges in organic semiconductor absorption region can be pictured by using the exciton concept.

To understand the carrier transport mechanism, understanding of device transport parameters are essential. The Carrier trapping and recombination effects play a significant role in deciding the mobility of the carriers. The knowledge of trap density present at the interface and bulk is useful to quantify the decrease in efficiency. Many complex processes which can give rise rather simple characteristics like I-V or C-V, needs to analyzed using models to derive the carrier transport parameters.

3.2 Measurement and Analysis

With the discussion on the energy level alignment and band structure diagram, we will now look at the experimental results and evaluated parameters. The band structure shown in figure 3.4 depicts the case for a perfectly ideal system, which is not the case in real materials which are more or less defective. Thus the characteristics expected from these OI diodes will also deviate from ideal curves. The effect of structural defects, charge carrier traps, foreign impurities and measurements conditions will have a significant effect on the measured electrical properties and corresponding related phenomena. In the measurement and analysis section we will try to explain the effect of such imperfections qualitatively or quantitatively, their possible effects on transport and related parameters.

3.2.1 Current – Voltage Characteristics (I –V curves)

Current – Voltage characteristic has been a very basic characterization technique in semiconductor device industry. Apart from giving valuable information about the transport process and efficiency, the technique is also used very extensively for optimizing device application. In the current work the I – V characteristics has been utilized to look at the transport properties in terms of the models used to fit the experimental curve and extract the transport

parameters like V_{bi} and ideality factor for the OI diode. Dark I –V's have been fitted to two step mechanism of charge transport, where the low current part has been modeled using thermionic emission curve, which also give the diode ideality factor "n" and the high current part is modeled using the space charge limited current which gives the B and m values for the transport. I – V under illumination shows a significant light response from the OI hybrid heterostructure diode. The light generation and corresponding increase in current has not been modeled to account for factors affecting the generation of charge carriers.

n-GaN/pBTTT hybrid system

The OI hybrid system consists of n-GaN as n-type layer and pBTTT as p – type layer, the PProDOT is used as buffer layer and Au as hole injecting electrode. The dark I-V curve for these hybrid system OI diodes is rectifying with a rectification ratio of 10^3. I-V has been measured by applying a voltage sweep from +1 to -1 and measuring current across the device, where n-GaN is given a negative bias as compared to gold. The reverse saturation current density is less ~ 500 nA/cm^2 and the forward current density at 1 V is 10mA/cm^2. Figure 3.5 shows a representative dark I-V for n-GaN/pBTTT hybrid device. The semi log shows that no space charge layer is present as the slope of the curve is not changing.

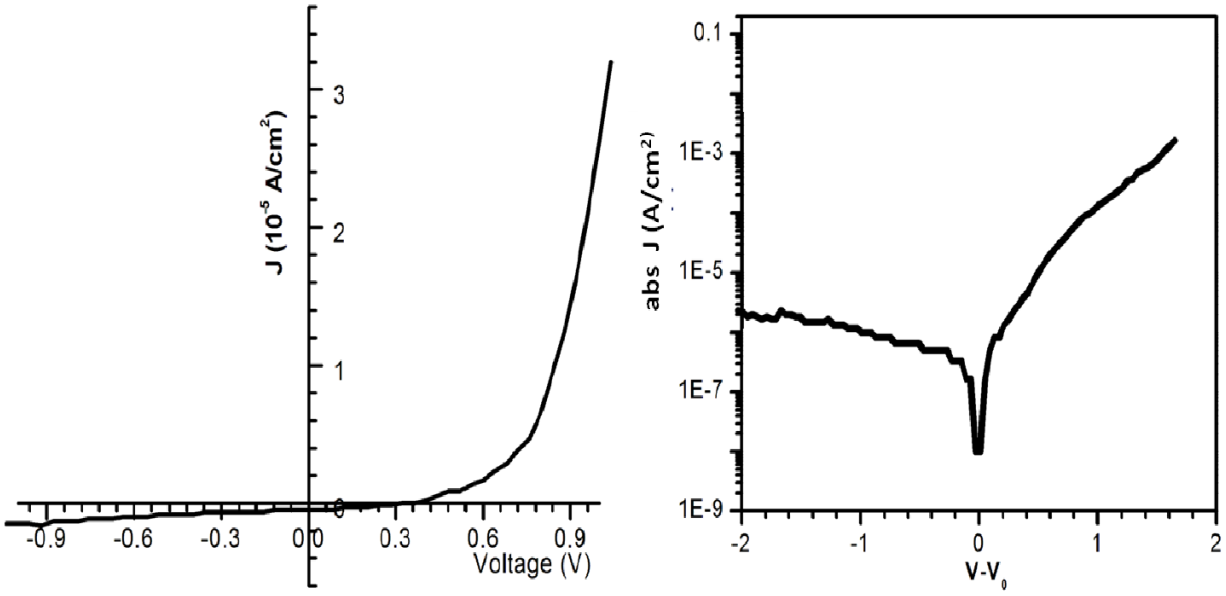

Figure 3.5 : Linear and semi log Plot of dark I –V curve for n-GaN/pBTTT hybrid diode.

As can be noticed from the dark I –V plots that the saturation current density is less than a μA for lower reverse biased voltages. The important point to be noticed is the presence of additional voltage V_0 in dark I – V which is mainly a characteristics of light I –V response. The current density at zero applied voltage is not zero but has a significant negative value. The origin of such a voltage is not clear as there is no external source present for carrier generation apart from injection from the electrodes. Along with this voltage there is a barrier for charge transport whose height can be calculated using saturation current density, the height of the barrier can be close to 0.70 V as can be speculated from the threshold of linear I-V curve.

The semi log I –V has been modeled using thermionic emission for lower current density (< 10 μA/cm^2) shown in Figure 3.6 . The space charge region was not observed in the range of measurement. The model parameters used are the diode ideality factor "n" in thermionic emission model. The voltage has been reduced to V – V_0 to take care of the extra built in voltage V_0, where V_0 for given n-GaN/pBTTT system is 0.44 V. The value for barrier height as calculated from saturation current density of 800 nA/cm^2 is ~ 0.60 eV which is a little less than what was speculated from I-V and the band diagram for n-GaN/pBTTT. The effective mass (m^*) of hole, for pBTTT, was taken to be 1.61 m_e as given in literature [231]. The diode ideality factor "n" as calculated from the thermionic emission model fit to semi log dark I-V is n ~ 11.34 ± 0.02 which is much higher as compared to an ideal diode.

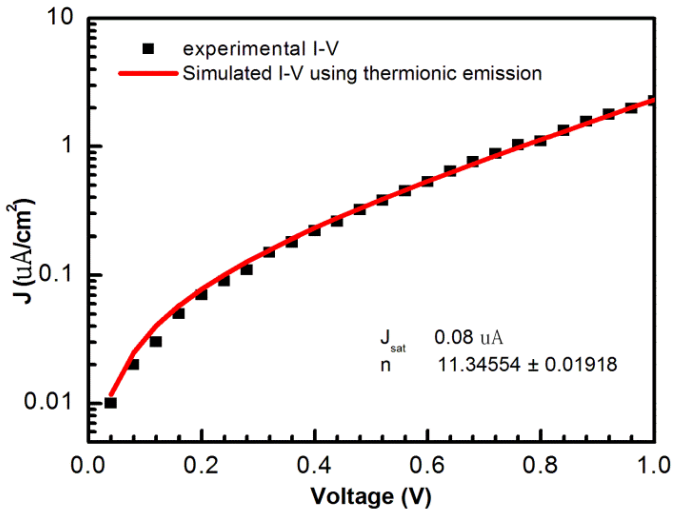

Figure 3.6 : Thermionic emission model fit to forward current – voltage characteristics for n-GaN/pBTTT hybrid devices.

A significant light response has been observed in this system, the power output for light input is very low (efficiency ~ 10^{-3}), but the short circuit current density is sufficient enough to understand the light response of the system. Figure 3.7 (a) shows a dark and light I-V for a n-GaN/pBTTT system, where the voltage generated (V_{OC}) is around 0.6 V and short circuit current J_{sc} = 10 μA/cm^2. Figure 3.7 (b) shows wavelength dependence of I-V, measured under 5mW intensity at 370 nm and 522 nm respectively. The difference in J_{Sc} and V_{OC} are quite large for two different illuminations.

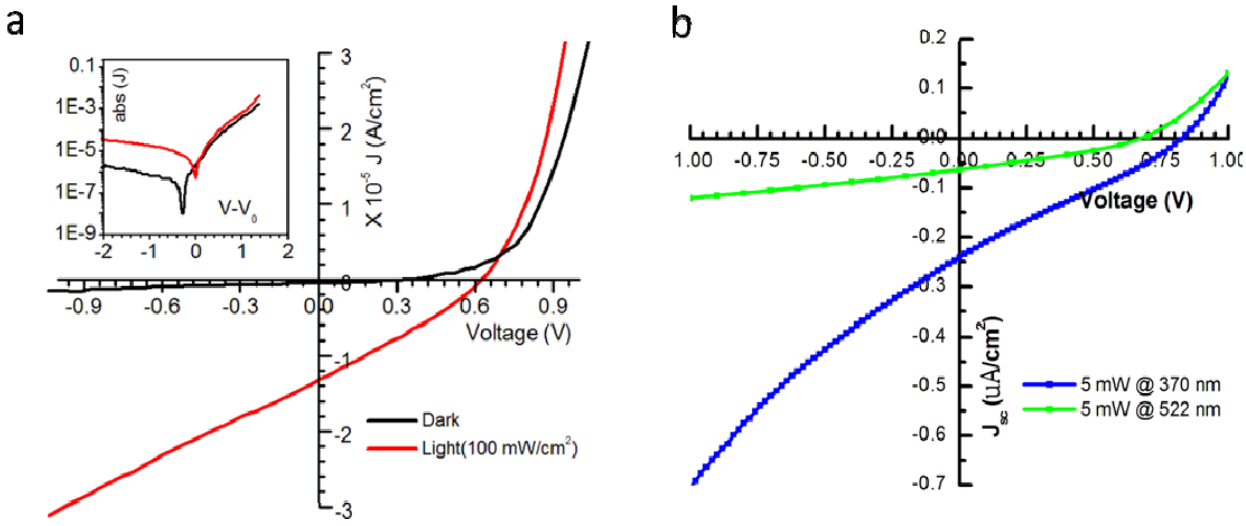

Figure 3.7 : a) The Dark and light I-V for n-GaN/pBTTT system. Inset shows the log – normal plot of dark and light I-V. b) Wavelength dependence of I-V.

The voltage and current value increases with illumination intensity, the V_{OC} saturates at higher voltage. Current response for incident photo flux density remains linear with photon flux in log – log plot for over two decades as is shown in figure 3.8. The J_{Sc} variation with intensity has been modeled using the equation $J_{Sc} \propto I^{\alpha}$ where α is a constant for a particular response. The variation of V_{OC} with intensity has been modeled using the relation $V_{OC} \propto Sln\left(I/I_0\right)$. The values for α are 0.734 (370 nm) and 0.852 (522 nm) which shows that the J_{Sc} variation with intensity is more close to linear for 522 nm illumination, which implies less trapping effects playing role. Values for S obtained from the fit are 0.053 V (370 nm) and 0.34 V (522 nm) which is much higher compared to kT/q (0.025 V). The nonlinear dependence of J_{Sc} on I and higher value of S for the V_{OC} versus Intensity plot suggests that the quasi Fermi level is not constant throughout

the device. Carrier transport experiences significant influence of trapping of carriers. The loss mechanism involved is not only bimolecular recombination but other loss mechanisms are also present [232]. Figure 3.7 shows the fitting for the J_{Sc} versus Intensity and V_{OC} versus Intensity.

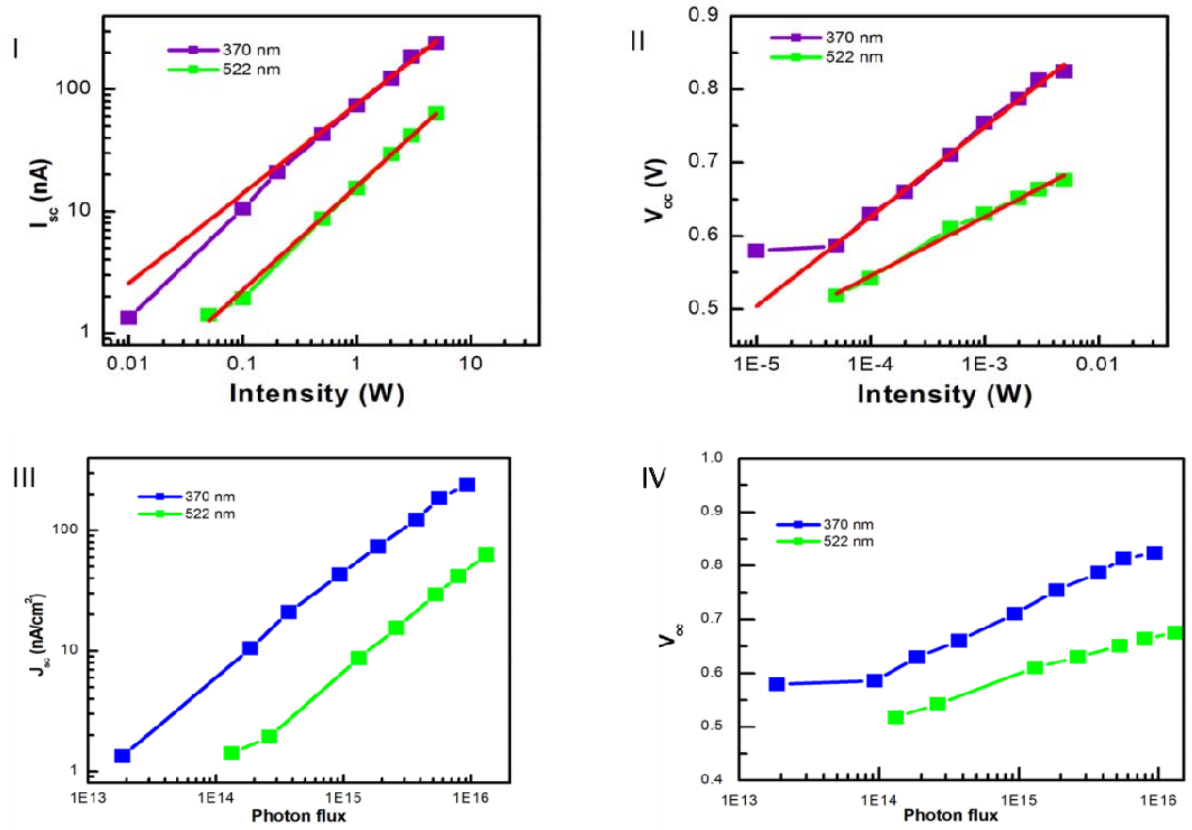

Figure 3.8 : I) $\boldsymbol{J_{Sc} \propto I^{\alpha}}$ fit to J_{Sc} versus I plot. II) $\boldsymbol{V_{OC} \propto Sln\left(I/I_0\right)}$ fit to V_{OC} versus I plot. III) J_{Sc} versus photon flux showing almost linear behavior. IV) V_{OC} versus photon flux on a log – linear plot shows the saturation nature of open circuit voltage.

From these measurements it can be seen that the n-GaN/pBTTT hybrid system forms a heterostructure diode, with good rectification ratios and low dark saturation current density. The current transport under applied field has been mainly modeled using thermionic emission model. OI diode also has a significant light response with V_{OC} and fill factor close to all polymer BHJ's. For few measured diodes the break down voltages were found to be higher than 10 V, while the reverse dark current densities less than 100 nA. It is not clear as why the current and voltages generated while illumination is much less than expected from the band gap and

absorption coefficients. Charge generation is limited by the interface region for the major absorption region and presence of traps at the interface can be one possible reason for lower efficiency.

n-GaN/P3HT system

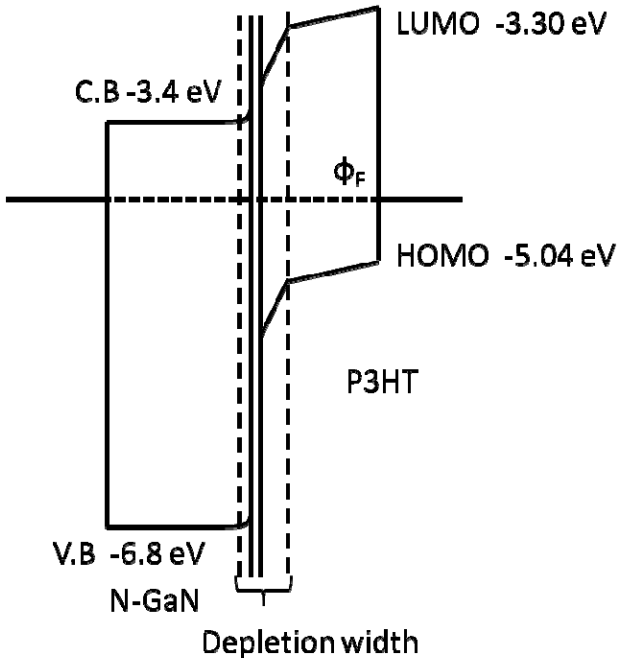

Figure 3.9 : Energy band diagram for n-GaN/P3HT hybrid system**.**

The n-GaN/P3HT system is another type I heterostructure studied in this work. The HOMO and LUMO of P3HT is off by only 0.3 eV from pBTTT. Where the LUMO of pBTTT is a little below - 3.4 eV making it a type II heterostructure ideally, P3HT is type I structure with LUMO at - 3.3 eV, as shown in Figure 3.9. From the energy band diagram it is expected that the transport properties or the measured electrical characteristics should not differ much from that measured for pBTTT. This structure can give an idea about the effect of band shifts on electrical characteristics, while it can also be used to verify the parameters calculated for pBTTT. For this case we will be discussing only the light and dark I – V and corresponding modeling to extract the device parameters. The methods and parameters used for I – V measurement remains same as pBTTT. Figure 3.10 shows the linear and logarithmic I – V plots for a n-GaN/P3HT hybrid heterojunction diode system.

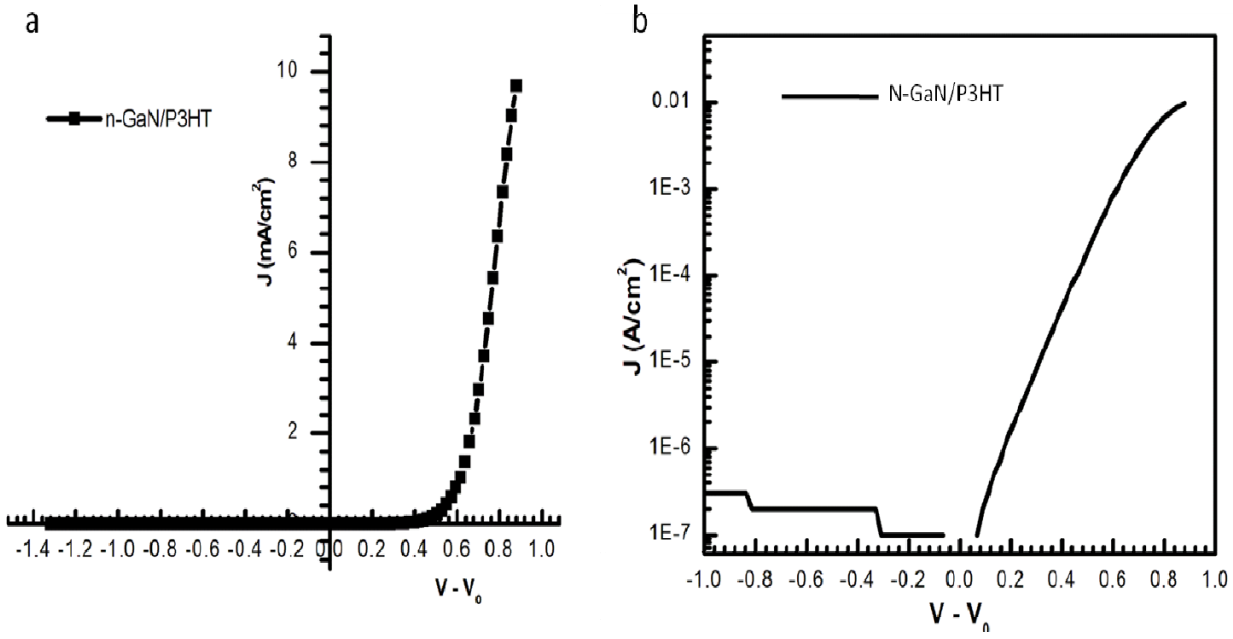

Figure 3.10 : I –V plot for n-GaN/P3HT hybrid devices a) linear and b) semi logarithmic.

The dark I – V curves for n-GaN/P3HT devices are better in comparison to n-GaN/pBTTT hybrid devices. The rectification ratio of 10^4 and dark saturation current density ~ 100 nA/cm^2 are almost comparable, the diode ideality factor calculated using thermionic emission fit to the experimental data is n= 2.258 ± 0.001 which is much less compared to that of n-GaN/pBTTT showing that an ideal type I energy structure makes better diode. The thermionic fit to the experimental measured dark I –V for lower current density (~ 1mA/cm^2) is shown in Figure 3.11, it can also be notices that the current densities are higher for same applied bias as compared to n-GaN/pBTTT devices. An offset in voltage was observed in dark I –V when the current changes its polarity the magnitude is not fixed but varies from device to device. This offset voltage has been taken care while fitting the curve by using $V - V_0$, here V_0 the offset voltage is 0.32 V. Assuming the MS junction between n-GaN and P3HT the barrier height has been calculated using effective hole mass (m^*) of 1.71 m_e along the $\pi - \pi$ stacking direction [231]. The barrier height as calculated using saturation current density is ~ 0.85 eV which is higher than that expected from the I-V onset.

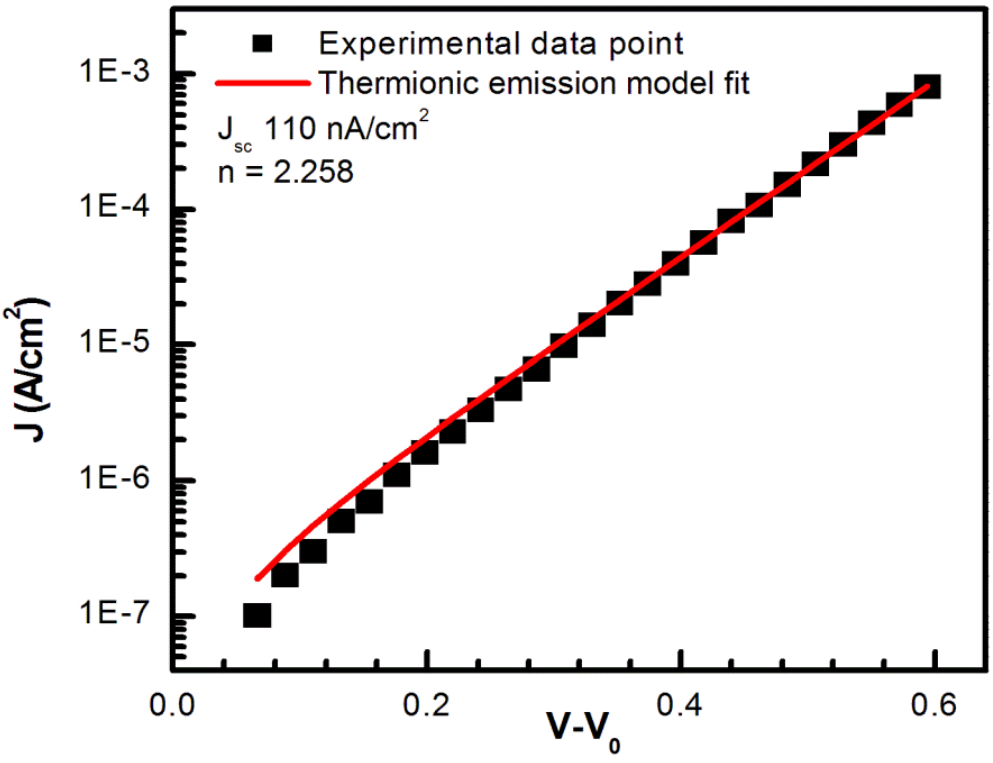

Figure 3.11 : Thermionic emission model fit for forward I-V of n-GaN/P3HT devices for lower current density (~ 1mA/cm^2).

The n-GaN/P3HT hybrid diodes also show photo response when illuminated. The measured short circuit current and open circuit voltage is almost similar to n-GaN/pBTTT device which is a little surprising as this structure has better energy matching for charge transport. Thus this suggests that there can be other reasons along with lower offset for electron transport between the polymer and n-GaN layer. Figure 3.12 shows a representative I –V for light response of n-GaN/P3HT hybrid diodes. As will be shown in next chapter, these devices show photocurrent response over the entire absorption range of the semiconducting material.

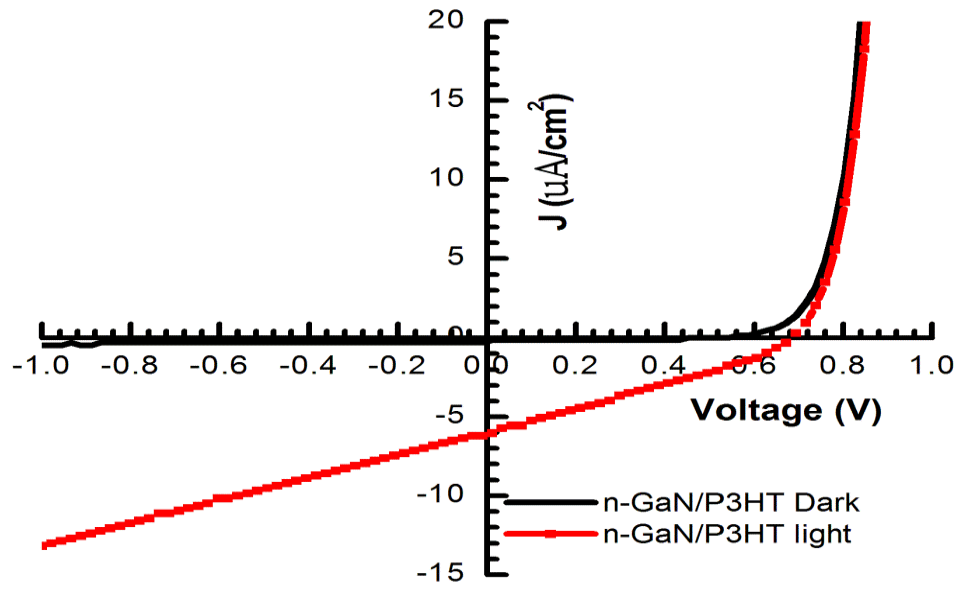

Figure 3.12 : Light and dark I –V for n-GaN/P3HT devices. The light response is similar to the n-GaN/pBTTT hybrid devices.

The hybrid devices with type I heterostructure show good rectification and lesser saturation current density, the light response is significant with a sizable current in photovoltaic and photoconductive mode. Origin of extra voltage as observed in both the cases of type I energy structure is not understood. Effect of shift toward type I energy structure is visible as the difference in the response of n-GaN/pBTTT and n-GaN/P3HT devices, where second structure is closer to type I structure. In both the cases, decreased photo current response on illumination is not clear even though dark conductivity and V_{OC} values are comparable with other photovoltaic structures.

To look at the effect of shift in energy structure more towards type II heterostructure, n-GaN/N2200 devices were also measured. In the next section we will see that the shift towards better type II heterostructure is more clearly visible in the electrical characteristics of the hybrid devices.

n-GaN/N2200 hybrid heterojunction diodes

Hybrid devices fabricated using N2200 do not form a p-n junction with n-GaN, as both the materials are electron transporting. The structure can be seen as the n-n heterostructure where n-

GaN side can act as metal while the N2200 acts as semiconductor, figure 3.13 shows the energy band structure for n-GaN/N2200. The top electrode used in this case is Au as well as Al. It will be shown that the n-GaN/N2200 interface acts as the barrier for charge generation in N2200 absorption region, the collection efficiency is higher in case of Al than Au, which is also valid from the fact hole mobility is very low as compared to electron mobility in N2200, and thus the hole current will be negligible.

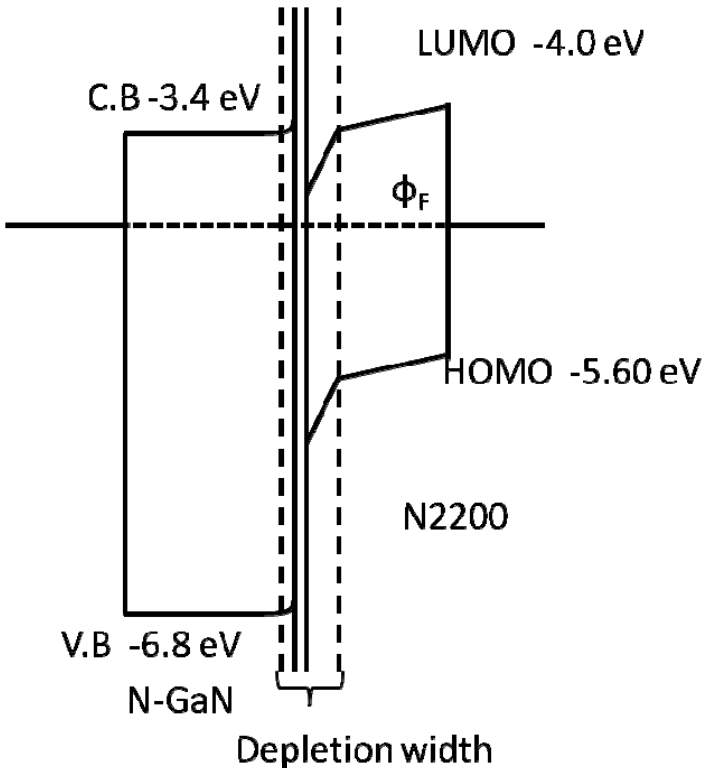

Figure 3.13 : Energy band structure for n-GaN/N2200 n-n heterostructure.

It can be seen that the I-V of type II heterostructure is completely different from that of type I energy structure. There is no stray offset voltage in the dark I-V curve for either Al or Au electrode. The turn on voltage is higher for Al electrode, while the space charge region is visible for Au electrode showing the decreased electron injection efficiency of Au in N2200. While the dark saturation current densities are high compared to p type semiconductors, which is not very obvious from the band diagram as shown in Figure 3.13. Figure 3.14 shows the dark I –V curve for Al and Au top electrode devices.

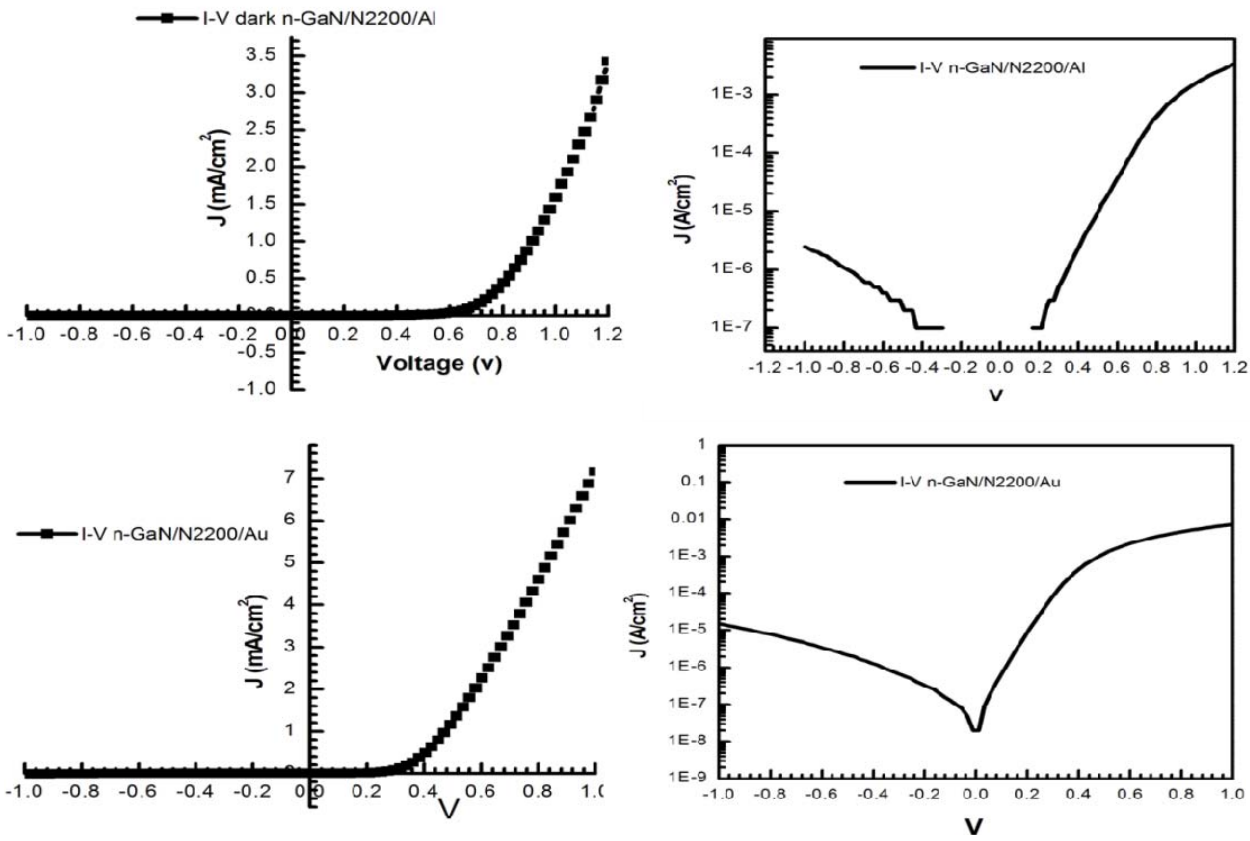

Figure 3.14 : Dark I-V linear and semi logarithmic for n-GaN/N2200/Al and n-GaN/N2200/Au. It should be noticed that there is no offset in the dark I –V. The space charge effects are clearly visible for gold electrode.

The dark I-V curve for n-GaN/N2200/Al has been fitted to thermionic emission for lower current (< 1 mA/cm^2) and space charge models for higher current (> 1 mA/cm^2). The diode ideality factor calculated was $n = 3.14 \pm 0.03$ which is lesser than n-GaN/pBTTT devices. The expression used for space charge fit was $B(V_{app} - V_0)^m$ the "B" and "m" values found from the fit where $B = 0.0087 \pm 2 \times 10^{-4}$ and $m = 1.98 \pm 0.08$, where m value is little less than Mott – Gurney current model, which can be due to influent of trap on transport . The diode ideality factor for n-GaN/N2200/Au is $n = 2.40 \pm 0.006$ and the values for B and m are $B = 0.012 \pm 3 \times 10^{-3}$ and $m = 1.28 \pm 0.04$. Thus the Au top electrode diodes are closer to linear regime of charge transport at higher current densities. Figure 3.15 shows the fit for n-GaN/N2200/Al and n-GaN/N2200/Au devices.

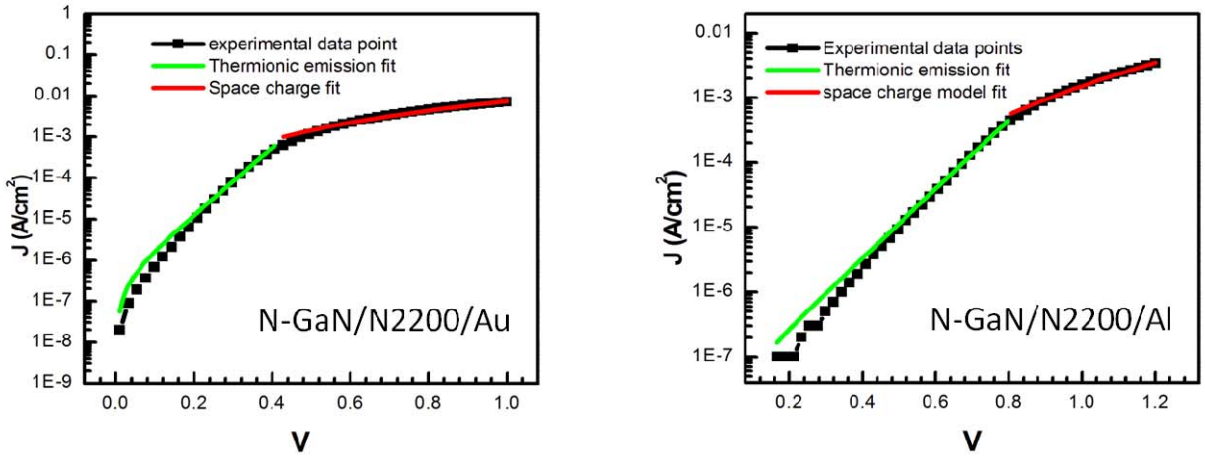

Figure 3.15 : Thermionic emission (Green) and space charge (red) fit to n-GaN/N2200/AU and nGaN/N2200/Al devices. Where the Au top electrode devices fit better to the space charge model.

The light response was also measured for these devices to see the photo response of type II energy structure. The light response for n-GaN/N2200/Al is significant in photoconductive mode, while n-GaN/N2200/Au shows no light response, which can be explained by the reason that Au electrode provide very high barrier for electron collection. Figure 3.16 shows the light response of n-GaN/N2200/Al devices, where the most important point to notice is the large current density in photo conductive mode.

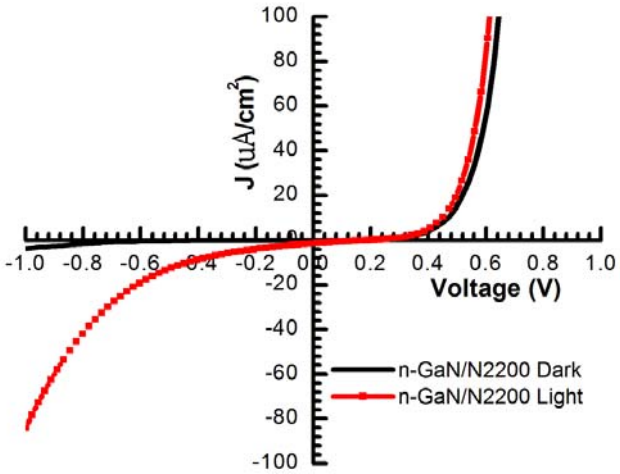

Figure 3.16 : Light and dark I-V for n-GaN/N2200/Al devices.

The open circuit voltage and short circuit current density is almost zero for this device, but as the device is reverse biased the photo generated carrier collection efficiency increases. The role of type II energy structure in such increased collection efficiency is not understood. The important parameters for OI hybrid diode structure have been summarized in Table 3.1, at the end of this chapter.

In present study I-V characteristics were measured to understand the transport mechanism and other factors which effect charge transport. The type I energy structure diodes show no space charge region in their dark response and light response is similar to other p-n junctions, the type II energy structure has a completely different behavior, they show space charge regions clearly but the light response is not obvious. More experimental measurements are required to derive a definite trend for effect of type I and type II energy structure alignment for OI diodes I –V characteristics.

3.2.2 Capacitance – Voltage measurement

Capacitance – Voltage measurement is one of the very well studies techniques for depletion layer characterization in case of p-n junction diode. The small signal admittance from the p-n junction gives valuable information about the presence of fixed barrier layer or changing depletion layer present in p-n junction [233]. This method has also been applied well for studying the depletion width and doping profile of the p-n junction [234]. The basics of this method have been discussed well in chapter 2, in this section we will be looking at the experimental data for n-GaN/polymer hybrid heterostructure diodes.

n-GaN/pBTTT Hybrid diode

As seen through I-V measurement the n-GaN/pBTTT hybrid heterojunction diode forms a rectifying junction, the built in potential and doping profile can be derived from the capacitance-voltage characteristics. C-V measurement for n-GaN/pBTTT hybrid system shows that the depletion width changes with applied bias. While the C-V at different frequency can give information about the loss factors involved, the doping profile can be estimated from the $1/C^2_j$ versus V plot. Figure 3.17 shows C – V plot for pBTTT/n-GaN and $1/C_j^2$ versus V. It can be seen that the capacitance decreases monotonously with increasing voltage, which shows that the

depletion layer width is increasing as is clear from the expression used for calculating capacitance ($C = K_s\varepsilon_0 A/W$) where W is the depletion layer thickness. While the $1/C_j^2$ shows that the doping profile is not linear or abrupt, the form of this curve is more like third order of V, the fit has not been shown. Calculation of built in field gave values much higher than expected. A detailed analysis is required for such a curve to understand the nature of doping profile and depletion layer width variation with applied bias between n-GaN and pBTTT.

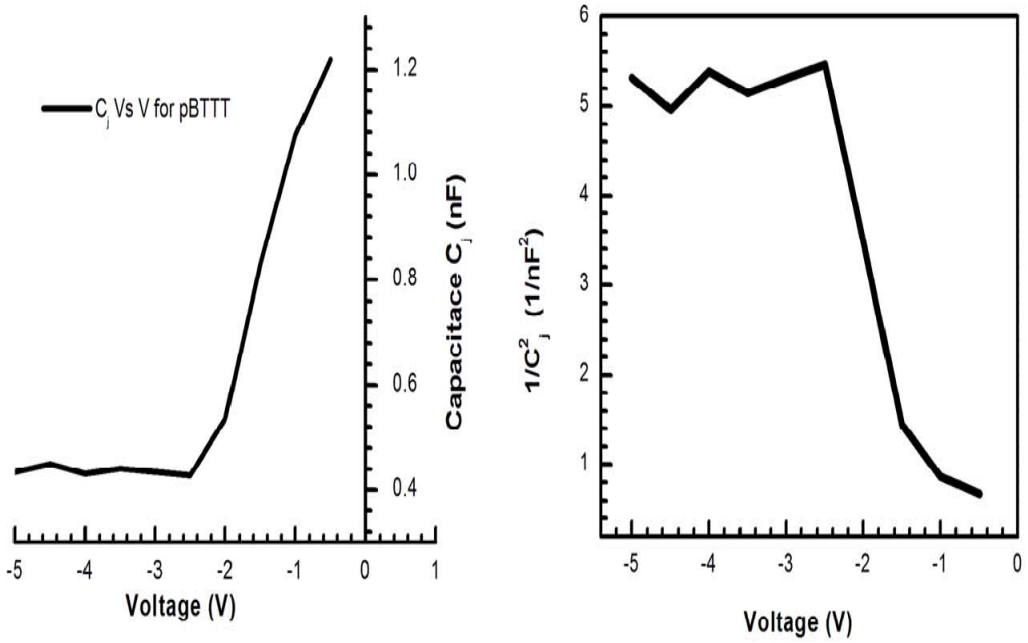

Figure 3.17 : C – V and $1/C^2$ – V plot for n-GaN/pBTTT hybrid diodes. The Nature of the curve is not like an abrupt or linearly graded junction.

An approximate plot for doping profile has been sketched in Figure 3.18. It can be derived from a simple relation between N_B (x) and derivative of Mott –Schottky plot. The equation 2.14 can be used for this plot. The plot shows the doping concentration to be saturating at the bulk doping concentration of pBTTT, which is reasonable value to an extent.

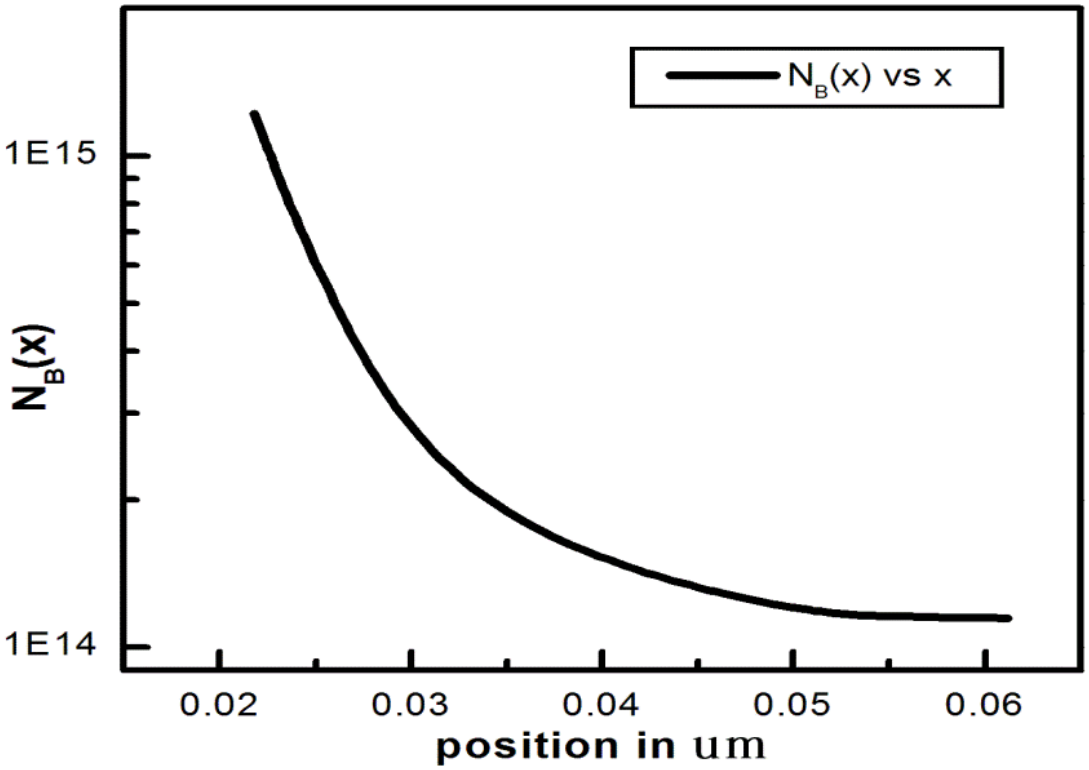

Figure 3.18 : Approx doping profile in n-GaN/pBTTT region where the position is measured from the highly doped region into the lightly doped region.

n-GaN/P3HT hybrid structure

The diodes made of n-GaN/P3HT are better in terms of ideality factor and rectification ratios. The C-V analysis for these systems show that the depletion width variation with applied voltage is completely different compared to n-GaN/pBTTT diode. Figure 3.19 shows the C versus V and $1/C_j^2$ versus V plot for n-GaN/P3HT devices. It can be noticed that the change in capacitance with increasing voltage is monotonic and the form of the curve is different compared to n-GaN/pBTTT devices.

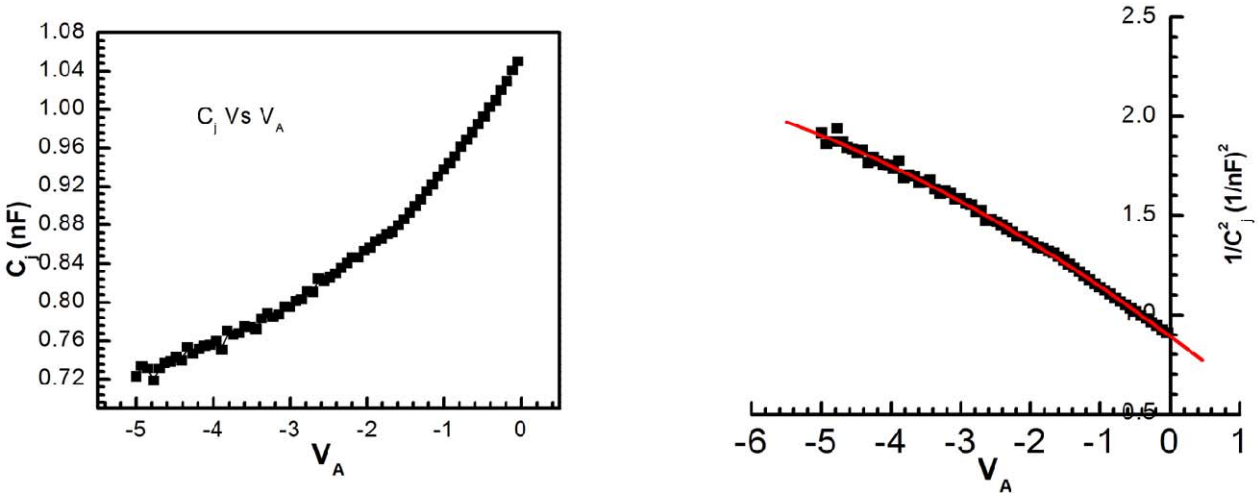

Figure 3.19 : C_j versus V_A and $1/C_j^2$ versus V_A plot with second order polynomial fit for n-GaN/P3HT hybrid diodes. A monotonic decrease in capacitance with applied voltage is visible in C_j versus V_A plot.

The calculation of V_{bi} using second order polynomial gives a value of 8.711 V which is more than 10 times off from the expected value (V_{bi} ~ 0.8 V). A multiplicative correction factor is required in the Mott – Schottky plot for the organic – inorganic hybrid structure structure.

The n-GaN/N2200 devices were also tested for C-V measurement, the data shows a peak in the capacitance in reverse biased state, which is unexpected for p-n junction or MS junction. Thus there is a requirement for further analysis and more measurements to ascertain the validity of results.

3.2.3 Capacitance – Frequency Measurement

Capacitance – Frequency or admittance spectroscopy has been a tool to characterize the trap states present in p-n junction or MS junction. The C –F curve can be used to locate the step in the capacitance when it changes from bulk capacitance to interface capacitance. This step can be reflected as a peak in conductance (G_P) versus frequency. Thus the frequency dependent capacitance and conductance measurement can be used to probe trap states at the interface of OI hybrid diodes. Figure 3.20 shows capacitance and conductance plot with respect to applied

frequency for n-GaN/pBTTT hybrid diode. The peak in conductance can be seen clearly which also corresponds to change in capacitance from bulk to interface.

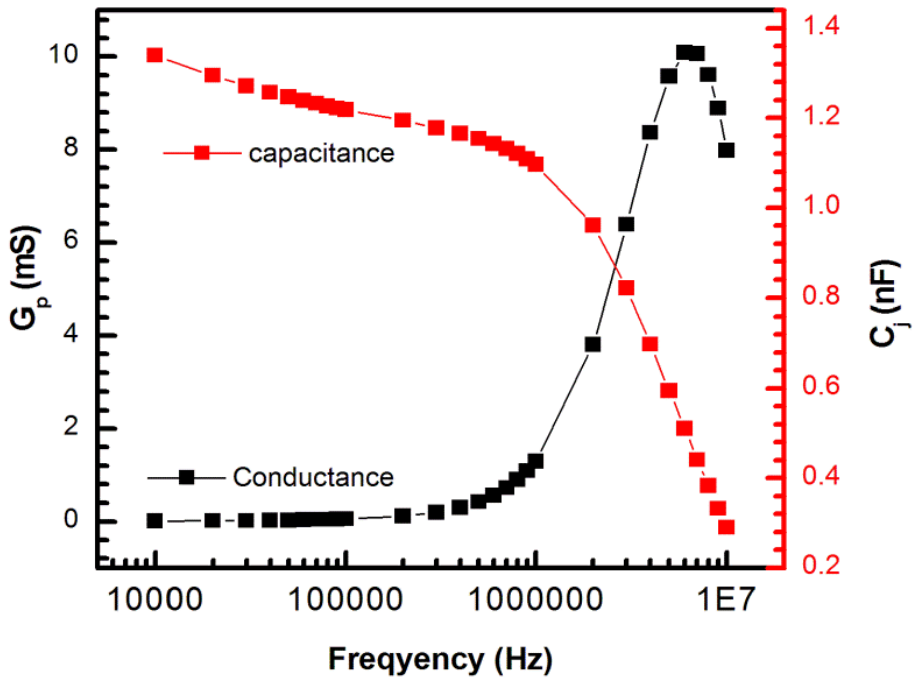

Figure 3.20 : Conductance and capacitance plot versus frequency for n-GaN/pBTTT device.

The effective trap density at the organic inorganic interface can be calculated approximately using single time constant (STC) model. Where the expression is given as,

$$\frac{G_P}{\omega} = \frac{qD_{it}\omega\tau}{(1+\omega^2\tau^2)} \qquad (3.1)$$

In equation 3.1, D_{it} is the density of defect states, and $(1+\omega^2\tau^2)$ has been optimized for $\omega\tau = 1$, τ is carrier relaxation time. The equivalent circuit has been shown in Figure 3.21.

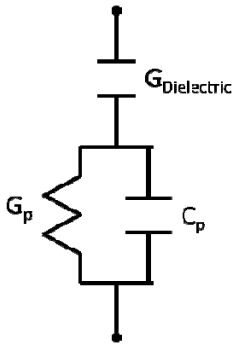

Figure 3.21 : Equivalent circuit for single time constant model.

Using STC model, an approximate, effective trap density has been calculated for n-GaN/pBTTT hybrid devices. The trap density calculated, for a device area of 0.06 cm^2, is of the order of 10^9 eV^{-1} cm^{-2}, which is an approximated value; the actual value can be still higher than calculated value. The model fit for G_p/ω versus frequency has been shown in Figure 3.22.

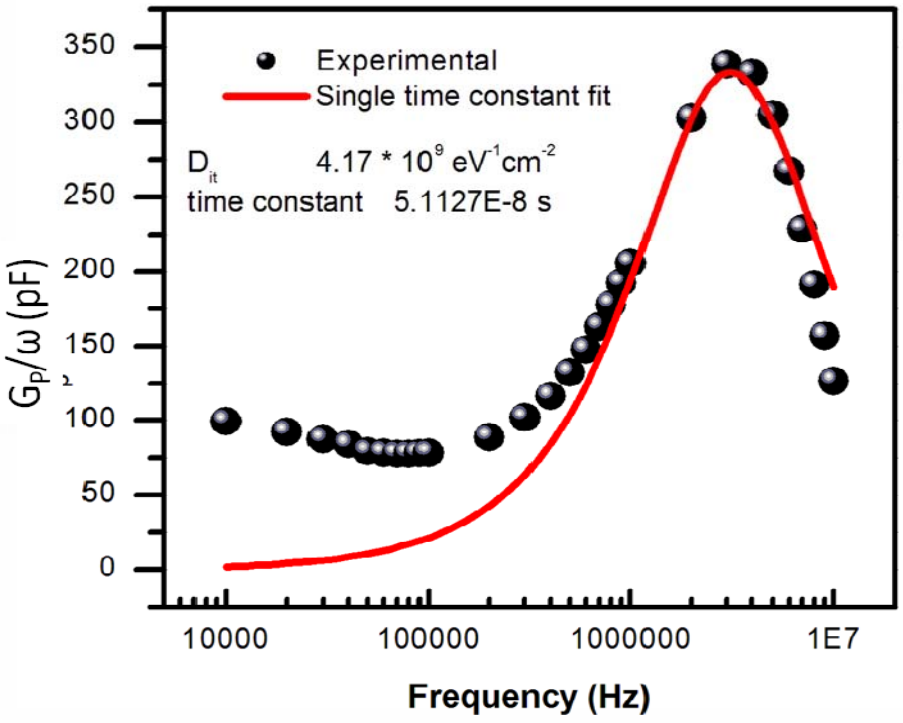

Figure 3.22 : Single time constant fit for G_P/ω (the loss factor) versus frequency for pBTTT/n-GaN hybrid diode.

The n-GaN/pBTTT devices show a shift from bulk capacitance to interface capacitance with frequency. A step in capacitance versus frequency curve, and a corresponding peak in conductivity versus frequency curve verify this shift. The n-GaN/P3HT devices do not show any such peak in conductivity. The shift from bulk to interface capacitance is visible but not very clear. Figure 3.23 shows capacitance and conductance versus frequency curve for n-GaN/P3HT devices.

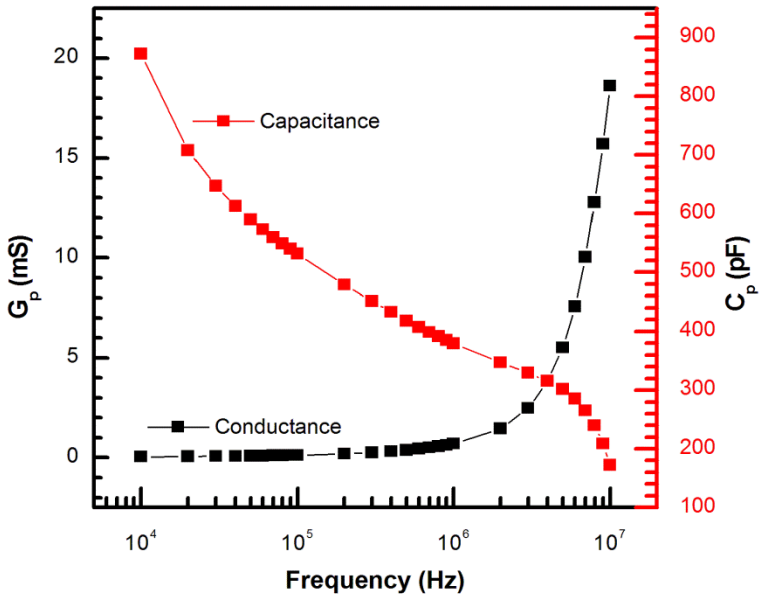

Figure 3.23 : Capacitance and conductance versus frequency curve for n-GaN/P3HT. As compared to n-GaN/pBTTT devices these devices do not show any peak in conductivity.

The interface trap density could not be calculated for n-GaN/P3HT devices as the model doesn't fits well to the G_P/ω versus frequency curve. Similarly the curves for N2200/n-GaN did not show any characteristic feature.

Thus it can be said that the capacitance – frequency measurement can give valuable information on the interface trap density, which is an important factor while looking at the transport of charge carriers, as these traps can act as the centers for carrier recombination and loss. The measured trap density for n-GaN/pBTTT diodes is not much as expected from the capacitance measurements, but a careful measurement with more sets of devices can give a better result.

3.2.4 Intensity Modulated Photocurrent Spectroscopy

This is a non steady state measurement, where modulated light from LED or laser is used to study the charge generation, transport and recombination mechanisms semiconductor devices. The technique has been widely used in studies of amorphous silicon solar cells [221,235] organic photovoltaic cell (OPV) [236,237,238] and dye synthesized solar cell (DSSC) [239,240,241] to understand the mechanisms of carrier life times, transit times and recombination dynamics. Modulated photocurrent measurement in absence of background illumination has been used to calculate trap state density [242,243]. Frequency and amplitude modulation techniques are useful for studying the charge transport dynamics. The IMPS technique has been used to understand the effect of different rate limiting steps on carrier transport. The experimental details have been mentioned in previous chapter. Different wavelength LED's were used for the modulated illumination measurement. To remove any frequency dependent characteristic feature of LED, the light sources were tested for average power and shape of waveform at different frequencies. Figure 3.24 shows average power of different wavelength LED's as a function of modulation frequency.

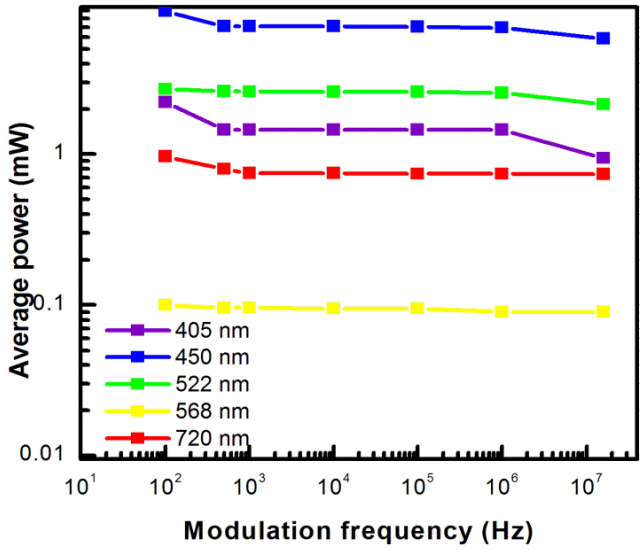

Figure 3.24 : Average power of different wavelength LED as a function of modulation frequency.

The photocurrent spectrum was measured only for n-GaN/pBTTT devices. The characteristic feature of photocurrent response from OI hybrid devices are listed below.

I) A different response for different illumination wavelengths, which can be differentiated in three categories.

1) n-GaN excitation wavelength, where the photocurrent I_{ph} (ω) shows no peak, the maxima is reached at very low frequency (ω~50 Hz). Photocurrent decays after this frequency and shows a peak at 10 KHz, which is characteristic to all λ.
2) Polymer excitation wavelength at energies higher as compared to absorption maxima of pBTTT. The I_{ph} (ω) an anomalous increase and decrease before reaching its peak value at ω_{max} = 10KHz, after which it decays sharply.
3) Polymer excitation wavelength at energies lower compared to absorption maxima, where the photocurrent is very less at lower frequencies, and increases rapidly at higher frequencies. A peak is observed at ω_{max} ~ 10 KHz and then the signal decays exponentially.

II) Magnitude of I_{ph} (ω) scales with modulated light intensity.

The response of the OI diodes for different modulation wavelength has been shown in figure 3.25.

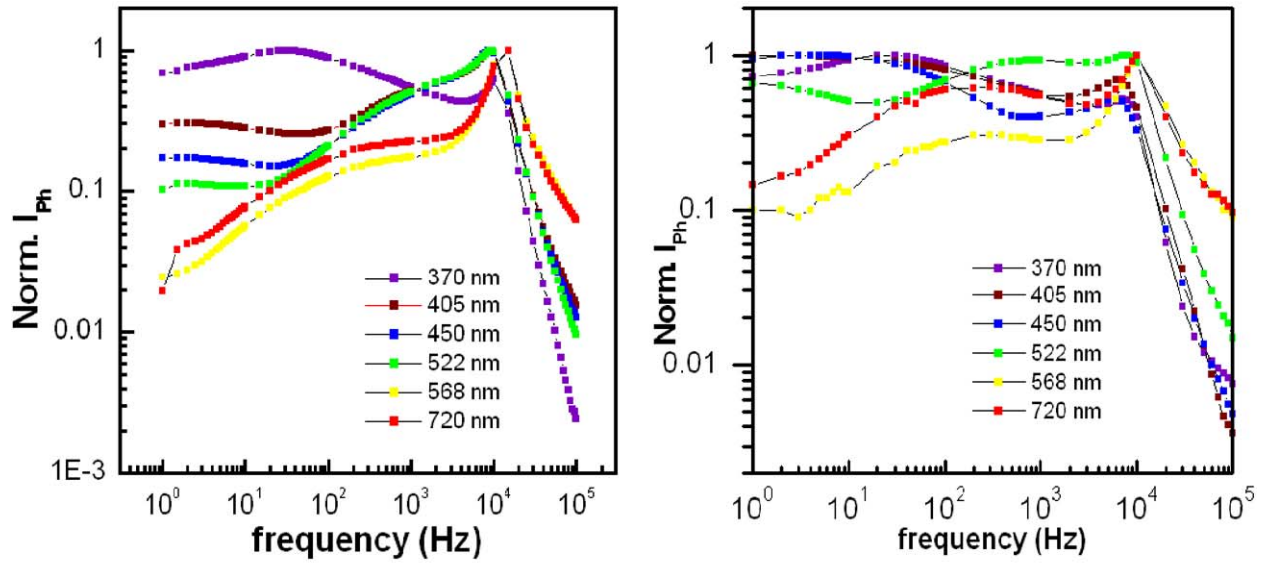

Figure 3.25 : IMPS response from two different devices measured at different wavelength at room temperature.

The characteristic peak frequency can arise because of the generation and recombination dynamics which plays role in device. The I_{ph} (ω) responses for these devices are close to pristine polymer sandwich between two electrodes. The dynamics which determine the peak position and peak width along with frequency variation of photocurrent can be simulated using circuit transfer function and microscopic transfer function.

3.3 Summary

Steady state measurements are useful to give basic device parameters which are important factors in determining the charge transport across the OI HJ interface. The basic device parameters like diode ideality factor, barrier height and defect state density was calculated using the I-V and C-V models. The hybrid device transport parameters have been summarized in the table below.

Table 3.1 : Summarized transport parameters for n-GaN/Polymer hybrid structure

Diode structure	n-GaN/pBTTT	n-GaN/P3HT	n-GaN/N2200/Al	n-GaN/N2200/Au
Ideality factor "n"	11.34 ± 0.02	2.258 ± 0.001	3.14 ± 0.03	2.40 ± 0.006
Space charge constant "B"	-	-	$0.0087 \pm 2 \times 10^{-4}$	$0.012 \pm 3 \times 10^{-3}$
Space charge exponent "m"	-	-	1.98 ± 0.08	1.28 ± 0.04
Barrier height Φ_B(eV)	0.60	0.85	-	-
Interface trap density D_{it} (eV^{-1} cm^{-2})	4.17×10^9	-	-	-

CHAPTER 4

SPECTRAL PHOTOCURRENT RESPONSE OF HYBRID PHOTODIODE STRUCTURE

4.1 Introduction

A spectral photocurrent response is governed by electronic structure, trapping and recombination kinetics, mobility and life time of charge carriers and the surface and interface state. Influence of these factors can be studies by varying the electrode material, thickness of the film and applying electric field [244,245]. The observed variation in responses as a function of illumination direction and electrode polarity can be attributed to bulk mobility of charge carriers, effect of polymer film thickness, Surface polarity dependent recombination kinetics, and excitonic states which are more likely to get differentiated at polymer – electrode interface. Spectral photoconductivity measurements have been useful in characterizing the efficiency limiting factors in organic BHJ solar cells, studying the trapping effects and measuring responsivity of photodetectors. I_{ph} (λ) is useful for identifying relative importance of different microscopic factors on the photogeneration. The photogeneration is given by the formula $J_{ph}(\lambda) = \alpha\theta I_0 \exp(-\alpha x)$, where α is the absorption coefficient, θ is the quantum efficiency of charge generation, and I_0 is the input photon flux. J_{ph} (λ) is normally expected to

resemble α (λ), this need not be the case for bilayer structures, where the J_{ph} (λ) depends on the direction of illumination and thickness of the sample.

In the present work we have studied the spectral photocurrent response of organic – inorganic (OI) hybrid heterojunction devices, as a function of different energy level alignments, applied field, background illumination, film thicknesses and direction of illumination. Striking differences in the measured photocurrent spectrum have been observed for OI diodes as a function of different parameters. Sizable spectral photocurrent response has been measured for the entire absorption range of the n-GaN/polymer hybrid diodes, where the spectral response of the device is much higher for n-GaN excitation wavelength as compared to polymer excitation. The overall quantum efficiencies are very low (< 1%) for all hybrid structures measured and an increase was observed with applied field.

The mechanism through which charges are photogenerated is different in inorganic semiconductor as compared to organic semiconductors. In an inorganic semiconductor the photo-excited electron-hole pairs are bound through coulomb interaction, where the force of interaction lowers the energy of electron-hole pair by an amount equal to exciton binding energy in the material. The value of this binding energy is very less in inorganic semiconductors (~ 30 meV), for GaN the free exciton binding energy is found to be 25.4 ± 0.9 meV [246] which is of the order of room temperature energy (25 meV). Thus the photo-excited charge pairs can be easily separated into free electrons and holes present in conduction band and valance band respectively. Thus, the carriers are generated in the bulk and at the interface of n-GaN without the requirement for any driving field for charge separation. In case of polymeric semiconductors the exciton binding energies are much higher (~ 0.2 – 1.0 eV) [43]. The energies required to separate an exciton into free negative and positive polaron cannot be provided by just the room temperature thermal energy. An extra field is required to break them into free negative and positive polaron, which is provided by the donor acceptor interface or a barrier layer; where the barrier can be created by an offset between donor and acceptor LUMO's or a workfunction mismatch between the semiconductor and metal electrode. In the present case the n-GaN/polymer semiconductor provides this barrier for exciton dissociation in the form of built in field or junction barrier.

The exciton generated in the interface and bulk region of polymer semiconductor diffuses towards the electrode and barrier layer. The excitons in polymer semiconductors have a diffusion length of ~ 5 – 10 nm [247,248]. Thus the excitons generated in the range of 5 -10 nm of barrier layer can only get dissociated into free negative and positive polarons; excitons generated in the bulk can either dissociated due to the presence of impurities or can recombine back radiatively or non radiatively. Thus it can be said that the n-GaN/polymer interface has a special role to play in the spectral photocurrent response of OI hybrid devices, where the density of photogenerated carriers is controlled by the interface area and its other properties. The impurities acting as trap states and defect states have an important role to play in the net photoconductivity and transport of photogenerated carriers. Once the carriers are photogenerated, the transport is governed by the band alignment and field conditions present at the interface and in the bulk of the active layer. The holes generated in n-GaN are transferred to p-type polymer active layer, while the electrons generated in polymer moves into the conduction band of n-GaN. The offset for electron transport for n-GaN/pBTTT and n-GaN/P3HT devices are very low (~ 0.1-0.2 eV) and is not enough for efficient electron transfer, as the role of back transfer in the transport becomes important with low offset energies.

In this section we will be looking at the spectral photocurrent response from hybrid n-GaN/polymer devices and effect of various parameters on the spectral response, which originates from various factors affecting the charge transport in the hybrid devices. Changes in spectral photocurrent response have been quantified and arguments have been presented in support for such observations. Studies have been performed with varying the polymer layer thickness, direction of illumination, background illumination and applied DC field. The type I and type II energy structures, as defined in chapter 3 (Figure 3.4 (a)), has a significant effect on spectral photocurrent response.

4.2 Measurement and Analysis

The spectral photocurrent response measurement of OI hybrid structures (n-GaN/pBTTT, n-GaN/P3HT and n-GaN/N2200) has been carried out using the experimental method and the calibration procedure described in spectral photocurrent response section of chapter 2. The illumination source used was a UV enhanced Xe lamp, coupled with SPEX 500 monochromator

(spectral range 0 – 1400 nm, 1 Å spectral resolution). The monochromatic light was focused using lens optics and chopped using mechanical chopper. The output of the device and detector were converted to voltage using I to V converter and measured using lock in amplifier (SR 830) simultaneously. External field (~ 10^5 V/cm) was applied using source meter; the data was collected by a computer using Labview.

4.2.1 n-Gallium Nitride/Polymer diode

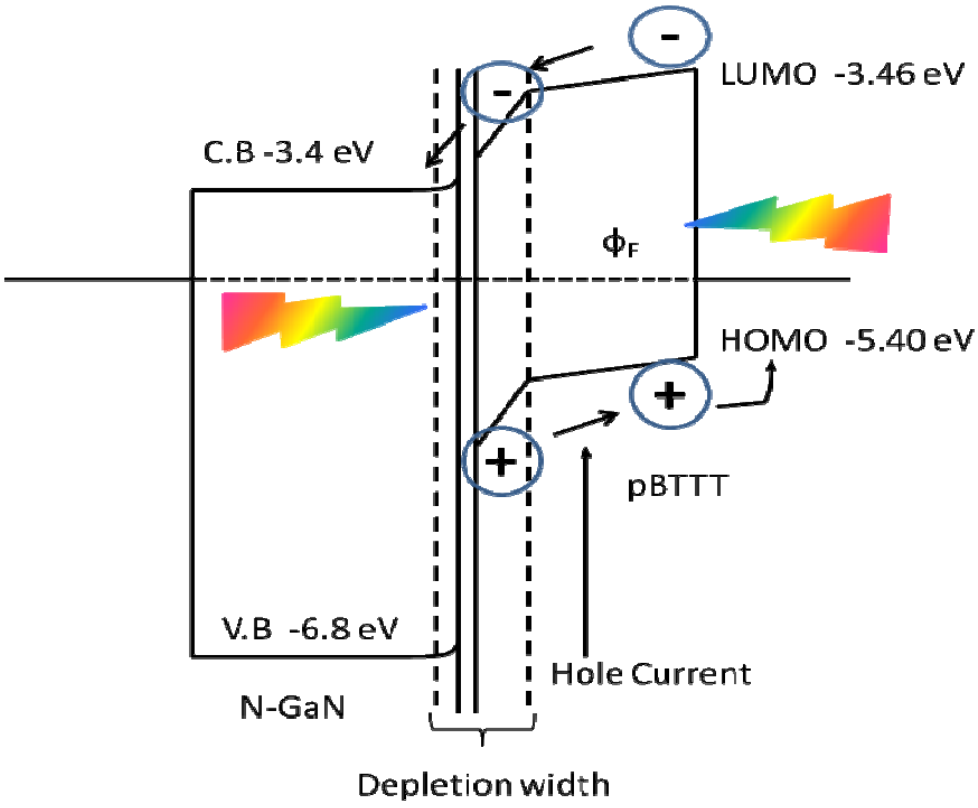

Figure 4.1 : An approximated band diagram showing additional field for hole transport and expected direction of hole current under zero bias.

The steady state and transient measurements for n-GaN/polymer OI diode system shows that they form a semiconductor-semiconductor heterojunction, with properties depending upon the energy level alignment. The current-voltage and capacitance-voltage measurements were used to extract various parameters, which can influence the transport of carriers under applied bias. Though these measurements were useful they cannot tell about the microscopic origin of efficiency limiting steps in OI devices, which are related to photoconductivity and transport of

carriers. The n-GaN/pBTTT hybrid diodes forms a type I energy structure where the holes transport from n-GaN to polymer is more favored compared to electrons transport from polymer to n-GaN. This is because of an extra driving force for hole current present between the HOMO of polymer and valance band maxima of n-GaN as shown in Figure 4.1. This is reflected in the increased responsivity of device in the n-GaN absorption region (370-400 nm). This can also be attributed to higher generation rate in n-GaN, but the transport in n-GaN is mostly diffusion dominated as there is no bulk field present because of the lateral electrode structure as shown in chapter 2 (Figure 2.16). This idea of carrier transport may not be completely valid as the lateral scan along the top electrode from far to near region of n-GaN/metal contact does not give any signature of n-GaN bulk resistance playing role in diffusive flow of carriers.

4.2.1.1 Illumination from n-GaN side

In this structure the photo illumination is carried from n-GaN side, which has 70% transmission for wavelengths > 400 nm as shown in chapter 2 (Figure 2.15). The device response for this illumination has been shown below for all three hybrid structures. This structure gives an advantage of protecting the polymer layer when exposed to wavelengths < 400 nm, i.e. UV illumination.

n-GaN/pBTTT diodes

The zero bias spectral photocurrent response (ΔJ_{Ph} (λ)) for n-GaN/pBTTT hybrid OI device for illumination from n-GaN side has been shown in figure 4.2. As can be inferred from the plot, the responsivity is 10 times higher for n-GaN absorption region (370 -400nm) as compared to polymer absorption region (400-650 nm). This can be a convoluted result of higher photo generated carrier density and better hole transport from n-GaN to pBTTT devices. A maximum EQE of 0.25% is measured and a responsivity of 0.30mA/cm^2 under zero applied bias. Photocurrent response from n-GaN shows a peak and decreases rapidly on the higher energy side as shown in figure 4.2 (a); this feature arises because of the undetectable emission from Xe lamp at wavelengths < 370 nm. The photocurrent edge is red shifted from the absorption edge of n-GaN, which may arise from the electron – electron interaction, but the exact reason is not understood as such a response is observed for disordered transport [249]. Whereas for pBTTT the photocurrent edge coincides with the absorption edge, such type of response has been cited as a

proof for semiconducting band model [250,251], which has been contradicted for photo excitation in many other polymers [252,253]. The spectral response from pBTTT shows a characteristic peak in the higher wavelength region, where the polymer absorption is less. Such a response can arise from the hole current generated from the electrode far from the illumination electrode. These responses where the photocurrent shows a peak at higher wavelength region, where the absorption is less, is called as an antibatic response [245], which arises when the direction of illumination and direction of field are antiparallel [254] . Figure 4.2 (b) shows intensity dependence of dc photocurrent, measured for n-GaN/pBTTT devices, where the average intensity at 20 Hz in half of the intensity under continuous illumination. The photocurrent from n-GaN/pBTTT hybrid devices scales with the incident power, this increase is almost linear as shown in chapter 3 (Figure 3.8).

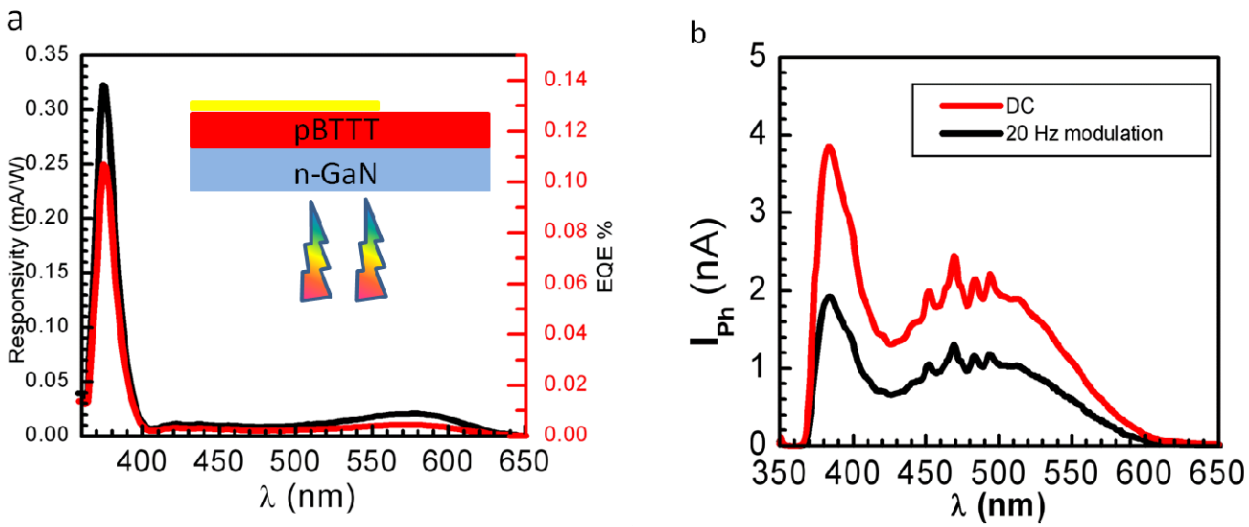

Figure 4.2 : a) Spectral photocurrent response from n-GaN/pBTTT device, A schematic of direction of illumination has been shown. b) The dc photocurrent measurement shows the intensity dependence of photocurrent.

n-GaN/P3HT

This device structure forms a perfect type I energy level alignment. The steady state current-voltage measurements show that this structure forms a better diode compared to n-GaN/pBTTT device. The spectral response and quantum efficiency plot measured for n-GaN/P3HT OI diodes has been shown in figure 4.3. The spectral response in very much similar

to n-GaN/pBTTT devices, a broad peak is observed in the lower energy region, which is also present in spectral response of pBTTT/n-GaN devices. The origin of such a peak is associated to hole current generated by absorption in lower wavelength range. This happens when the energy band alignment is such that the absorption maxima doesn't gives rise to significant hole current while the tail state absorption at the electrode far from illumination electrode can give a significant hole current (antibatic response) in donor polymer. This effect of decreased hole current at peak absorption wavelength is known as the internal filter effect [245] and is caused by the absorption of higher energy photon in the bulk and illuminated interface while the hole photocurrent is generated when the exciton generated by the higher wavelength photon, dissociates at the electrode far from the illumination electrode. Thus the responsivity increases in the tail absorption region giving rise to a peak in spectral response before going to zero.

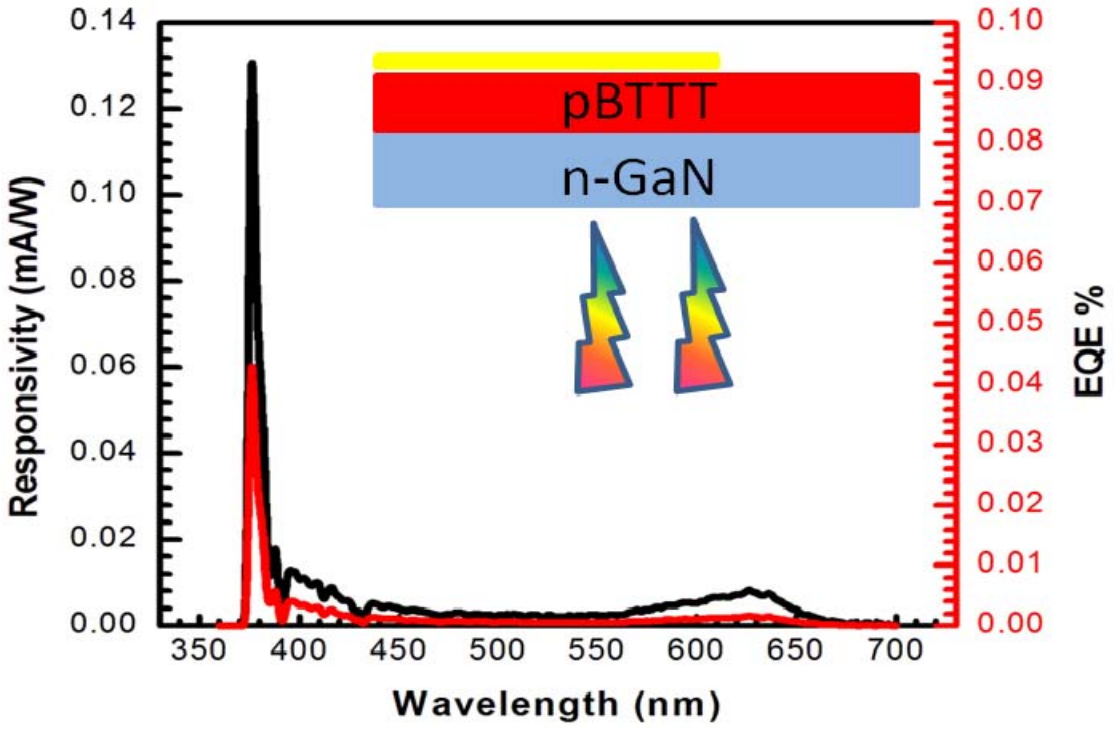

Figure 4.3 : Spectral responsivity and EQE % for n-GaN/P3HT device. Direction of illumination has been shown in the figure.

n-GaN/N2200 diode

The n-GaN/N2200 structure forms a type II energy structure; effect of such structure was clearly visible in the steady state dark and lights I-V. The spectral photocurrent response for n-GaN/N2200/Al structure show significant contribution from N2200. It is in contrast to what was measured in I-V, where the short circuit current was very less. In this case the maximum responsivity for polymer excitation, i.e. the peak in spectral response for N2200 excitation is around the same wavelength where the absorption shows a peak as shown in figure 4.4. The photocurrent response is little red shifted because of the interchain interaction which is higher in the film compared to in solution.

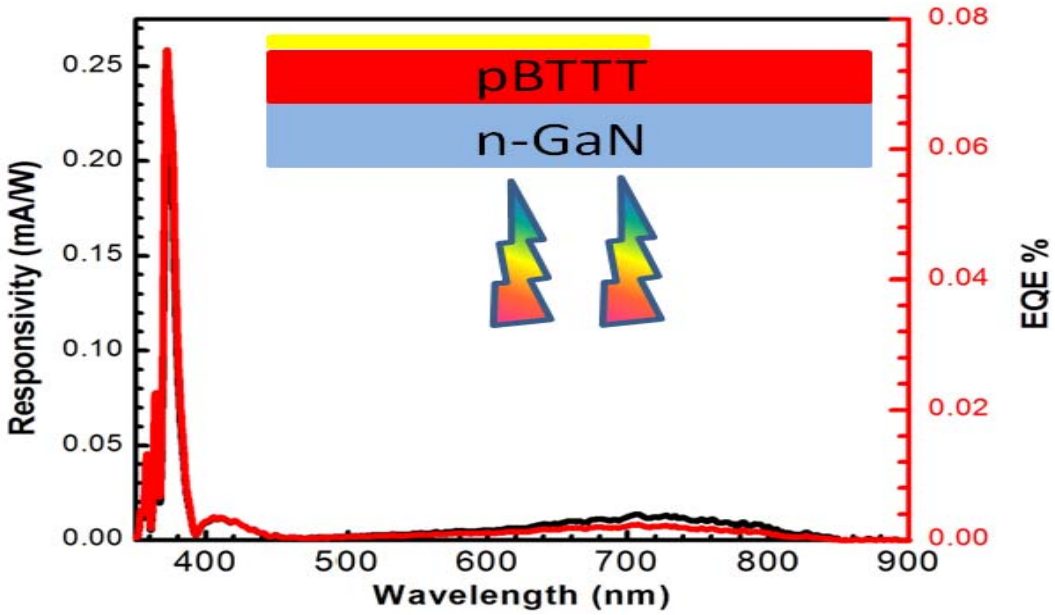

Figure 4.4 : Spectral response (black) and EQE (red) plot for n-GaN/N2200/Al devices, illumination from n-GaN side. Direction of illumination has been indicated.

The increased responsivity for n-GaN illumination (370-400 nm) in case of n-GaN/N2200/Al devices are yet not clear since N2200 cannot transport hole. The Characteristic peak observed in the tail states of absorption for p –type polymers are a direct result of energy band structure present in the bulk of the polymer semiconductors. Such response is not observed for n-GaN/N2200/Al hybrid devices.

It has been seen that the spectral response changes when the direction of illumination is reversed. The characteristic antibatic response in donor type polymer heterostructure changes to

symbatic response, where the spectral photocurrent follows the absorption trend. Spectral response for top electrode illumination is presented in next section.

4.2.1.2 Illumination from top electrode

Top electrode illumination gives completely different results as compared to when devices are illuminated from n-GaN side. The characteristic peak present in the absorption tail, when illuminated from n-GaN side is not present when illuminating from the top electrode. The photocurrent spectral response follows the absorption spectrum and is highest at the wavelength where absorption curve peaks. Since this top illumination exposes the polymer for UV radiation, thus the response from n-GaN was not measured for top electrode illumination. A thin layer (~ 10 -15 nm) of gold was used as top electrode for this measurement.

n-GaN/pBTTT diode

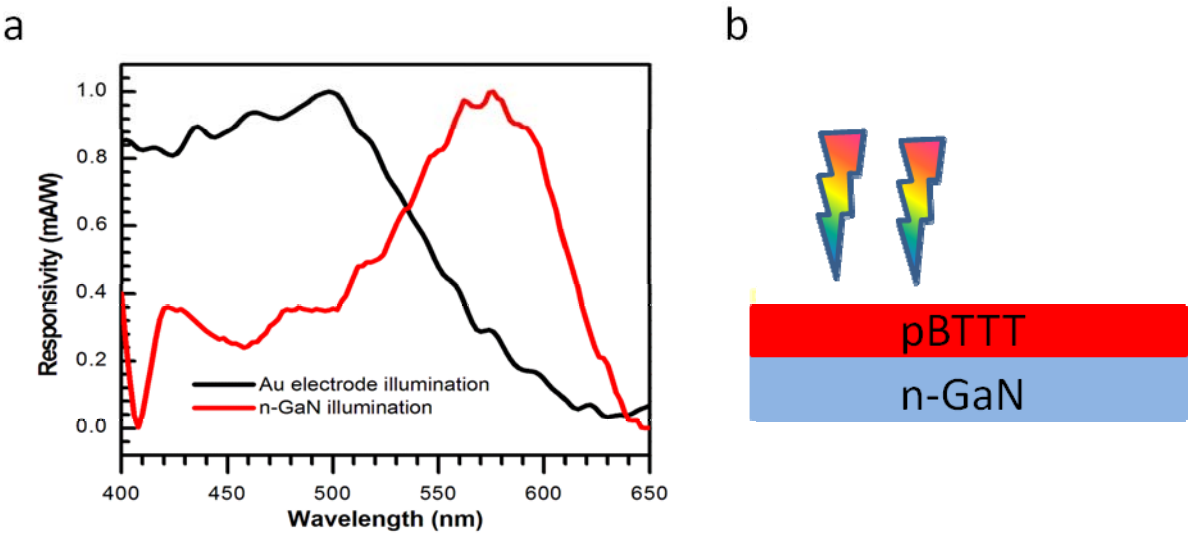

Figure 4.5 : a) Normalized Responsivity for illumination from top (Au) electrode (black) and bottom n-GaN (red), b) schematics of direction of illumination.

When illuminating from the top electrode side, it is observed that the photocurrent response follows the absorption trend; such type of response is known as symbatic response [245]. This response is observed when the direction of illumination is parallel to the direction of field present in the bulk of the semiconductor. The maximum in photocurrent response is observed around the same wavelength at which the absorption shows a peak. This nature of photocurrent

response can be understood by the fact that the hole current in the device is now because of the exciton dissociation near the illumination electrode, i.e. the absorption close to illumination edge is giving rise to hole current while the absorption at the interface far from the illumination electrode is not giving rise to any photocurrent. This argument is supported by the fact that there is no peak in the tail region of absorption. This argument can also be verified by the response, when illumination from n-GaN side, where, hole current generated by absorption at higher wavelength at far electrode gives peak in photocurrent response, while the photo excitation at near electrode doesn't contribute to photocurrent. Figure 4.5 shows response for illumination from top Au electrode. Normalized Responsivity from n-GaN side illumination has also been included for comparison if. The responsivity has been normalized to respective maximum values for a clear picture of change in spectral photocurrent response with illumination direction.

A peak in tail state of absorption (550 – 650 nm), when illuminated from n-GaN side is a clear signature of antibatic response, no such peak was observed for illumination from top electrode side. The difference in the spectral photocurrent response for illumination from n-GaN and Au sides suggests that, the energy band alignment in polymer is such that the hole current flows from gold electrode towards n-GaN/polymer interface. This is contrary to the response expected from the energy band diagram shown in Figure 4.1, where the hole current should flow from n-GaN/pBTTT interface to Au/pBTTT interface.

Origin of such spectral photocurrent response under zero external bias is n-GaN/pBTTT OI hybrid devices is not clear. The photocurrent spectrum suggests an opposite direction of band bending which is not obvious from the basic band bending concept applied for the semiconductor-semiconductor heterojunction systems. Further analysis will be required to completely understand the reversed nature of photocurrent spectrum and the associated band bending which give rise to such response.

n-GaN/P3HT diode

Spectral photocurrent response measured for top electrode illumination in n-GaN/P3HT systems show a similar trend in photocurrent response, as measured in the case of n-GaN/pBTTT. Thus the small shift in energy structure does not affect the bulk band structure

much; Figure 4.6 shows spectral photocurrent response from n-GaN/P3HT devices, for top illumination. Photocurrent response for bottom n-GaN illumination has also been included for comparison. The responses are normalized with respect to their maximum for a better comparison.

The difference in spectral response with illumination from 2 different sides is much more distinct for n-GaN/P3HT as compared to n-GaN/pBTTT. The FWHM of photocurrent peak is less for n-GaN/P3HT which is an example of strong internal filter effect present in P3HT donors. But the observed spectral response in opposite to what is expected, which is consistent with what was observed in spectral response of n-GaN/pBTTT hybrid system.

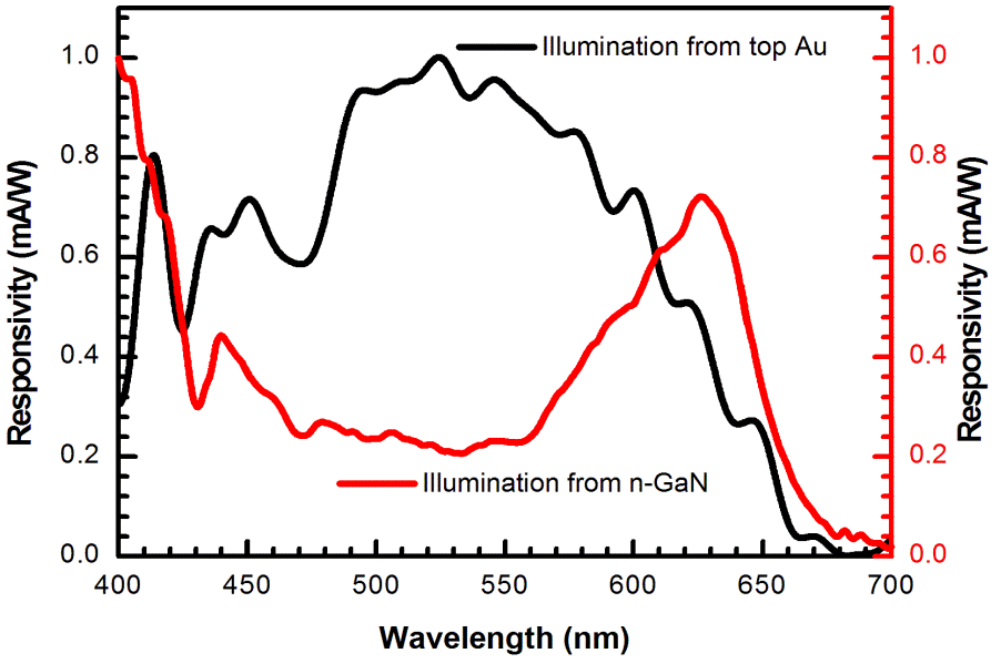

Figure 4.6 : Normalized Responsivity for illumination from top Au electrode (black) and bottom n-GaN/polymer interface (red).

Detailed analysis is required to understand the reversed nature of spectral photocurrent response from the expected response, under zero bias condition, which is consistent for both the donor polymer/n-GaN hybrid structures. As will be seen in the next section, with the application

of external field the energy band structure changes and corresponding spectral photocurrent response is different under different bias conditions.

4.3 Effect of different control parameters on spectral photocurrent response

The spectral photocurrent responses as measured for the zero biased devices with no external perturbation to the systems were shown in previous sections. An understanding of the role of external control parameters in modulating the energy band diagram, and charge condition, is important for understanding the mechanism of physical processes taking place in OI hybrid devices. Spectral responses under applied reverse field are generally used for estimating the efficiency limiting factors in BHJ and dye sensitized solar cells. Here we have varied the applied external field condition, donor polymer film thickness and background light flux to probe the effects of such perturbations on the transport of carriers in OI hybrid systems.

4.3.1 Effect of Electrical Bias

The energy band structure present in the bulk of polymer is sensitive to the applied external field. The band structure shifts up or down depending upon the direction of the applied field. In certain extreme cases it can also cause inversion of the band structure. In case of photoconductivity measurements, under applied reverse field, the device works in photo conducting mode. Under this condition the spectral response and the quantum efficiency for photon to charge conversion increases. Here we have measured spectral photo current response as a function of applied forward and reverse bias. A sizable change in spectral photocurrent response has been observed as a function of applied field direction. Figure 4.7 shows the spectral photocurrent response from n-GaN/pBTTT OI hybrid devices. The shift from one type of response to other is clearly visible under applied reverse bias, which suggests the change in energy band structure with applied bias. Figure 4.7 (a) shows the response from n-GaN part, the response from n-GaN side is in agreement with the argument that the spectral photocurrent response should increase with increase in applied reverse bias. Figure 4.7 (b) shows the spectral response from donor pBTTT part. The change in the spectral response of pBTTT occurs with gradual increase in bias. This suggests that the shift from one type of response to another type is not instantaneous but gradual changes with increasing bias. The response has been decoupled for having a clear picture.

While the response under forward bias, as shown in Figure 4.8, is similar in shape to the spectral response under zero biased state, except that the spectral responsivity increases with increasing field. This observation suggests that the zero biased energy band structure doesn't changes it's form but gets more enhanced under forward bias. Thus it can be speculated that the zero biased and the forward biased energy band structures are similar.

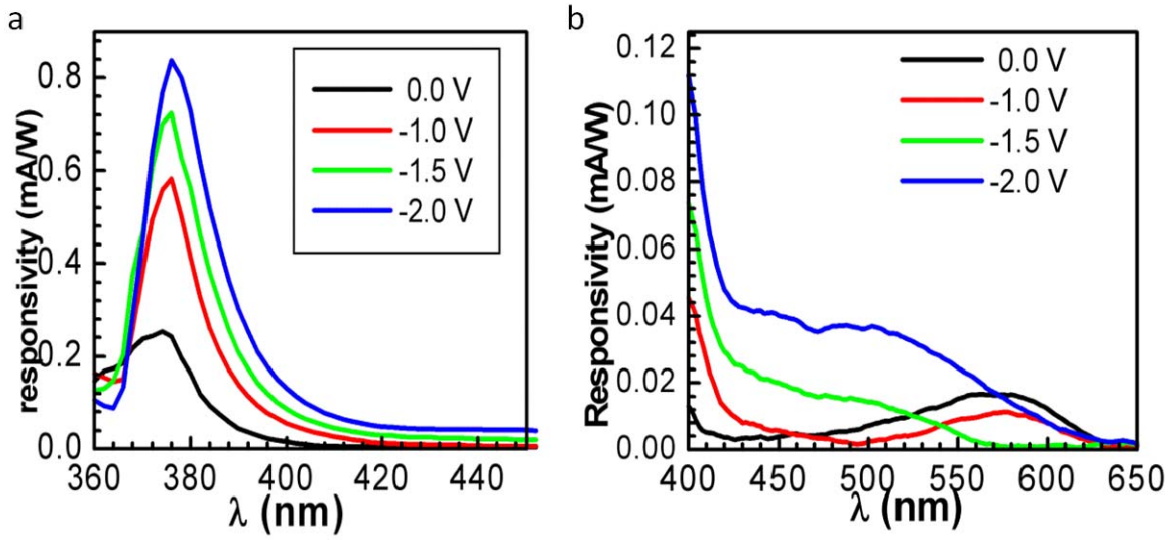

Figure 4.7: Spectral photocurrent response a) n-GaN, b) pBTTT under applied reverse bias, direction of illumination is from n-GaN side.

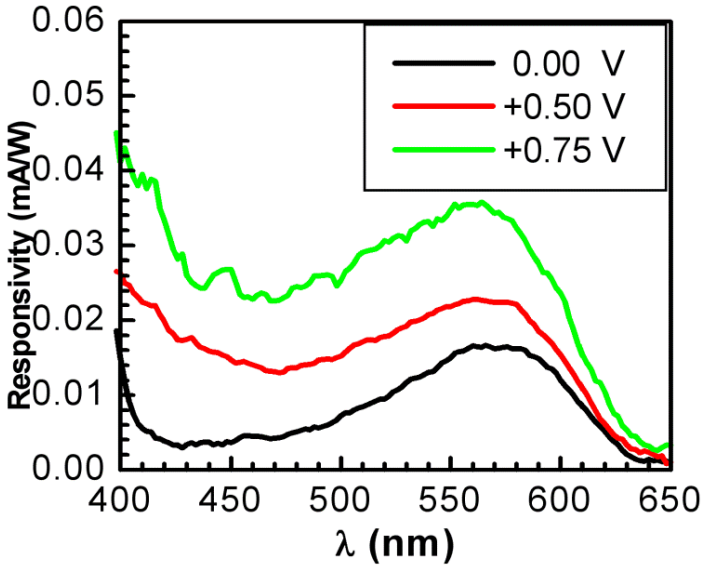

Figure 4.8 : The forward biased spectral photocurrent response from n-GaN/pBTTT devices, illumination from n-GaN side.

A further comparison has been shown in figure 4.9 between the spectral responses measured under forward and reverse fields in n-GaN/pBTTT hybrid system, the symbatic and antibatic responses are clearly visible for illumination from n-GaN in Figure 4.9 (a), and illumination from top electrode in Figure 4.9 (b).

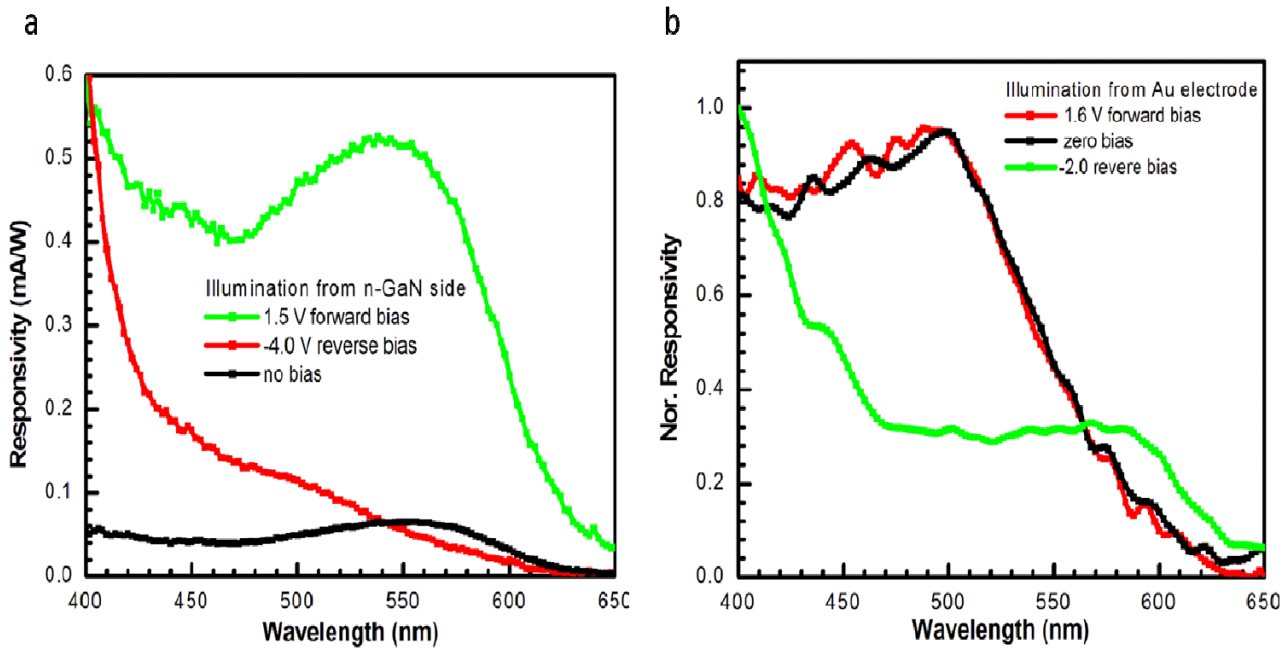

Figure 4.9 : Spectral photocurrent response from n-GaN/pBTTT OI hybrid devices, a) illumination from n-GaN and b) illumination from gold electrode, under forward and reverse biased conditions.

The basic underlying reason for two different spectral responses is same as mentioned in case of zero biased symbatic and antibatic response. The change in energy band structure from one state to another causes the change in direction of hole current in the hybrid diode, giving rise to two different response. This type of variation in response with direction of applied field has been reported for many polymer semiconductors diodes [244,245,255,256]. Theoretical models explain the origin of such spectral photocurrent response [257,258,259,260] using the different boundary conditions and generation, transport and recombination kinetics. The models used for

simulating the spectral photocurrent response for inorganic as well as organic polymeric semiconductors have been highlighted in chapter 5.

4.2.2 Thickness dependence of spectral photocurrent

The effect of change in the thickness of semiconductor layer can be seen as a change in the magnitude of internal filter effect i.e. the peak in the spectral photocurrent response, observed in the absorption tail is more distinct. The symbatic response remains undisturbed by the increase in thickness, apart from the effects caused by film thickness on charge transport. Thickness dependence was measured for n-GaN/P3HT devices, the response for thinner films (~ 90 nm) show increased antibatic response, which is because of the enhanced internal filter effect. Similar responses are expected from n-GaN/pBTTT devices. Figure 4.10 show thickness dependent antibatic response from n-GaN/P3HT devices for two different film thicknesses (90 nm and 130 nm).

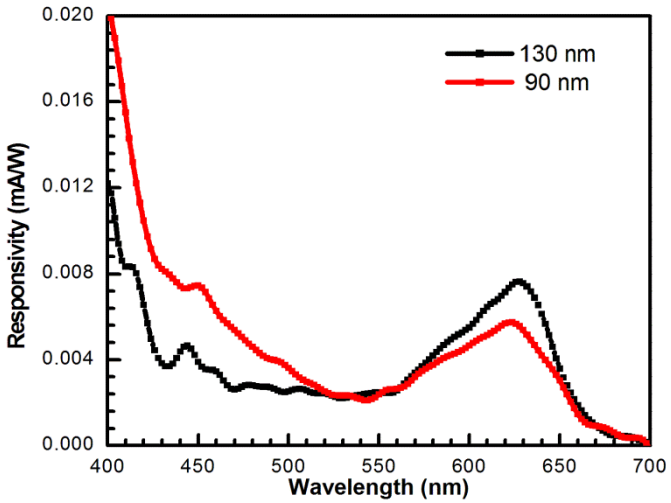

Figure 4.10 : Spectral response from n-GaN/P3HT devices for 130 nm and 90 nm P3HT films.

4.2.3 Background illumination dependence

The effect of illumination on a photodiode is an increased conductivity due to the increase in the free carrier density in the bulk. The photogenerated charge density can have a significant effect on trapping and recombination kinetics of the carriers. In chapter 3 it has been shown that the intensity dependence of J_{sc} can be a useful tool to look into the recombination mechanisms. The background CW illumination can have a significant effect in the

photoconductivity measurement. The charges generated by background illumination can fill the trap states and allow a trap free path for carriers generated through the modulated light. Oppositely, they can also enhance the recombination events causing a net decrease in carrier density reaching the collection electrodes. In Figure 4.11 spectral responses in presence of background CW illumination of different intensity has been shown. The responsivity in n-GaN increases with intensity of CW illumination as shown in Figure 4.11 (a), while the characteristic peak present at 580 nm in the spectral response of donor polymer decreases with increasing background illumination intensity, as shown in Figure 4.11 (b).

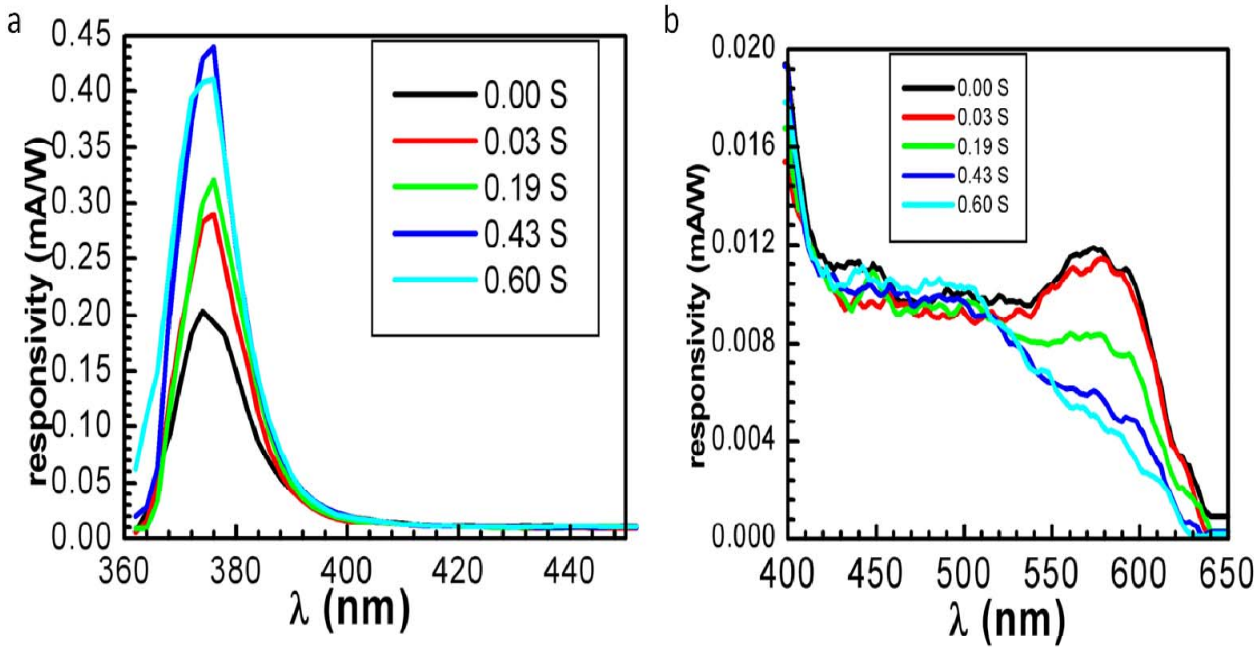

Figure 4.11 : Spectral photocurrent response from n-GaN/pBTTT devices in the presence of background illumination a) response from n-GaN, b) response from pBTTT.

Increase in n-GaN response can be because of the lateral transport in n-GaN which offers less recombination for carriers, while the hole transport in polymer is enhanced because of the filling up of trap states in the presence of continuous background illumination. Decrease in the characteristic peak in the spectral response of the pBTTT arises from the fact that the hole current generated at the electrode far from the illumination electrode can undergo recombination near the Au electrode. As this should be visible in both the responses, it is seen only in pBTTT response while n-GaN response does not show any such decrease. Hence there have to be other

factors involved in deciding the spectral response of the device in presence of background illumination apart from the recombination effect.

4.4 Summary

It is clear from the results of spectral photocurrent response that the photoconductivity in an OI hybrid system is dependent on many physical factors. The effect of band bending, Type of energy structure, application of electrical bias, thickness of the active semiconducting layer and the background illumination has significant effect on the spectral photocurrent response. The control parameters studied are related with some physical process and show the effect of that process on charge transport in bulk and at the interface. Though all the results mentioned here are not completely understood, but a basic understanding about photogenerated charge transport in the OI system can be developed. Understanding the energy band structure is important for explaining the reversed nature of zero biased spectral photocurrent response from the n-GaN/donor polymer OI hybrid interface. A detailed analysis will be required to sketch a complete picture of physical processes controlling the charge transport in the bulk and interface of the OI hybrid structures.

CHAPTER 5

MODELING SPECTRAL PHOTOCURRENT RESPONSE

5.1 Introduction

Photocurrent action spectrum or spectral photocurrent response is a useful tool for studying the bulk and interface of photodiodes and solar cells. The applicability of this experiment in quantifying the efficiency limiting processes and external quantum efficiency for solar cells and photodetectors is well established [245,261,262]. The photocurrent spectral response may depend on many fundamental processes occurring inside the semiconductor, which includes generation of charge carriers, transport, trapping, recombination, and collection on the edge electrodes. Each step is an efficiency determining process and has a significant effect on the spectral response. In a BHJ structure the requirement for an electron and a hole collecting contact is an important factor for higher efficiency [263]. In single layer pristine polymer system, like ITO/MEH PPV/Top electrode, the nature of top electrode determines the spectral photocurrent response; this is derived from the fact that a barrier electrode is required for exciton dissociation and electron collection from MEH PPV [245].

In a bilayer type device structure where the exciton dissociation occurs at the interface between the active layers, the interface property decides the generation rate of free carriers or the charge polarons. The transport through the bulk is subjected to the bulk recombination mechanisms and trap density [264]. The charge collection efficiency of an electrode depends on the work function of the metal electrode and relative energies of semiconductor [265]. To understand the fundamental process giving rise to the spectral photocurrent response in a device

structure, modeling of device response in terms of carrier generation, transport and recombination losses are essential. Many models have been proposed for simulating the spectral photocurrent response for semiconductor devices [257,258,259,260,266] of which the model of DeVore is few of the earliest models. The model proposed by Ghosh et.al. [258] assumes a two step energy structure namely barrier and bulk region. The photo generation of carriers in the bulk and barrier is assumed to be uniform but they differ in their collection efficiency of charges. The model is able to generate the characteristic symbatic and antibatic responses observed in the spectral photocurrent response. The model developed by DeVore considered the effects of carrier diffusion and recombination effects [257], Exciton diffusion has been considered by the model of Desormeaux, and Ghosh and Feng [260,266] and dissociation at the barrier electrodes and surface recombination's. These models have been used for simulating the photocurrent spectral response in many polymeric semiconductor device structures [244,245,267].

The spectral photocurrent response for organic – inorganic heterojunction (OJ HJ) hybrid semiconductor heterostructures of n-GaN/Polymer was shown in chapter 4. The spectral photocurrent response can be modeled using these basic generation, transport and recombination models for semiconductors. Since these models generally consider the basic mechanism of carrier transport, the model needs to be modified in the presence of external fields, and interface trap states. In this chapter a detailed description of the models will be presented

5.2 Device Modeling

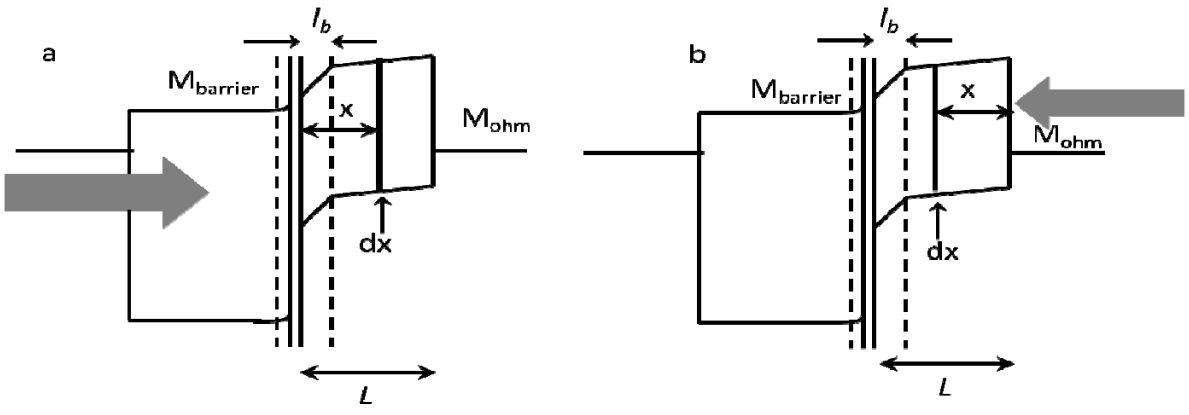

Figure 5.1 : Schematic representation of OI HJ semiconductor diode with bulk and barrier layer band diagram. a) Light illumination from ohmic and b) barrier electrode.

A very simple model can be assumed for simulating the spectral response of photocurrent in OI devices. Since the OI devices consist of two layers of semiconductors of completely different properties, the model developed will require a consideration of such structure. The model will be developed assuming band transport of charge carriers, where in the molecular semiconductor properties will be introduced later. The model assumes a bilayer structure of OI HJ semiconductor with ohmic electrode on both the ends. Figure 5.1 shows a schematic diagram of the model semiconductor diode assumed for the modeling the device response. The structure is a combination of organic and inorganic semiconductor, where the organic layer thickness is L. Thickness of the barrier layer is l_b, the inorganic side of the system can be treated as a barrier electrode for organic semiconductor in this derivation. We will consider the spectral response of organic semiconductor; the model can be easily extended for spectral response of inorganic material.

We assume a single organic semiconductor layer between metal electrode M_{ohm}, which forms ohmic interface with organic semiconductor and inorganic semiconductor $M_{barrier}$, which forms barrier junction with organic semiconductor. Because of the formation of barrier layer in vicinity of $M_{barrier}$, the CB and VB bend sharply inside the barrier region of width l_b. Effect of band bending is less in the bulk region, which is defined as the region between the electrode M_{ohm} and barrier layer l_b. Let us assume that the total length of the organic semiconductor layer is equal to L, where l_b is the width of the barrier layer. Either ohmic or barrier electrode can be assumed to be at $x = 0$, depending upon the direction of illumination. When the light of incident, a photon flux of density I_0 is illuminated on the electrode at $x = 0$, the charge carrier generated in the bulk will be proportional to the intensity of incident light at x. The rate of generation of carrier at x is given by [258],

$$\frac{dn_{photo}(x)}{dt} = \varphi I_0 \alpha(\epsilon) exp(-\alpha(\epsilon)x) \tag{5.1}$$

In equation 5.1, $\alpha(\epsilon)$ is the absorption coefficient of the semiconducting layer, as a function of photon energy (ϵ), φ represents the quantum efficiency of charge generation by light in the semiconductor layer. The photogenerated charge carrier density at a position x is given by $n_{photo}(x)$.

The photogenerated carriers can diffuse or drift through the bulk or recombine at the trap sites. Thus, the rate of change of charge carrier density at *x* is determined by the rate of generation, rate of carrier transport via drift, under an applied field E, or diffusion, under a carrier gradient dn_{photo}/dx, and the rate of recombination proportional to total charge carrier density. In this model the equilibrium carrier density is assumed to be negligible compared to photogenerated carrier density. Effect of bulk equilibrium density on transport and recombination mechanisms can be added as a correction to the charge density later. The net rate change of photogenerated carrier in the bulk is given by,

$$\frac{dn_{photo}(x)}{dt} = \varphi I_0 \alpha \exp(-\alpha x) - \frac{di_{diff}}{dx} - \frac{di_{drift}}{dx} - \frac{n_{photo}}{\tau} \qquad (5.2)$$

In equation 5.2, n_{photo} is the carrier density which can be density of either electron or hole, α = $\alpha(\epsilon)$, μ is the bulk mobility of the photogenerated carrier and τ is the bulk recombination lifetime, i_{diff} is the diffusion current, and E is the applied field across the electrode. Under the equilibrium condition, the net charge flowing through *x* in the bulk is zero, giving $\frac{dn_{photo}(x)}{dt} = 0$. The diffusion current i_{diff} can be given by $i_{diff} = -D_n \, {dn_{photo}}/{dx}$ where D_n is the carrier diffusion constant, expression for i_{drift} is given by $i_{drift} = n\mu E$. Substituting E = V/x and expression for diffusion and drift current in equation 5.2, and assuming no spatial distribution of D_n and μ, gives a time independent differential equation, for steady state distribution of carrier density in the bulk, which is given by,

$$\frac{d^2 n_{photo}(x)}{dx^2} - \frac{dn_{photo}(x)}{dx}\left(\frac{\mu V}{xD_n}\right) = \frac{n_{photo}(x)}{D_n}\left(-\frac{\mu V}{x^2} + \frac{1}{\tau}\right) - \frac{\varphi I_0 \alpha}{D_n} exp(-\alpha x) \qquad (5.3)$$

This is a drift-cum-diffusion relation between generation, transport and recombination rates. This equation can be applied to only free carriers, under applied external field, present in the semiconductor material. The equation changes to diffusion equation in the absence of external applied field, this equation can be applied to free charge carriers under the absence of field and also to exciton diffusion in the organic semiconductor bulk. The diffusion equation for excitons is given by [257,260,266],

$$\frac{d^2n'(x)}{dx^2} = \frac{n'}{D'\tau'} - \frac{\varphi I_0 \alpha}{D'} exp(-\alpha x) \tag{5.4}$$

In equation 5.4, $n'(x)$ represents the exciton density. This equation has been mentioned by Ghosh and Feng and Desormeaux, max, and Leblanc. The exciton diffusion length is given by $L'_D = \sqrt{D'\tau'}$. A general solution for equation 5.3 can be given as,

$$\begin{aligned} n_{photo}(x) = x^{\left(\frac{1}{2}+\frac{\mu V}{2D}\right)} \Bigg\{ & BesselJ\left[\left(\frac{1}{2}-\frac{\mu V}{2D}\right), \frac{-ix}{L_D}\right] B + BesselY\left[\left(\frac{1}{2}-\frac{\mu V}{2D}\right), \frac{-ix}{L_D}\right] C \\ & + BesselJ\left[\left(\frac{1}{2}-\frac{\mu V}{2D}\right), \frac{-ix}{L_D}\right] \int_1^x \frac{\varphi I_{0\alpha}}{D}, exp(-\alpha x_1).\pi.x_1^{\left(\frac{1}{2}-\frac{\mu V}{2D}\right)} BesselY\left[\left(\frac{1}{2}-\frac{\mu V}{2D}\right), \frac{-ix}{L_D}\right] dx_1 \\ & - BesselY\left[\left(\frac{1}{2}\right.\right. \\ & \left.\left. -\frac{\mu V}{2D}\right), \frac{-ix}{L_D}\right] \int_1^x \frac{\varphi I_{0\alpha}}{D}, exp(-\alpha x_2).\pi.x_2^{\left(\frac{1}{2}-\frac{\mu V}{2D}\right)} BesselJ\left[\left(\frac{1}{2}-\frac{\mu V}{2D}\right), \frac{-ix}{L_D}\right] dx_2 \Bigg\} \end{aligned} \tag{5.5}$$

Using $\Gamma = \left(\frac{1}{2}+\frac{\mu V}{2D}\right)$, $\Delta = \left(\frac{1}{2}-\frac{\mu V}{2D}\right)$, and $A = \frac{\varphi I_{0\alpha}}{D}$, equation (5.5) can be written as,

$$\begin{aligned} & n_{photo}(x) \\ & = x^{\Gamma} \Bigg\{ BesselJ\left[\Delta, \frac{-ix}{L_D}\right] B + BesselY\left[\Delta, \frac{-ix}{L_D}\right] C \\ & + BesselJ\left[\Delta, \frac{-ix}{L_D}\right] \int_1^x Aexp(-\alpha x_1).\pi.x_1^{\Delta} BesselY\left[\Delta, \frac{-ix}{L_D}\right] dx_1 \\ & - BesselY\left[\Delta, \frac{-ix}{L_D}\right] \int_1^x Aexp(-\alpha x_2).\pi.x_2^{\Delta} BesselJ\left[\Delta, \frac{-ix}{L_D}\right] dx_2 \Bigg\} \end{aligned} \tag{5.6}$$

In equation 5.5, B and C are constants and L_D is the carrier diffusion length. For the case of exciton the solution of diffusion equation is given by [245],

$$n'(x) = B'exp\left\{-\frac{1}{L'_D}x\right\} + C'exp\left\{\frac{1}{L'_D}x\right\} + \frac{\theta I_0 \alpha exp(-\alpha x)}{D'\left(\frac{1}{L'^2_D} - \alpha^2\right)} \tag{5.7}$$

In equation 5.7, D' is the diffusion coefficient of exciton, this expression can also be used for free carriers when no external bias is applied, in that case n'(x) represents free carrier density. From the considerations of Devore model [257] which assumed direct generation of free electron and holes. The recombination of charge carriers can take place in the bulk after mean life time τ, or at any surface at a rate which is represented by a recombination current $i_R = n_s S$. Where, $n_{S\ photo}$ is

the density of electron hole pair and S is the surface recombination velocity. When film thickness is comparable to the reciprocal of the maximum value of absorption coefficient, a high surface recombination rate $S > D_n/L_{Dn}$ (bulk recombination rate) results in an antibatic response [245], while a low recombination rate gives symbatic response. The boundary conditions for surface recombination at illuminated surface for zero external bias case can be given by [257],

$$(i_R)_0 = -D_n \left({dn_{photo}}/{dx} \right)_{x=0} = -n_{0_{photo}} S \tag{5.8}$$

Boundary condition for surface far from the illuminated surface is given by,

$$(i_R)_L = -D_n \left({dn_{photo}}/{dx} \right)_{x=L} = -n_{L_{photo}} S \tag{5.9}$$

Under these boundary conditions the coefficients B' and C' can be calculated as [245,257],

$$B' = \frac{\varphi I_0 \, {\alpha}/{D_n}}{(\beta^2 - \alpha^2)} \left\{ \frac{(S - D_n\alpha)(D_n\beta - S)exp(-\alpha L) + (S + \alpha D_n)(S + \beta D_n)exp(\beta L)}{(D_n\beta - S)^2 exp(-\beta L) - (D_n\beta + S)^2 exp(\beta L)} \right\} \tag{5.10}$$

And

$$C' = \frac{\varphi I_0 \, {\alpha}/{D_n}}{(\beta^2 - \alpha^2)} \left\{ \frac{(S - D_n\alpha)(D_n\beta + S)exp(-\alpha L) + (S + \alpha D_n)(D_n\beta - S)exp(-\beta L)}{(D_n\beta - S)^2 exp(-\beta L) - (D_n\beta + S)^2 exp(\beta L)} \right\} \tag{5.11}$$

In equation 5.10 and 5.11, $\beta = 1/L_D$, the inverse of carrier diffusion length.

The increase in conductivity because of photo excitation is proportional to the total number of carrier pairs which for Sandwich cell geometry is given by [245],

$$J_{ph} \propto \frac{1}{\int \left({1}/{n_{photo}} \right) dx} \tag{5.12}$$

And corresponding photoconductivity is given by [245]

$$\sigma_{ph}(\alpha) \propto \frac{1}{\int_0^L \frac{1}{n_{photo}(\alpha, x)}\, dx} \tag{5.13}$$

The equations 5.12 and 5.13 derived above are valid only for free carriers. Considering OI system with an organic and inorganic layer, the charge generation in the organic side depends on the exciton diffusion to the barrier electrode. Under this case a pure diffusion equation given by equation 5.4 is valid. The general solution to such an equation is given by equation 5.7. Under the boundary condition of $n' = 0$ at $x = 0$ [260], i.e. the exciton density goes to zero at the electrode $x = 0$. The exciton density is given by [245,260],

$$n' = \frac{\alpha\varphi I_0}{\beta'^2 - \alpha^2}\left[\left(\frac{\exp(\beta' L) - \exp(-\alpha L)}{\exp(-\beta' L) - \exp(\beta' L)}\right)\exp(-\beta' x) - \left(\frac{\exp(\beta' L) - \exp(-\alpha L)}{\exp(-\beta' L) - \exp(\beta' L)}\right)\exp(\beta' x) + \exp(-\alpha x)\right] \tag{5.14}$$

In equation 5.14, $\beta' = \frac{1}{L_D'}$, this model of exciton diffusion was introduced by Ghosh and Feng [260]. The photocurrent is proportional to the gradient of exciton density at the barrier layer. For illumination from the side of barrier layer, the photocurrent gives symbatic response [245,260].

$$J_{Barrier} = -D'\left(\frac{dn'(x)}{dx}\right)_{x=0} \tag{5.15}$$

$$J_{Barrier} = \frac{\alpha\varphi I_0 D'}{\beta'^2 - \alpha^2} \times \left\{\frac{\beta'\left(e^{\beta' L} - e^{-\alpha L}\right) + \beta'\left(e^{-\beta' L} - e^{-\alpha L}\right) + \alpha\left(e^{-\beta' L} - e^{\beta' L}\right)}{\left[e^{-\beta' L} - e^{\beta' L}\right]}\right\} \tag{5.16}$$

For illumination through ohmic electrode, for sufficient thick film photocurrent response is antibatic [245,260].

$$J_{Ohmic} = D'\left(\frac{dn'(x)}{dx}\right)_{x=L} \tag{5.17}$$

$$J_{Ohmic} = \frac{\alpha\varphi I_0 D'}{\beta'^2 - \alpha^2} \times \left\{ \frac{2\beta' - e^{-\alpha L}\left[\beta' e^{-\beta' L} + \beta' e^{\beta' L} - \alpha e^{-\beta' L} + \alpha e^{\beta' L}\right]}{\left[e^{-\beta' L} - e^{\beta' L}\right]} \right\} \quad (5.18)$$

Including the consideration of exciton density present in barrier layer along with bulk, the boundary condition are modified, and are given by [266],

$$n'_{barrier} = \int_0^{l_b} \varphi\, I_0 \alpha \exp(-\alpha x)\, dx = \varphi I_0 [1 - \exp(-\alpha l_b)] \quad (5.19)$$

$$\begin{aligned} n'_{ohmic} &= \int_0^{l_b} \varphi\, I_0 \alpha \exp[-\alpha(L - x)]\, dx \\ &= \varphi I_0 [\exp\{-\alpha(L - l_b)\}] \times [1 - \exp(-\alpha l_b)] \end{aligned} \quad (5.20)$$

This modification in boundary condition was introduced by Desormeaux, Max, and Leblanc [266]. Thus the net photocurrent from the organic side is a contribution from bulk as well as barrier. The photocurrent for light illumination from barrier electrode is given by [266],

$$J_{Barrier} = -D' \left(\frac{dn'(x)}{dx} \right)_{l_b} + n'_{barrier} \quad (5.21)$$

$$\begin{aligned} J_{Barrier} = {} & \frac{\alpha\varphi I_0 \beta' e^{-\alpha l_b}}{(\beta'^2 - \alpha^2)} \left[1 - e^{-\beta'(L - l_b)} \frac{\left[2e^{-\alpha(L - l_b)} - e^{-\beta'(L - l_b)}\right]}{\left[1 - e^{-2\beta'(L - l_b)}\right]} \right] \\ & + \varphi I_0 \left[1 - \frac{\beta'^2 e^{-\alpha l_b}}{\beta'^2 - \alpha^2} \right] \end{aligned} \quad (5.22)$$

For light illuminating from ohmic electrode, the photocurrent due to exciton diffusion is given by [266]

$$J_{ohmic} = -D' \left(\frac{dn'(x)}{dx} \right)_{l_b} + n'_{ohmic} \quad (5.23)$$

$$\begin{aligned} J_{ohmic} = {} & \frac{\alpha\varphi I_0 \beta' e^{-\alpha(L - l_b)}}{(\beta'^2 - \alpha^2)} \Bigg[1 \\ & - e^{-\beta'(L - l_b)} \frac{\left[2e^{\alpha(L - l_b)} - e^{-\beta'(L - l_b)}\right]}{\left[1 - e^{-2\beta'(L - l_b)}\right]} \Bigg] \\ & - \varphi I_0 e^{-\alpha L} \left[1 - \frac{\beta'^2 e^{-\alpha l_b}}{\beta'^2 - \alpha^2} \right] \end{aligned} \quad (5.24)$$

These models, when used isolated, might still not be able to generate the spectral response of OI devices. There are still few modification required for specific transport models like GDM or SM for free carriers in the bulk of organic semiconductors. Spectral response for the inorganic side in the OI heterojunction can be reproduced using equation 5.12, the consideration of exciton diffusion is not required for n-GaN.

Thus the response from all the components of OI devices can be summed to give an expression for net spectral photo current through the OI device. Such a combined equation can be written as

$$J_{ph}(OI\ HJ) = J_{exciton} + J_{free\ carrier}(organic) + J_{free\ carrier}(inorganic) \tag{5.25}$$

Total current density given by 5.21 can be used to simulate the spectral photocurrent response of the OI hybrid heterostructure devices.

5.3 Modifications Required

The existing models for simulating the spectral photocurrent response have been shown to deviate from the experimental curves [267,245]. Such devations can arise from the fact that the basic assumptions of the model do not take into consideration many factors related to device operation. In such case the modifications of the existing models is essential to have a clear picture of basic underlying phenomena giving rise to spectral photo current response. Here we will discuss few such areas were the modification is required.

Reflection from each layer

A heterostructure device is composed of many different layers of varying refractive index and thicknesses. The loss of incident light via reflection from the each layer has to be taken into account in the model trying to explain the photoresponse. Light reflected from the back electrode

can have significant effect on the spectral response in the tail absorption region. The higher wavelengths may not be able to reach back electrode, since they get absorbed by the intervening layer in the organic films, but the lower energy photon can undergo multiple reflections giving increased response. The effect of reflection from the thick electrode was seen in the form of increased response at lower wavelengths in the n-GaN/Polymer films which was less for thin (~ 15 nm Au) top electrodes. In the studies [266] of Desormeaux, Max, and Leblanc they have tried to include the effect of multiple reflections in the film in their model, which has an effect of reducing the contrast between the symbatic and antibatic response.

Disorder within the polymer semiconductor

The models discussed here, were developed mainly for small organic molecules. These small molecules have a well defined size and conjugation length, planarity, rigid structure and mono dispersity. These models provide good qualitative agreement between the experimental curves and model fits for small molecule organic semiconductor materials. Organic polymer semiconductor systems represent a much disordered class of semiconductors where the conjugation length and molecular weights vary over a wide range. The electronic structure and charge transport in these materials are generally disordered, as shown in chapter 1. Considerations of such system dependent mechanisms are required to have a better qualitative agreement between the experimental and model curves for inorganic – polymer semiconductor heterostructures.

Charge transfer efficiency of the interface

It has been shown previously that the interface controls many of the properties of n-GaN/polymer heterostructures. In case of photoconductivity, there is a requirement of exciton dissociation and electron transfer towards n-GaN for a significant photo-response. The interface charge transport thus plays a significant role in deciding the spectral response of OI systems. Introduction of interface charge transport parameters in the model will be essential for simulating the spectral response for OI HJ's.

Imperfection in the n-GaN crystal

The n-GaN wafers used are not completely defect free; there are surface terminated states and bulk defect states which give rise to decrease in mobility and defect state PL emission. Such states cause strains and offer non radiative recombination sites inside the bulk causing loss of carriers. Effects are visible in reduced PL from the band gap emission (365-370 nm) and increased PL at lower wavelength (550 nm). Thus, it can be said that the imperfections have a definitive role to play in the spectral response of the OI devices, and they should be taken into consideration in the models.

Other perturbations to the system, like temperature, ambient and background carrier density effects have not been considered in these models. Even though the perturbation introduced by such processes will be less, they may cause deviations from the experimentally measured response.

5.4 Implications

The model discussed can be used for simulating the spectral photocurrent response for the n-GaN/polymer hybrid heterostructure using generation, transport and recombination rates of known process. The model can be utilized to get a basic understanding of the kinetics involved in photoconductivity of the n-GaN/polymer hybrid structures. A drift term has been included in the general diffusion equation to account for the applied electric bias across the heterostructure. Though any comparison has not been presented here between the experimental spectral responses and simulated response but it can be guesses that the model is still not complete and requires a significant amount of modifications to generate spectral response close to what is experimentally observed for OI heterostructures. The opposite response observed, compared to what is predicted in case of n-GaN/donor polymer heterostructure can be explained by photocurrent modeling with the proper considerations of disorder transport in polymer, barrier and ohmic electrode workfunction offsets and surface and interface defect states.

CHAPTER 6

SUMMARY AND FUTURE DIRECTIONS

OI semiconductor heterostructures are a new class of systems which have shown many novel properties. These new classes of materials have shown potential for application in the field of LED's, photodetectors, Solar cells and high mobility FET channels. The use of hybrid materials and structures in semiconductors in not very new, the initial Si/organic semiconductor based devices are very well studied. One of the important aspects in these devices is the properties of charge transport across the organic – inorganic heterostructure. It is essential to understand the transport properties for efficient hybrid devices. In this study we have tried to look at some of the transport properties in the n-GaN/polymer hybrid heterojunction. The steady state measurements have been utilized to study the transport parameters like interface trap states density, barrier height between organic and inorganic layers etc. The modulated photocurrent measurements have been performed for studying the transport properties under illumination.

The hybrid structure n-GaN/pBTTT shows a characteristic PL emission which does not matches with the PL response of any of the pristine material. The emission energy is intermediate of n-GaN and pBTTT emission energy. Such emission can be the signature of formation of interface states of energies in between the pBTTT and n-GaN emission states. The current – voltage characteristics have been studied as a function of different energy structures and top electrode configuration. We see that the energy level alignment has a significant effect on the rectification ratios and saturation current density of OI diodes. The light response for type I and type II heterostructures are completely different. It was observed that the top electrode plays an important role in determining the space charge region. The small signal admittance measurement was used to calculate built in voltage (V_{Bi}), since, the values are much higher than

expected, it suggests that the corrections are required in the existing models for application in n-GaN/polymer OI diodes. Capacitance-frequency measurements could give valuable information on interface state densities and trap response with frequency, which shows a shift from bulk to interface capacitance at around 2-3 MHz frequency. The IMPS studies carried out using small modulated light source suggests presence of three response regions which corresponds to three wavelength ranges (< 400 nm, 400 nm – 550 nm, > 550 nm). The frequency response at higher wavelengths (> 600 nm) shows a steady increase in photocurrent, which are generally observed for lower efficiency, trap dominated devices. Such response is the characteristics of recombination dominated transport.

Photoconductivity measurement shows symbatic and antibatic response in the photocurrent spectral response when illuminated from Au and n-GaN side respectively. Such responses are critical to the energy band structure present in the bulk of the material. Forward and reverse biased responses show striking differences, which supports the idea of the role of band structure in spectral response. The zero bias response from the n-GaN/p-type polymers is opposite with respect to the direction of illumination, i.e. symbatic response is observed for illumination form ohmic electrode while antibatic response is observed for illumination from barrier interface. Response expected from band structure, as shown in figure 3.4, is opposite to what is observed experimentally, such a response is not present for n-GaN/N2200, type II heterostructure devices. Observed opposite response can arise because of the effect of interface trap or asymmetric bending of Conduction band and valance band on the transport of photogenerated carriers, the true origin for these responses have not been understood properly. Measurements by varying the external control parameters like applied field, film thickness and background illumination gives useful information on parameters that affect the carrier transport at the interface and bulk.

Methods to model the spectral photocurrent response from the n-GaN/Polymer heterostructures have been presented. A systematic consideration of exciton generation, exciton diffusion to the barrier electrode and charge generation by exciton dissociation under the barrier field has been considered. The total current density from the OI device is speculated to be a mutual combination of exciton in organic region reaching the barrier interface, drift and/or diffusion dominated transport of generated charge carriers, and drift or diffusion dominated

transport in inorganic semiconductor. Any comparison between the theoretical and experimental spectral response has not been presented, the assumptions made in the model requires consideration of various carrier transport and loss mechanisms. .

Further a detailed analysis of the results along with the modification of the models is required to extract the transport parameters accurately. Correlation between the derived transport parameters and physical process is essential for a better understanding. The model derived for spectral photocurrent response has to be compared with experimental curves for n-GaN/Polymer devices for validating their applicability. Modeling of IMPS response in terms of generation, transport and recombination rates is required to understand the physical origin of the characteristic peak at 10 kHz and the wavelength dependent response. Understanding the device transport properties will also help understanding the reasons for lower efficiencies, and help improving the device performance.

REFERENCES

1 *Experimental Researches in Electricity, Volume 1.* (London: Richard and John Edward Taylor, 1839), Faraday, M. pp.122-124 (para. 432).

2 "On the current conduction in metal sulphides (title translated from German into English)", K.F. Braun, Ann. Phys. Chem., 153 (1874), 556. (In German) An English translation can be found in "*Semiconductor Devices: Pioneering Papers*", edited by S.M. Sze, World Scientific, Singapore, 1991, pp. 377–380.

3 *Handbook for Electrical Engineers, 2nd Ed.* Pender, Harold; William Arthur del Mar, New York: J. Wiley & Sons.. pp. 1268, (1922).

4 "transistor." *Encyclopedia Britannica. 2008. Encyclopedia Britannica Online*. 09 Nov. 2008. Nobel Organization citation, (1956).

5 Ghioni, M. Zappa, F. ; Kesan, V.P. ; Warnock, J., IEEE transactions on electronic devices, 43, 7, 1054 – 1060, (1996)

6 *Semiconductor device fundamentals*, Robert F. Pierret, Pearson, (1996)

7 *Encyclopedia of laser physics and technology*, Dr. Rüdiger Paschotta, RR photonics consulting, (2011)

8 Photodiode characteristics, UDT sensors corporation,

9 P.Calvani, M.Girolami, S. Cartra, M.C. Rossi, G. Conte, Nuclear instruments and methods in physics research A, 610, 311-313, (2009)

10 Silicon photodetectors, HAMAMATSU PHOTONICS DEUTSCHLAND GmbH, Arzbergerstr. 10, D-82211 Herrsching am Ammersee, Germany.

11 InGaAs photodetectors, HAMAMATSU PHOTONICS DEUTSCHLAND GmbH, Arzbergerstr. 10, D-82211 Herrsching am Ammersee, Germany.

12 Hsiao-Wen Zan, Wei-Tsung Chen, Hsiu-Wen Hsueh, Shih-Chin Kao, Ming-Che Ku, Chuang-Chuang Tsai, and Hsin-Fei Meng, Appl. Phys. Lett. 97, 203506, (2010)

13 Takayoshi Kobayashi, Synthetic metals, 50, 1-3, 565-581, (1992)

14 *Semiconductor materials, an introduction to basic principles*, B.G.Yacobi, Microdevices physics and fabrication technology, Kluwer academic/Plenum publishers, Newyork, (2003)

15 *Organic Semiconductors: Properties, Fabrication and Applications*, Maria A. Velasquez, Nova Science Pub, (2011)

16 Gong, X., Tong, M., Xia, Y., Cai, W., Moon, J. S., Cao, Y., Yu, G., Shieh, C.L., Nilsson, B. and Heeger, A. J., Science 325, 1665, (2009).

17 Michael S. Arnold, Jeramy D. Zimmerman, Christopher K. Renshaw, Xin Xu, Richard R. Lunt, Christine M. Austin and Stephen R. Forrest, Nano Lett., 9 (9), pp 3354–3358, (2009)

18 Zisheng Su, Wenlian Li, Bei Chu, Tianle Li, Jianzhuo Zhu, Guang Zhang, Fei Yan, Xiao Li, Yiren Chen, and Chun-Sing Lee, Appl. Phys. Lett. 93, 103309, (2008)

19 So, F.F.; Forrest, S.R., Electron Devices, IEEE Transactions on , vol.36, no.1, 66-69, (1989)

20 Fahrettin Yakuphanoglu, Sensors and Actuators A: Physical, 141, 2, (2008)

21 Yamaura, J., Muraoka, Y., Yamauchi, T., Muramatsu, T., Hiroi, Z., 83, 11, (2003)

22 J. Koenigsberger, K. Schilling, Ann. Physik 32, 179, (1910)

23 M. Volmer, Ann. Physik, 40 775, (1913)

24 M. Pope, H. Kallmann and P. Magnante, J. Chem. Phys. 38, 2042, (1963)

25 C. K. Chiang, C. R. Fincher, Jr., Y. W. Park, A. J. Heeger, H. Shirakawa, E. J. Louis, S. C. Gau, and Alan G. MacDiarmid, Phys. Rev. Lett. 39, 1098, (1977).

26 Heeger, A. J.; Schrieffer, J. R.; Su, W.P., Reviews of Modern Physics 60: 781, (1988)

27 C. W. Tang, Appl. Phys. Lett. 48, 183, (1986)

28 H. Koezuka, A. Tsumara, and T. Ando, synth. Met. 18, 699, (1987)

29 J.H. Burroughes, C. A. Jones, and R. H. Friend, nature 335, 137, (1988)

30 Tang, C.W.; Vanslyke, S.A., Appl. Phys. Lett. 51 12, 913, (1987)

31 Burroughes, J. H.; Bradley, D. D. C.; Brown, A. R.; Marks, R. N.; MacKay, K.; Friend, R. H.; Burns, P. L.; Holmes, A. B., Nature 347 (6293): 539, (1990)

32 Padinger, F., Rittberger, R. S. and S., S. N. Effects, Adv. Funct. Mater. 13, 85, (2003).

33 Reyes-Reyes, M., Kim, K. and Carroll, D. L., Appl. Phys. Lett. 87, 083506, (2005).

34 Drury, C. J., Mutsaers, C. M. J., Hart, C. M., Matters, M. and De Leeuw, D. M., Appl. Phys. Lett. 73, 108, (1998).

35 Yoshiro Yamashita, Sci. Technol. Adv. Mater. 10 (2): 024313, (1990)

36 R. Peierls, Quantum theory of solids (Clarendon, Oxford) (1955)

37 Chamberlain, G. A., Organic solar cells: a review. Solar. Cells, 8, 47, (1983)

38 Hertel, D.; Baessler, H., Chem Phys Chem, 9, 666, (2008)

39 K.P.C. Vollhardt, Organische Chemie, VCH- Verlag, Weinheim, (1990)

40 Sanjay Tiwari, N C Greenham, Optical and Quantum Electronics, 41, 2, (2009)

41 Chin, V.W.L, T.L. Tansley, T. Osotchan, J. Appl. Phys. 75(11), 7365-7372, (1994)

42 Paul E. Shaw, Arvydas Ruseckas, and Ifor D. W. Samuel, Adv. Mater. 20, 3516, (2008)

43 M. Knupfer, Applied Physics A: Materials Science & Processing , 77, 5, 623 – 626, (2003)

44 Peumans P, Yakimov A, Forrest SR., Journal of Applied Physics, 93(7): 3693-3723, (2003)

45 Muth, J.F, J.H. Lee, I.K. Shmagin, R.M. Kolbas, H.C. Casey, Jr., B.P. Keller, U.K. Mishra, S.P. DenBaars, Appl. Phys. Lett. 71(18) , 2572-2574, (1997)

46 J W Orton and C T Foxon, Rep. Prog. Phys, 61, (1998)

47 J. Cornil, D. Beljonns, J. P. Calbert, J. L. Bŕedes, Adv. Mater. 13, 1053, (2001)

48 *Electrical characterization of organic electronic materials and devices*, Peter Stallinga, John Wiley and sons, (2009)

49 M. Springbore, K. Schmidt, H. Meider and L. De Maria, *Organic Electronic materials conjugated polymers and low molecular weight organic solids*, R. Farchioni, G. Grosso, Springer , (2001)

50 H. Bässler, Phys. Status Solidi B, 175, 15, (1993)

51 M. Shur, M. Hack, J. Appl. Phys. 55, 3831, (1989)

52 N. Tessler, Y. Roichman, Org. Electronics, 6, 200, (2005)

53 Novikov, S. V.; Dunlap, D. H.; Kenkre, V. M.; Parris, P. E.; Vannikov, A. V., Phys. Rev. Lett., 81, (20), 4472-4475, (1998)

54 T. Holstein, Ann. Phys., 8 325 (1959), T. Holstein Ann. Phys., 8, 343, (1959)

55 S. Brazovskii, N. Kirova, Z. G. Yu, A. R. Bishop, A. Saxena, Opt. Mater. 9, 502, (1998)

56 M. P. Sarachik, P. Dai, Phys. Status Solidi B, 230, 205, (2002)

57 H. Bässler, Phys. Status Solidi B 175, 15, (1993)

58 V. Ambegaokar, B. I. Halperin, J. S. Langer, Phys. Rev. B 4, 2612, (1971)

59 D. C. Look, D.C. Walters, M.O. Manashreh, J. R. Sizelove, C. E. Stitz, K. R. Evans Phys. Rev. B 42, 3578, (1990)

60 N. F. Mott, W. D. Twose, Adv. Phys. 10, 107, (1961)

61 B. I. Shklouskii, Sov. Phys. Semicond. 6, 1053, (1973)

62 H. A. Albuquerque, A. G. de Oliveira, G. M. Ribeiro, R. L. da Silva, R. M. Rubinger, J. Appl. Phys. 95, 3883, (2004)

63 Scher, H. and Montroll, E. W., Phys. Rev. B 12, 2455, (1975)

64 Van der Auweraer, M.; De Schryver, F. C.; Borsenberger, P. M.; Bässler, H., Adv. Mater., 6, (3), 199-213, (1994)

65 Gailberger, M.; Bassler, H., Phys. Rev. B, 44, (16), 8643-8651, (1991)

66 Shaked, S.; Tal, S.; Roichman, Y.; Razin, A.; Xiao, S.; Eichen, Y.; Tessler, N., Adv. Mater., 15, (11), 913-916, (2003)

67 S. V. Novikov, D. H. Dunlap, V. M. Kenkre, P. E. Parris, and A. V. Vannikov, Physical Review Letters 81, 4472-4475, (1998).

68 Y. N. Gartstein and E. M. Conwell, Physical Review B, 51, 6947-6952, (1995).

69 H. Kageyama, K. Ohnishi, S. Nomura, and Y. Shirota, Chemical Physics Letters 277, 137-141, (1997).

70 Fishchuk, II, A. Kadashchuk, H. Bassler, and S. Nespurek, Physical Review B 67, (2003).

71 V. I. Arkhipov, P. Heremans, E. V. Emelianova, G. J. Adriaenssens, and H. Bassler, Chemical Physics 288, 51-55, (2003).

72 S. Rackovsky and H. Scher, Journal of Chemical Physics 111, 3668-74, (1999).

73 H. Scher and T. Holstein, Philosophical Magazine B - Physics of Condensed Matter Statistical Mechanics Electronic Optical and Magnetic Properties 44, 343-56, (1981).

74 W.P.Su, J.R.Schrieffer, Proc. Natl. Acad. Sci. 7, 5626 (1980)

75 K. Murata, Y. Shimoi, S. Abe, S. Kuroda, T. Noguchi, T. Ohinishi, chem.. Phys. 227, 191, (1998)

76 S. C. Graham, D.D.C. Bradley, R. H. Friend, Synthe. Met. 41-43, 1277, (1991)

77 S. Mazumdar, F. Guo, Synth. Met. 78, 187, (1996)

78 V. I. Klimov, D.W. Mcbranch, N. Barashkov, J. Ferraris, Phys. Rev. B 58, 7654, (1994)

79 B. Kraabel, D. Moses, A.J. Heeger, J. Chem. Phys. 103, 5102 (1995)

80 S.V. Frolov, M.Liess, P.A. Lane, W.Gellermann, Z.V. Vardeny, M. Ozaki, K. Yoshino, Phys. Rev. Lett. 78, 4285 (1997)

81 Y.Shimoi, S. Abe, Phys. Rev. B 50, 14781 (1996)

82 E.M. Conwell, *Organic Electronic materials conjugated polymers and low molecular weight organic solids*, R. Farchioni, G. Grosso, Springer , (2001)

83 E. L. Frankevish, A. A. Lymarev, I. Sokolik, F.E. Karasz, S. Blumstengel, R. Baughman, H.H. Horhold, Phys. Rev. 46, 9320, (1992)

84 D. Moses, D. Comoretto, C.H. Lee, A.J. Heeger, F. Wudl, Science 258,1474, (1992)

85 R. Kersting, U. Lemmer, R.F. Mahrt, K.Leo, H. Kurz, H. Bässler, E.O. Gobel. Phys. Rev. Lett. 70, 3820, (1993)

86 U. Rauscher, H. Bässler, D.D. C. Bradley, M. Hennecke, Phys. Rev. B 42, 9830, (1990)

87 H. Bässler, M. Grailberger, R.F. Mahrt, J.M. Oberski, G. Weiser, Synth. Met. 49-50, 341, (1992)

88 M. Yan, L.J. Rothberg, F. Papadimitrakopoulous, M.E. Galvin, T.M. Miller, Phys. Rev. Lett. 73, 744, (1994)

89 , F. Papadimitrakopoulous, M. Yan, L.J. Rothberg, H.E. Katz, M.E. Galvin. Mol. Cryst. Liq. Cryst. 256, 663, (1994)

90 M. I. Khsn, G.C. Bazan, Z.D. Popovic, Chem. Phys. Lett. 298. 309, (1998)

91 V.I. Arkhipov, H. Bässler, M. Deussen, E. O. Gobel, R. Kersting, H. Kurz, U. Lemmer , R.F. Mahrt, Phys. Rev. B 52, 4932, (1995)

92 M. Scheidler, U. Lemmer, r. Kersting, S. Karg, W. Riess, B. Cleve, R.F. Mahrt, H. Kurz, H. Bässler, E.O. Gobel, P. Thomas, Phys. Rev. B 54, 5536, (1996)

93 *Electrical transport in solids*, Kwan C. Kao and Wei Hwang, Pergamon press, (1981)

94 Deibel, C.; Baumann, A.; Dyakonov, V., Appl. Phys. Lett., 93, (16), 163303-3, (2008)

95 Pivrikas, A.; Juśka, G.; Ã–sterbacka, R.; Westerling, M.; ViliÅ«nas, M.; Arlauskas, K.; Stubb, H., Phys. Rev. B, 71, (12), 125205, (2005)

96 Kevin P. O'Donnell, *Group III nitride semiconductor compounds physics and application*, Ed. Bernard Gil, Series on semiconductor science and technology, Oxford science publication, (1998)

97 *Properties of group III nitrides*, edited by james H. Edger (EMIS data review 11,INSPEC, London, (1995)

98 I. Akasaki, H. Amano, M. Kito and K. Hiramatsu , Journal of Luminscence, 48-9, 666-670.

99 W.J.Meng, in Group III nitrides, ed. J.H. Edgar, INSPEC, London, UK. PP. 22-29

100 Galina Popovici, Hadis Morkoç and S. Noor Mohammed, *Group III semiconductor compounds physics and applications*, ed. Bernard Gil, Series on semiconductor science and technology, Oxford Science publication, pp. 20, (1998)

101 W.A.Harris, *electronic structure and properties of solids*, Dover, NY, PP. 174-179, (1980)

102 W. Y. Ching and B. N. Harmon, Phys. Rev. B 34, 5305, (1986)

103 W. R. L. Larnbrecht and B. Segal, Phys. Rev. B 43, 7070, (1991)

104 C. Yeh, Z. W. Lu, S. Froyen, and A. Zunger, Phys. Rev. B 46 10086 (1992); C. Yeh, S. Wei, and A. Zunger, ibid. 50, 2715, (1994).

105 Masakatsu Suzuki, Takeshi Uenoyama, and Akira Yanase , Phys. Rev. B, 52, 11, (1995)

106 NSM semiconductor archive

107 Bougrov V., Levinshtein M.E., Rumyantsev S.L., Zubrilov A., *Properties of Advanced SemiconductorMaterials GaN, AlN, InN, BN, SiC, SiGe*. Eds. Levinshtein M.E., Rumyantsev S.L., Shur M.S., John Wiley & Sons, Inc., New York, 1-30. 2001

108 Ejder, E., Phys. Status Solidi (a), 6, 445-448, (1971)

109 Jin Joo Song and Wei Shan*, Group III Nitride semiconductor compounds physics and applications*, Ed. Bernard Gil, Series on semiconductor science and technology, Oxford science publication.

110 Dennis K. Wickenden, Zhen Chun Huang, D. Brent Mott and Peter K. Shu. Jhons Hopkins Al. technical digest, 18, 2, (1997)

111 *Photoconductivity of solids*, Richard H. Bube, John Wiley and Sons, (1960).

112 Yuh – Renn Wu, Madhusudan Singh and Jasprit Singh, *Polarization effect in semiconductor. From ab Initio theory to device application*, Ed. Colin Wood, Debdeep Jena, Springer (2008).

113 Kolnik, J., Oguzman I.H., Brennan K.F., Wang R., Ruden P.P., Wang, Y. J. Appl. Phys. 78(2), 1033-1038, (1995)

114 Ilegems, M., Dingle, R., J. Appl. Phys. 44 (1973) 4234, Ilegems, M., Montgomery, H.C., J. Phys. Chem. Solids 34 885, (1972)

115 Chow, T.P, Ghezzo. SiC power devices. in *III-Nitride, SiC, and Diamond Materials for Electronic Devices*. Eds. Gaskill D.K, Brandt C.D. and Nemanich R.J., Material Research Society Symposium Proceedings,Pittsburgh, PA. **423** (1996), 69-73.

116 Sushobhan Avasthi , Stephanie Lee , Yueh-Lin Loo , and James C. Sturm, Adv. Mater. 23, 5762, (2011)

117 Wendy U. Huynh, Janke J. Dittmer and A. Paul Alivisatos, Science, 295, 5564, (2002)

118 Zhang, Chi; Heeger, Alan J, J. Appl. Phys. 84, 3, (1998)

119 Clint J. Novotny, Edward T. Yu, Paul K. L. Yu, Nano Lett., 8 (3), pp 775–779, (2008)

120 Lidan Wang, Dongxu Zhao, Zisheng Su, Fang Fang, Binghui Li, Zhenzhong Zhang, Dezhen Shen, Xiaohua Wang, Organic Electronics, 11, 7, (2010)

121 C.R.Kagan, D. B. Mitzi, C. D. Dimitrakopoulos, Science, 286, 945, (1999)

122 V. M. Agranovich, D. M. Basko, G. C. La Rocca, and F. Bassani, J. Phys.: Condens. Matter 10, 9369, (1998).

123 T. Goto, N. Ohshima, T. A. Mousdis, and G. C. Papavassiliou, Solid State Commun. 117, 13, (2001).

124 X. Hong, T. Ishihara, and A. V. Nurmikko, Phys. Rev. B 45, 6961, (1992).

125 6X. Huang, J. Li, Y. Zhang, and A. Mascarenhas, J. Am. Chem. Soc. 125, 7049, (2003).

126 M. H. Chan, J. Y. Chen, T. Y. Lin, and Y. F. Chen, Appl. Phys. Lett. 100, 021912, (2012).

127 S. Peters, F. Glöckler, U. Lemmer, M. Gerken, Thin solid films, 516, 14, (2008)

128 I. A. Levitsky, W. B. Euler, N. Tokranova, B. Xu, and J. Castracane, Appl. Phys. Lett. 85, 6245, (2004)

129 Hyunjin Kim, Ze-Lei Guan, Qian Sun, Antoine Kahn, Jung Han, and Arto Nurmikko, J. Appl. Phys. 107, 113707, (2010)

130 Xiaofei Lei, Fute Zhang, Tao Song, and Baoquan Sun, Appl. Phys. Lett. 99, 233305, (2011)

131 Mariani, Giacomo; Laghumavarapu, Ramesh B.; Tremolet de Villers, Bertrand; Shapiro, Joshua; Senanayake, Pradeep; Lin, Andrew; Schwartz, Benjamin J.; Huffaker, Diana L., App. Phys. Lett., 97, 1, (2010)

132 *Fundamentals of solid state electronics*, Chih-Tang Sah, World scientific, (1991)

133 S.R. Forrest, M. L. Kaplan, and P. H. Schmidt, Appl. Phys. Lett. 55, 6, (1984)

134 N. F. Mott and R. W. Gurney, *Electronic Processes in Ionic Crystals* (Clarendon, Oxford) (1940).

135 S. R. Forrest and F. F. So, Appl. Phys. Lett. 64, 1, (1988)

136 C. R. Crowell and M. Beguwala, Solid-State Electron. 14,1149, (1971).

137 *Conjugated polymer and metal interfaces,* W.R. Salaneck, K.Seki, A.Kahn, and J.-J. Pireaux (Marcel Dekker, New York, 2002) and references therein

138 J.C.Scott, J. Vac. Sci. Technol. A 21, 521, (2003)

139 W.Brötting, H. Riel, T. Beierlein and W. Riess, J. Appl. Phys. 89, 1704, (2001)

140 P.H. Nguyen, S. Scheinert, S. Berleb, W. Brötting, and G. Paasch, organic electronics 2, 105, (2001)

141 J.R. Ostrick, A. Dodabalapur, L. Torsi, A.J. Lovinger, E.R.Kwock, T.M. miller, M.Galvin, M. Berggren, and H. E. Katz. J. Appl. Phys. 81, 6804, (1997)

142 N karl *, Organic electronics materials*, P. 283 Ed. R. Farchioni and G. Grosso, Springer series in material science 41 (Springer, Berlin,) (2001)

143 A. Koma, J. Cryst. Growth 201/202, 236, (1999)

144 H.Peisert, T. Schwieger, J.M. Auerhammer, M.Knupfer, M.S. Golden, J.Fink, P.R. Bressler, and M.Mast, J. Appl. Phys. 90, 466, (2001)

145 M. Knupfer and H. Peisert, *Physics of organic semiconductors*, Ed. W. Brötting Wiley VCH (2005)

146 S.M.Sze, *Physics of semiconductor devices*. John Wiley and Sons, New York, (1981)

147 M. Knupfer and H. Peisert, *Physics of organic semiconductors*, p. 50, Ed. W. Brötting Wiley VCH and references there in, (2005)

148 H.Ishii, K.Sugiyama, E.Ito, and E.Seki, K. Adv, Mater. 11, 605, (1999)

149 *Electronic properties of semiconductor interface,* Winfried Mönch, Surface science series, Springer Berlin, (2004)

150 S. R. Forrest, M. L. Kaplan, P. H. Schmidt, W. L. Feldmann, and E. Yanowski, Appl. Phys. Lett. 41, 1, (1982)

151 S. A. Forrest, M. L Kaplan, and P. H. Schmidt, Appl. Phys Lett. 56, 2, (1984)

152 Michale, J. Sailor, Floyed. L. Klavetter, Robert H. Grubbs and Nathan S. Lewis, Nature Lett. 346, 155, (1990)

153 T. Ben Jomaa, L. Beji, A. Ltaeif, A. Bouazizi, Material science and engineering: C, 26, 2-3, (2006)

154 B.N. Park, J. J. Uhlrich, T. F. Kuech, and P. G. Evans, J. Appl. Phys. 106, 013713, (2009)

155 I. A. Levitsky, W. B. Euler, N. Tokranova, B. Xu, and J. Castracane. Appl. Phys. Lett. 85, 6245, (2004)

156 Chin-Yi Liu, Zachary C. Holman and Uwe R. Kortshagen, Nano Lett., 9 (1), 449, (2009)

157 C. H. Chen I. Shih, J Mater Sci: Mater Electron 17, 1047–1053, (2006)

158 J. W. Levell, M. E. Giardini, and I. D. W. Samuel, Optics Express, 18, 4, 3219-3225, (2010).

159 Jun Chen; Dayan Ban; Helander, M.G.; Zhenghong Lu; Poole, P., Lasers and Electro-Optics (CLEO), 2011 Conference on, 1-2, (2011)

160 Chanyawadee, S., Lagoudakis, P.G., Harley, R.T., Lidzey, D.G. and Henini, M, Phy. Rev. B, 77, (19), 193402, (2008)

161 Steven K. Hau, Hin-Lap Yip, Nam Seob Baek, Jingyu Zou, Kevin O'Malley, and Alex K.-Y. Jen, Appl. Phys. Lett. 92, 253301, (2008)

162 G. Li, C.-W. Chu, V. Shrotriya, J. Huang, and Y. Yang, Appl. Phys. Lett. 88, 253503, (2006)

163 Jin Young Kim, Sun Hee Kim, Hyun-Ho Lee, Kwanghee Lee, Wanli Ma, Xiong Gong, and Alan J. Heeger, Adv. Mater. 18, 572, (2006)

164 Iain Mcculloch, Martin Heeney, Clare Bailey, Kristijuonas Genevicius, Iain Macdonald, Maxim Shkunov, David Sparrowe, Steve Tierney, Robert Wagner, Weimin Zang, Michale L. Chabinyc, R. Joesph Kline, Michale D. Mcgehee and Michale F. Toney, Nature, 5, 328, (2006)

165 Jack E. Parmer, Alex C. Mayer, Brian E. Hardin, Shawn R. Scully, Michael D. McGehee et al. Appl. Phys. Lett. 92, 113309, (2008)

166 Luminescence Tech. Corporation, Taiwan, 2F, No. 17, R&D Road II, Science-Based Industrial Park, Hsin-Chu 30076, Taiwan, R.O.C.

167 Cunningham, P. D. and Hayden, L. M. Carrier The J. of Phys. Chem. C 112, 7928 (2008).

168 S. Hugger, R. Thomann, T. Heinzel, T. Thurn-Albrecht, Colloid Polym Sci, 282: 932–938, (2004)

169 Renato Colle, Giuseppe Grosso, Alberto Ronzani, and Claudio M. Zicovich-Wilson Phys. Status Solidi B 248, No. 6, 1360–1368 (2011).

170 He Yan, Zhihua Chen, Yan Zheng, Christopher Newman, Jordan R. Quinn, Florian Do¨tz, Marcel Kastler & Antonio Facchetti, Nature 457 (2009)

171 Z. Chen, Y, Zheng, H. Yan and A. Facchetti, J. Am. Chem. Soc. 131, 8 – 9 (2009)

172 Polyera Corporation, 8045 LAMON AVE, STE 140, SKOKIE, IL 60077-5318, USA

173 *Properties of Group III Nitrides* (EMIS Datareview Series 11) ed J H Edgar (London: INSPEC, IEE) p 71, Porowski S and Grzegory I (1994)

174 *Group III Nitride semiconductor compounds physics and applications*, p. 77 Bernard Gill, Oxford Science publications (1998)

175 *Group III Nitride semiconductor compounds physics and applications*, Bernard Gill, Oxford Science publications (1998)

176 Ilegems M and Montgomery H C J. Phys. Chem. Solids 34 885 (1973)

177 J.W. Orton and C. T. Foxon, Rep. Prog. Phys. 61 1, (1998)

178 Sung Heum Park, Anshuman Roy, Serge Beaupré, Shinuk Cho, Nelson Coates, Ji Sun Moon, Daniel Moses, Mario Leclerc, Kwanghee Lee & Alan J. Heeger, Nature Photonics 3, 297 - 302 (2009)

179 M.S. White, D.C. Olson, S.E. Shaheen, N. Kopidakis, D.S. Ginley, Applied Physics Letters, 89 , 143517-1, (2009)

180 Chih-Wei Chu, Sheng-Han Li, Chieh-Wei Chen, Vishal Shrotriya, and Yang Yang, Appl. Phys. Lett. 87, 193508 (2005)

181 Vishal Shrotriya, Gang Li, Yan Yao, Chih-Wei Chu, and Yang Yang, Appl. Phys. Lett. 88, 073508 (2006)

182 Mikkel Jørgensen, Kion Norrman, Suren A. Gevorgyan, Thomas Tromholt, Birgitta Andreasen, Frederik C. Krebs, Adv. Mat. 24, 5, 580, (2012)

183 Min Chul Suh, Ho Kyoon Chung, Sang-Yeol Kim, Jang Hyuk Kwon, Byung Doo Chin, Chem. Phys. Lett, 413, 1-3, 205, (2005)

184 F. Li and H. Tang, J. Anderegg, J. Shinar, Appl. Phys. Lett. 70 (10), (1997)

185 Hong Ma, Hin-Lap Yip, Fei Huang, and Alex K.-Y. Jen, Adv. Funct. Mater., 20, 1371–1388, (2010)

186 Ching-Lin Fan, Yu-Zuo Lin and Cheng-Han Huang, Semicond. Sci. Technol. 26, 045006, (2011)

187 Tipler, Paul A. and Llewellyn, Ralph A., Modern Physics, 3rd Ed., W.H. Freeman, 1999

188 H. B. Michaelson: J. Appl. Phys. 48 (1977) 4729.

189 J. S. Foresi and T. D. Moustakas, Appl. Phys. Lett. 62 (22), 2859, (1993)

190 Ki Man Kang, J. M. Jo and Joon Seop Kwak, Hyunsoo Kim, Y. S. Kim, C. Sone and Y. Park, Journal of the Korean Physical Society, Vol. 55, No. 1, pp. 318-321, (2009)

191 Kamal Asadi, Dago M. de Leeuw, Bert de Boer & Paul W. M. Blom, Nature Mater. 7, 547 - 550 (2008)

192 M.J. Małachowski and J. Żmija, Opto-electronics review, **18**(2), 121–136, (2010)

193 Z. Chiguvare, J. Parisi, and V. Dyakonov, J. Appl. Phys. 94, 4, 2440, (2003)

194 Srinivas Sista, Ziruo Hong, Mi-Hyae Park, Zheng Xu, and Yang Yang, Adv. Mater., 22, E77–E80, (2010)

195 Kim, Y. Choulis, S.A. Nelson, J., Bradley, D.D.C, Cook, S. and Durrant, J.R., Appl. Phys. Lett., 86, 063503, (2005)

196 Jack E. Parmer, Alex C. Mayer, Brian E. Hardin, Shawn R. Scully, Michael D. McGehee, Martin Heeney, and Iain McCulloch, Appl. Phys. Lett., 92, 11, (2008)

197 C. J. Sun, P. Kung, A. Saxler, H. Ohsato, E. Bigan, M. Razeghi, and D. K. Gaskill, J. Appl. Phys. **76**, 236, (1994)

198 Christoph J. Brabec, N. Serdar Sariciftci, Jan Kees Hummelen, Advanced Functional Materials, Vol. 11 No: 1, pp. 15–26 (2001)

199 M. A. Baldo and S. R. Forrest, Phys. Rev. B 64, 085201 (2001)

200 Won-Ju Cho, Journal of semiconductor technology and science, 7, 2, pp-82, (2007)

201 Martin S. Kunz, Kenneth R. Shull, and Andrew J. Kellock, J. Appl. Phys. **72**, 4458 (1992)

202 Y. Segui, Bui Ai , C. Bagnol, J. Pistre, Y. Danto, and A. S. Barriere, J. Appl. Phys. **50**, 2973 (1979)

203 Douglas H. Cole, Kenneth R. Shull, L.E. Rehn, P.M. Baldo, Nuclear Instruments and Methods in Physics Research Section B: Beam Interactions with Materials and Atoms, 136-138, pp. 283-289, (1998)

204 Nadine Gergel-Hackett, Behrang Hamadani, Barbara Dunlap, John Suehle, Curt Richter, Christina Hacker, and David Gundlach, IEEE Electron devices letters,. 30, 7, (2009)

205 Hye-Jeong Park, Kang-Hyuck Lee, Brijesh Kumar, Kyung-Sik Shin, Soon-Wook Jeong, and Sang-Woo Kim, Journal of Nanoelectronics and Optoelectronics, 5, 1–4, (2010)

206 Yanming Sun , Christopher J. Takacs , Sarah R. Cowan , Jung Hwa Seo , Xiong Gong ,

Anshuman Roy , and Alan J. Heeger, Adv. Mater., 23, 2226–2230, (2011)

207 G. Li, C.-W. Chu, V. Shrotriya, J. Huang, and Y. Yang, Appl. Phys. Lett., **88**, 253503 (2006)

208 L.S. Roman, M. Berggren and O. Inganas, Appl. Phys. Lett. 75, 3557 (1999)

209 F.L.Zhang, A. Gadisa, O.Ingans, M.Svensson and H.R. Anderson, Appl. Phys. Lett. 84, 19 (2004)

210 Kirill Zilberberg, Houssem Gharbi, Andreas Behrendt, Sara Trost, and Thomas Riedl, ACS Appl. Mater. Interfaces, 4 (3), pp 1164–1168,, 2012

211 Steven K. Hau, Hin-Lap Yip, Nam Seob Baek, Jingyu Zou, Kevin O'Malley, and Alex K.-Y. Jen, Appl. Phys. Lett. **92**, 253301 (2008)

212 Chen Tao, Shengping Ruan, Guohua Xie, Xiangzi Kong, Liang Shen, Fanxu Meng, Caixia Liu, Xindong Zhang, Wei Dong, and Weiyou Chen, Appl. Phys. Lett. 94**,** 043311, (2009)

213 L. "Bert" Groenendaal, Friedrich Jonas, Dieter Frietag, Harald Pielartzik, John B. Reynolds, Adv. Mater. 12,7 (2000)

214 Tom J. Savenijea, Jessica E. Kroezeb, Xiaoniu Yangc, Joachim Loos, Thin solid films, 511-512, 2-6, (2006)

215 Jung Ah Lim, Feng Liu, Sunzida Ferdous, Murugappan Muthukumar, and Alejandro L. Briseno, Materials today, 13, 5, pp. 14, (2010)

216 Advanced characterization techniques for thin film solar cells, Ed. Danial Abou-Ras, Thomas Kirtchartz, and Uwe Rau, Wiley VCH, 2011

217 The metrology of electrical impedance at high frequency: A review., Callegaro, L. Meas. Sci. Technol., 20, 022002, (2009)

218 Li, G.P. and andWang, K.L., J. Appl. Phys., 57, 1016, (1985)

219 *Dielectric Relaxation in Solids*, Jonscher, A.K., Chelsea Dielectrics Press, Ltd, Chelsea. (1983)

220 Zabierowski, P. and Edoff, M., Thin Solid Films, 480–481, 301 (2005)

221 D. Vanmaekelbergh, J. van de Lagemaat, R.E.I. Schropp, Solar energy materials and solar cells, 41-42, 537-542, (1996)

222 Nese Kavasoglu, A. Sertap Kavasoglu, Ozcan Birgi, Sener Oktik, Solae energy materials and solar cells, 95, 2, (2011)

223 L. Dloczik, O. Ileperuma, I. Lauermann, L. M. Peter, E. A. Ponomarev, G. Redmond, N. J. Shaw, and I. Uhlendorf, J. Phys. Chem. B, 101, 10281-10289, (1997)

224 Chong Chen, Mingtai Wang, and Kongjia Wang, J. Phys. Chem. C, 113 (4), 1624-1631, (2009)

225 Laurence M. Peter, *Applications of kinetic modeling*, Ed. R. G. Compton, Gus Hancock, Comprehensive chemical kinetics, Vol. 37, Elsevier (1999)

226 A. V. Nenashev, S. D. Baranovskii, M. Wiemer, F. Jansson, R. Österbacka, A. V. Dvurechenskii, and F. Gebhard, Phys. Rev. B 84, 035210 (2011)

227 M. Wiemer, A. V. Nenashev, F. Jansson, and S. D. Baranovskii, Appl. Phys. Lett. 99, 013302 (2011).

228 S.J. Xu, W. Liu and M. F. Li, App. Phys. Lett. 81, 16, (2002)

229 M. Knupfer, Applied Physics A: Materials Science & Processing , 77, 5, 623 – 626, (2003)

230 Muth, J.F, J.H. Lee, I.K. Shmagin, R.M. Kolbas, H.C. Casey, Jr., B.P. Keller, U.K. Mishra, S.P. DenBaars, Appl. Phys. Lett. 71(18) , 2572-2574, (1997)

231 John E. Northrup, Phys. Rev. B, 76, 245202 (2007)

232 L.J.A. Koster, V.D. Mihailetchi, R.Ramaker, P.W.M. Blom, Appl. Phys. Lett. 86, 123509,(2005)

233 M.G. Harrison, J. Griiner, G.C.W. Spencer, Synthetic Metals, 76, 71-75 (1996).

234 *Semiconductor device fundamentals,* Robert F. Pierret, Pearson Education, Inc. (1996)

235 Nese Kavasoglu, A. Sertap Kavasoglu, Ozcan Birgi, Sener Oktik, Solar energy materials and solar cells, 95, 2 (2011)

236 Monojit Bag and K. S. Narayan, Phys. Rev. B, 82, (2010)

237 Joshua C. Byers, Scott Ballantyne, Konstantin Rodionov, Alex Mann, and O. A. Semenikhin, ACS Appl. Mater. Interfaces, 3 (2), pp 392–401, (2011)

238 P.M. DiCarmine, O.A. Semenikhin, Electrochimica Acta, 53, 11 (2008)

239 L. Dloczik, O. Ileperuma, I. Lauermann, L. M. Peter, E. A. Ponomarev, G. Redmond, N. J. Shaw, and I. Uhlendorf, J. Phys. Chem. B, 101 (49), pp 10281–10289, (1997)

240 Kai Zhu, Nathan R. Neale, Alexander Miedaner, and Arthur J. Frank, Nano Lett, 7 (1), pp 69–74, , (2007).

241 P. E. de Jongh and D. Vanmaekelbergh, J. Phys. Chem. B, 101 (14), pp 2716–2722, (1997)

242 Orestein, J. and Kastner, M., Phys. Rev. Lett. 46, 1421 (1981).

243 Agostinelli, T., Caironi, M.and Natali, D., Sampietro, M., Arca, M., Devillanova, F. and Ferrero, V., Synthetic Metals 157, 984 (2007).

244 K.S. Narayan , K.S. Gautam , B. Shivkumar , S. Ramakrishnan, Synthetic Metals 80, 239-242, (1996)

245 M. G. Harrison, J. Grùner and G. C. W. Spencer, Phys. Rev. B, 55, 12, (1997)

246 S.J. Xu, W. Liu and M. F. Li, Appl. Phys. Lett. 81, 16 2002

247 Sariciftci, N. S.; Smilowitz, L.; Heeger, A. J.; Wudl, F. Science, *258*, 1474, (1992)

248 Shaheen, S.; Brabec, C. J.; Sariciftci, N. S.; Padinger, F.; Fromherz, T.; Hummelen, J. C. Appl. Phys. Lett., *78*, 841, (2001).

249 K. C. Yee and R. R. Chance, J. Polym. Sci. Polym. Phys. Ed. 16, 431 (1978).

250 C. H. Lee, G. Yu, and A. J. Heeger, Phys. Rev. B 47, 15 543 (1993).

251 R. N. Marks et al., J. Phys. Condens. Matter 6, 1379 (1994)

252 K. C. Kao and W. Hwang, *Electrical Transport in Solids*, Pergamon, Oxford, pp. 386–465, (1979)

253 P. M. Borsenberger and D. S. Weiss, *Organic Receptors for Imaging Systems*, Dekker, New York, (1993).

254 R. N. Marks et al., J. Phys. Condens. Matter, 6, 1379, (1994)

255 G.W. Jones, D.M. Taylor, H.L. Gomes, Synth. Met. 101, 1-3, 431-432, (1999)

256 Takahiro Osasa, Shuhei Yamamoto and Michio Matsumura, Jpn. J. Appl. Phys. 45, pp. 3762 – 3765, (2006)

257 H.B. DeVore, Phys. Rev. 102, 1, 86, (1956)

258 Amal K. Ghosh, Don L. Morel, Tom Feng, Robert F. Shaw, and Charles A. Rowe, J. Appl. Phys. 45, 230 (1974)

259 C. W. Tang and A. C. Albrecht, J. Chem. Phys. 62, 2139 (1975)

260 Amal K. Ghosh and Tom Feng, J. Appl. Phys. 49, 5982 (1978)

261 K. S. Narayan and Th. B. Singh, Appl. Phys. Lett. 74, 3456 (1999)

262 Sung Heum Park, Anshuman Roy, Serge Beaupre, Shinuk Cho, Nelson Coates, Ji Sun Moon,Daniel Moses, Mario Leclerc, Kwanghee Lee and Alan J. Heeger, Nature Photonics, 3, 297, (2009)

263 Erin L. Ratcliff, Brian Zacher, and Neal R. Armstrong, J. Phys. Chem. Lett., 2011, 2 (11), pp 1337–1350

264 R. Schmechel and H. von Seggern, *Physics of organic semiconductors*, Ed. W. Brutting, Wiley VCH, 2005

265 *Semiconductor contacts, An approach to ideas and models*, Heinz K. Henisch, The international series of monographs of physics, Oxford Science publications, (1984)

266 A. Desormeaux, J. J. Max, and R. M. Leblanc, J. Phys. Chem.,97, 6670-6678, (1993)

267 Leif A. A. Pettersson, Lucimara S. Roman, and Olle Inganäs, J.App. Phys. 86, 1 1999

Errata

1) Page 52, equation (1.13),

The equation of conductivity should be read as,

$$\sigma = q(\mu_e n_e + \mu_h n_h) \tag{1.1}$$

2) Page 108, line 3,

LUMO should be replaced by HOMO.

3) Page 113, paragraph 2, line 8,

Value of *S* for 522 nm illuminations should be replaced by 0.034

4) Page 127, line 2,

The calculated trap density, for a device area of 0.06 cm^2, is of the order of $4.3X10^9$ eV^{-1} cm^{-2}

5) Page 139, figure 4.3,

The polymer layer, pBTTT should be replaced by P3HT.

6) Page 140, figure 4.4,

The polymer layer, pBTTT should be replaced by N2200.

7) Page 154, the following equations have been redefined,

In equations (5.2), divergence of drift current has been included in place of drift current itself. The modified equation is given as,

$$\frac{dn_{photo}(x)}{dt} = \varphi I_0 \alpha \exp(-\alpha x) - \frac{di_{diff}}{dx} - \frac{di_{drift}}{dx} - \frac{n_{photo}}{\tau} \tag{5.1}$$

In equation 5.2, n_{photo} is the electron or hole carrier density, $\alpha = \alpha(\epsilon)$, μ the bulk mobility of the photogenerated carrier, τ the bulk recombination lifetime, i_{diff} the diffusion current, and E is the applied field across the electrode. Under the equilibrium condition, the net charge flowing through *x* in the bulk is zero, giving $\frac{dn_{photo}(x)}{dt} = 0$. The diffusion current i_{diff}, then can be given

by $i_{diff} = -D_n \, {dn_{photo}}/{dx}$, where D_n is the carrier diffusion constant, i_{drift} is expressed as $i_{drift} = n\mu E$. Substituting $E = V/x$ with the expression for diffusion and drift current in equation 5.2, and assuming no spatial distribution of D_n and μ, equation (5.2) gives a time independent differential equation for steady state carrier density distribution in the bulk –

Equation (5.3) has been modified for divergence of drift current,

$$\frac{d^2 n_{photo}(x)}{dx^2} - \frac{dn_{photo}(x)}{dx}\left(\frac{\mu V}{xD_n}\right) = \frac{n_{photo}(x)}{D_n}\left(-\frac{\mu V}{x^2} + \frac{1}{\tau}\right) - \frac{\varphi I_0 \alpha}{D_n} exp(-\alpha x) \tag{5.2}$$

The solution of differential equation (5.3) is given in terms of Bessel functions of first and second type.

The Solution to differential equation (5.3) has been modified and given in equation (5.5)

$$\begin{aligned} n_{photo}(x) = x^{\left(\frac{1}{2}+\frac{\mu V}{2D}\right)} \Bigg\{ & BesselJ\left[\left(\frac{1}{2}-\frac{\mu V}{2D}\right), \frac{-ix}{L_D}\right] B + BesselY\left[\left(\frac{1}{2}-\frac{\mu V}{2D}\right), \frac{-ix}{L_D}\right] C \\ & + BesselJ\left[\left(\frac{1}{2}-\frac{\mu V}{2D}\right), \frac{-ix}{L_D}\right] \int_1^x \frac{\varphi I_{0\alpha}}{D}, exp(-\alpha x_1).\pi.x_1^{\left(\frac{1}{2}-\frac{\mu V}{2D}\right)} BesselY\left[\left(\frac{1}{2}-\frac{\mu V}{2D}\right), \frac{-ix}{L_D}\right] dx_1 \\ & - BesselY\left[\left(\frac{1}{2}-\frac{\mu V}{2D}\right), \frac{-ix}{L_D}\right] \int_1^x \frac{\varphi I_{0\alpha}}{D}, exp(-\alpha x_2).\pi.x_2^{\left(\frac{1}{2}-\frac{\mu V}{2D}\right)} BesselJ\left[\left(\frac{1}{2}-\frac{\mu V}{2D}\right), \frac{-ix}{L_D}\right] dx_2 \Bigg\} \end{aligned} \tag{5.5}$$

Using $\Gamma = \left(\frac{1}{2}+\frac{\mu V}{2D}\right)$, $\Delta = \left(\frac{1}{2}-\frac{\mu V}{2D}\right)$, and $A = \frac{\varphi I_{0\alpha}}{D}$, equation (5.5) can be written as,

$$\begin{aligned} & n_{photo}(x) \\ & = x^{\Gamma}\Bigg\{ BesselJ\left[\Delta, \frac{-ix}{L_D}\right] B + BesselY\left[\Delta, \frac{-ix}{L_D}\right] C \\ & + BesselJ\left[\Delta, \frac{-ix}{L_D}\right] \int_1^x Aexp(-\alpha x_1).\pi.x_1^{\Delta} BesselY\left[\Delta, \frac{-ix}{L_D}\right] dx_1 \\ & - BesselY\left[\Delta, \frac{-ix}{L_D}\right] \int_1^x Aexp(-\alpha x_2).\pi.x_2^{\Delta} BesselJ\left[\Delta, \frac{-ix}{L_D}\right] dx_2 \Bigg\} \end{aligned} \tag{5.6}$$

In equation 5.5, B and C are constants and L_D is the carrier diffusion length. For the case of exciton the solution of diffusion equation is given by,

$$n'(x) = B'exp\left\{-\frac{1}{L'_D}x\right\} + C'exp\left\{\frac{1}{L'_D}x\right\} + \frac{\theta I_0 \alpha exp(-\alpha x)}{D'\left(\frac{1}{L'^2_D} - \alpha^2\right)} \quad (5.7)$$

In equation 5.7, D' is the diffusion coefficient of exciton, this expression can also be used for free carriers when no external bias is applied, in that case *n*'(x) represents free carrier density. From the considerations of Devore model direct generation of free electron and holes in the bulk is assumed. The recombination of charge carriers can take place in the bulk after mean life time τ, or at any surface at a rate given by a recombination current $i_R = n_s S$. Where, $n_{S\ photo}$ is the density of electron hole pair and S is the surface recombination velocity. When film thickness is comparable to the reciprocal of the maximum value of absorption coefficient, a high surface recombination rate $S > D_n/L_{Dn}$ (bulk recombination rate) results in an antibatic response while a low recombination rate gives symbatic response. The boundary conditions for surface recombination at illuminated surface for zero external bias case can be given by,

$$(i_R)_0 = -D_n\left(dn_{photo}/dx\right)_{x=0} = -n_{0_{photo}}S \quad (5.8)$$

Boundary condition for surface far from the illuminated surface is given by,

$$(i_R)_L = -D_n\left(dn_{photo}/dx\right)_{x=L} = -n_{L_{photo}}S \quad (5.9)$$

The coefficient B'and C' mentioned in (5.10) and (5.11) are valid only for diffusion equation.

$$B' = \frac{\varphi I_0 \alpha/D_n}{\left(\beta^2 - \alpha^2\right)}\left\{\frac{(S - D_n\alpha)(D_n\beta - S)exp(-\alpha L) + (S + \alpha D_n)(S + \beta D_n)exp(\beta L)}{(D_n\beta - S)^2 exp(-\beta L) - (D_n\beta + S)^2 exp(\beta L)}\right\} \quad (5.10)$$

And

$$C' = \frac{\varphi I_0 \alpha/D_n}{\left(\beta^2 - \alpha^2\right)}\left\{\frac{(S - D_n\alpha)(D_n\beta + S)exp(-\alpha L) + (S + \alpha D_n)(D_n\beta - S)exp(-\beta L)}{(D_n\beta - S)^2 exp(-\beta L) - (D_n\beta + S)^2 exp(\beta L)}\right\} \quad (5.11)$$

In (5.10) and (5.11) $\beta = \frac{1}{L_D}$, is the inverse of carrier diffusion length.

Other grammatical corrections,

Preoskite should be replaced by perovskite.

Taps should be replaced by traps.

Pool should be replaced by Poole.

Roots should be replaced by routes.

Gown should be replaced by grown.

Sates should be replaced by states.

Columbic should be replaced by Coulombic.

Incorporation should be replaced by Inc.

Monochromtor should be replaced by monochromator.

Plain should be replaced by plane.

HUMO should be replaced by HOMO.

Devotions should be replaced by deviations.